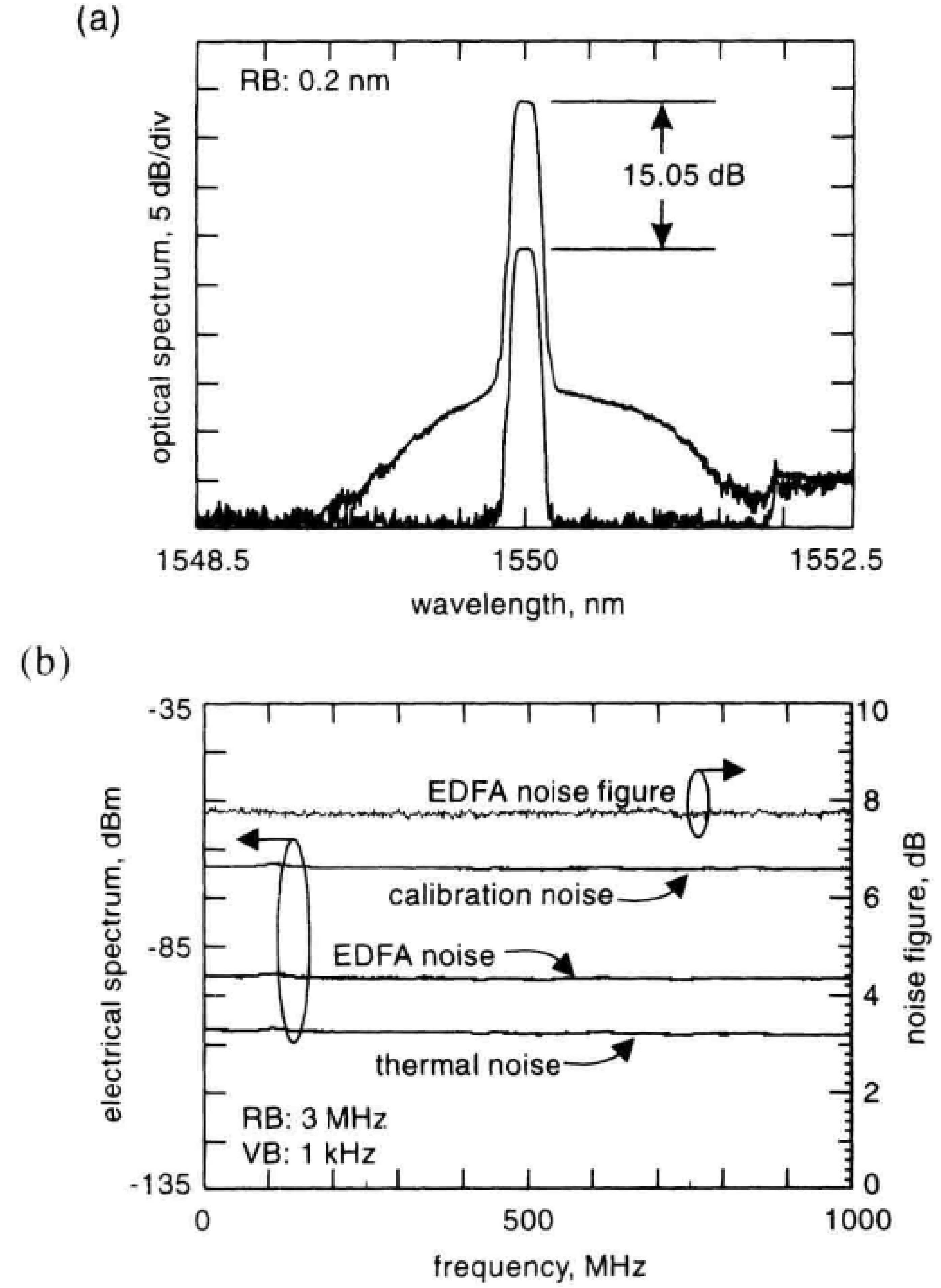

Figure 13.54 Noise figure measurement: (a) optical amplifier gain, (b) electrical spectrum analyzer display and noise figure result.

transition is activated by pumping into the $^1G_4$ band near 1 μm. The praseodymium-doped fluoride fiber amplifier (PDFFA) has demonstrated optical gains in excess of 40 dB, saturated output powers of 20.1 dBm and a sig-sp beat-noise-limited noise figure as low as 3.2 dB.[50–55] The PDFFA has a useful gain spectrum in excess of 30 nm as indicated in Figure 13.56. For communications applications, the problem of making a robust connection between the fluoride fiber and the silica fiber used for transmission has been solved, making commercialization of the PDFFA possible.[55] Alternate decay routes from the $^1G_4$ level reduces the fluorescent lifetime to ~ 110 μs. This is the reason the PFFDA operates most efficiently with stronger input signals. Weak signals must compete with the short fluorescent lifetime for the stored ion energy. For this reason, the PDFFA is usually used as a booster amplifier.

The trivalent neodymium ion $^4F_{3/2}-{}^4I_{13/2}$ transition provides gain about the 1.32 μm wavelength in fluorozirconate fiber. Pumping near the 0.8 μm wavelength provides a

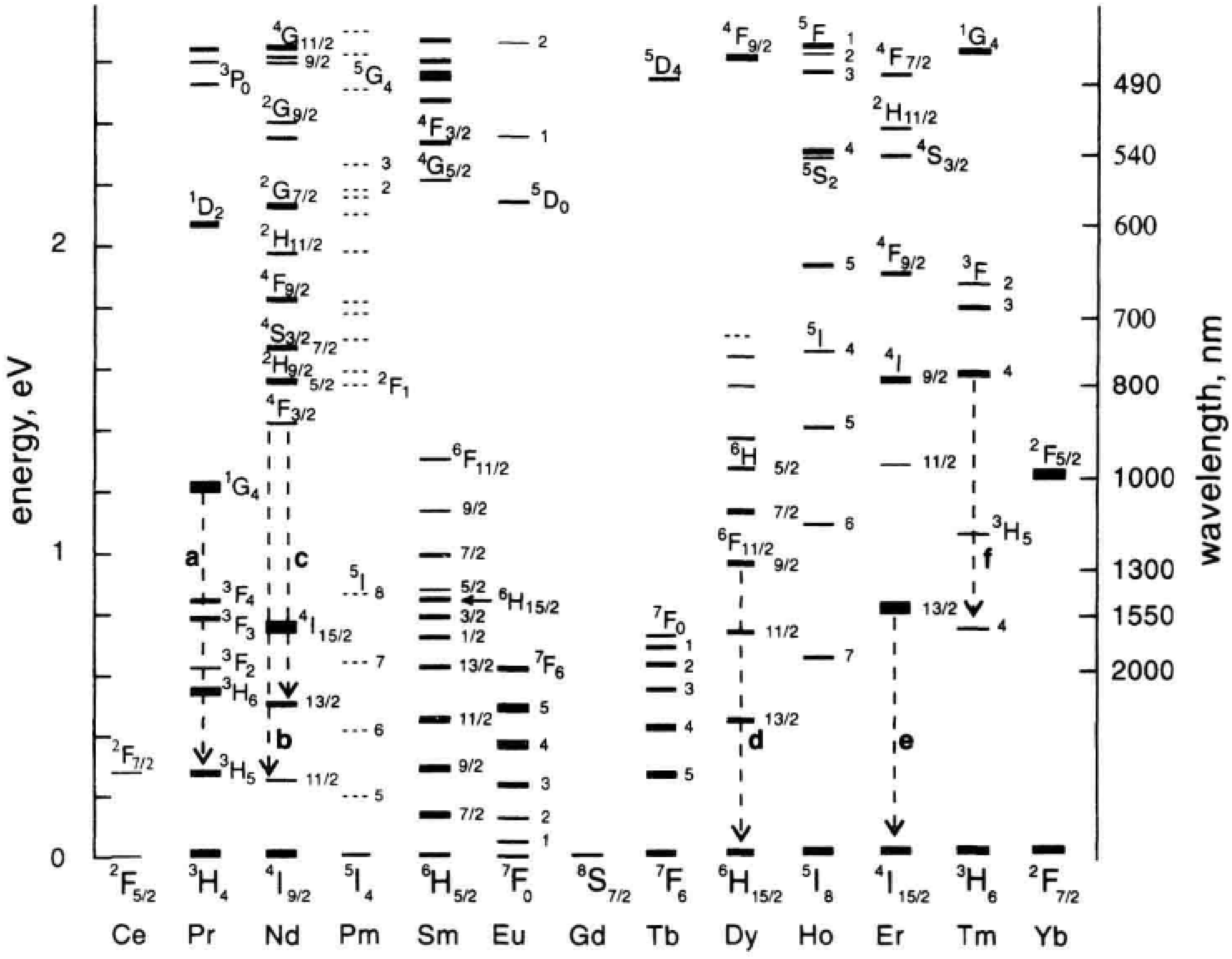

Figure 13.55 Partial energy level diagram for the trivalent rare earth ions. Some notable transitions: a: 1.31 μm, b: 1.06 μm, c: 1.34 μm, d: 1.32 μm, e: 1.53 μm, f: 1.47 μm. [after ref [15]].

ground-state $^4I_{9/2}$ to $^4F_{5/2}$ absorption which then populates the $^4F_{3/2}$-level. This transition is designated by 'c' in Figure 13.55. The efficiency of this amplifier is compromised by the strong 1.05 μm transition, designated by 'b' in the figure, which depopulates the metastable state population. Also upconversion of signal light to the $^4G_{7/2}$ level further competes with the desired transition.[56] Practical use of this transition will require suppression of the ASE generated by the large optical gain of the 1.05 μm transition.

Research is also being directed at the 1.32 μm ($^6H_{9/2}-{}^6F_{11/2}$) doublet to ground state $^6H_{15/2}$ transition of the dysprosium ion in low-phonon energy glasses.[57,58] This transition is designated by 'd' in Figure 13.55. This transition and the glass host is less mature than either the neodymium or praseodymium investigations in fluoride fiber, more work needs to be performed to fully evaluate its potential.

1.47 μm Amplifier. Gain near 1.47 μm from the trivalent thulium $^3F_4-{}^3H_4$ transition (designated by 'f' in Figure 13.55) has a number of applications ranging from transmission line monitoring to the possibility of opening up a new telecommunications band

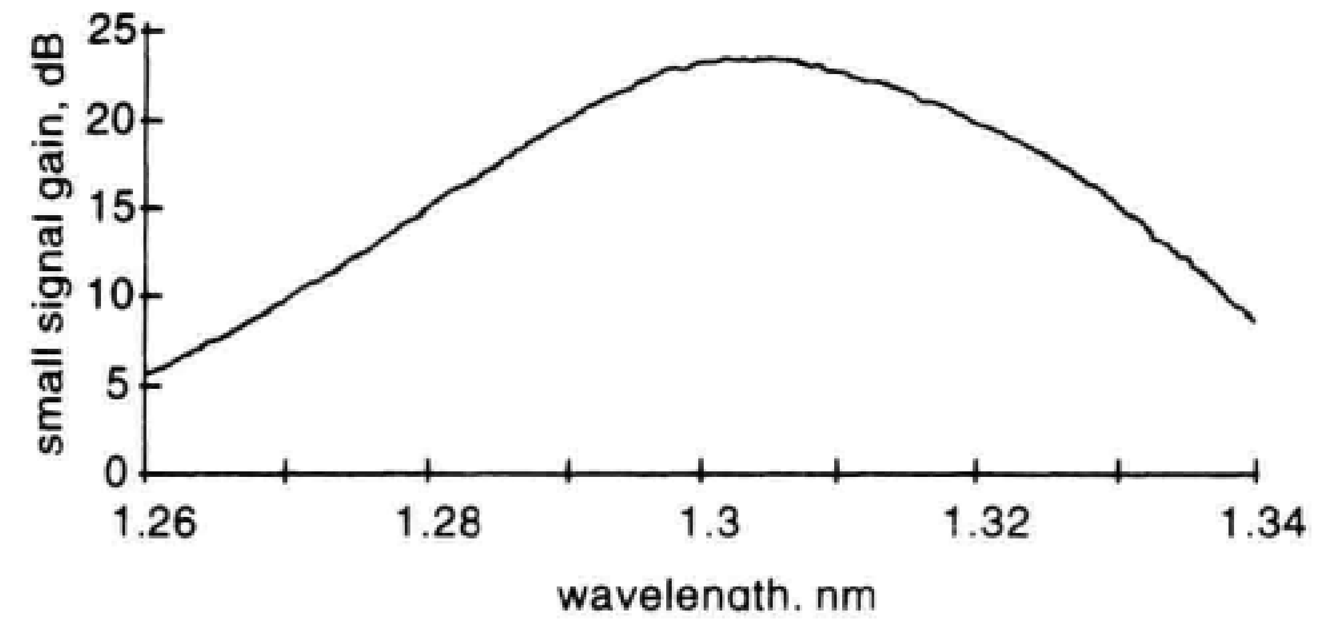

Figure 13.56 Small-signal gain spectrum for praseodymium-doped fluoride fiber amplifier. [with permission after ref [53] ©1993 BT Technol. J.].

in optical fiber. This transition can be pumped at a wavelength of 0.78 μm or 1.064 μm using an upconversion pumping scheme. The fluorozirconate glass host with its low-phonon energy has yielded the best performance. In one experiment, shown in Figure 13.57, an amplification bandwidth from 1440 nm to 1505 nm has been demonstrated with a maximum small-signal gain of 25 dB when 450 mW of pump power was applied.[59]

0.8 μm Amplifier. Thulium-doped fluoride fiber also provides transitions that can be used for 0.8 μm amplifiers. Low phonon energy fluoride fiber was used in an experiment that demonstrated 20 dB of gain with a saturated output power in excess of 10 dBm.[60] The optical gain was due to the $^3F_4$ to ground state $^3H_6$ transition shown in Figure 13.55. The $^3F_4$ energy level was populated by pumping at a wavelength of 790 nm. An amplification wavelength range from 795 nm to 820 nm appears to be feasible using this system.

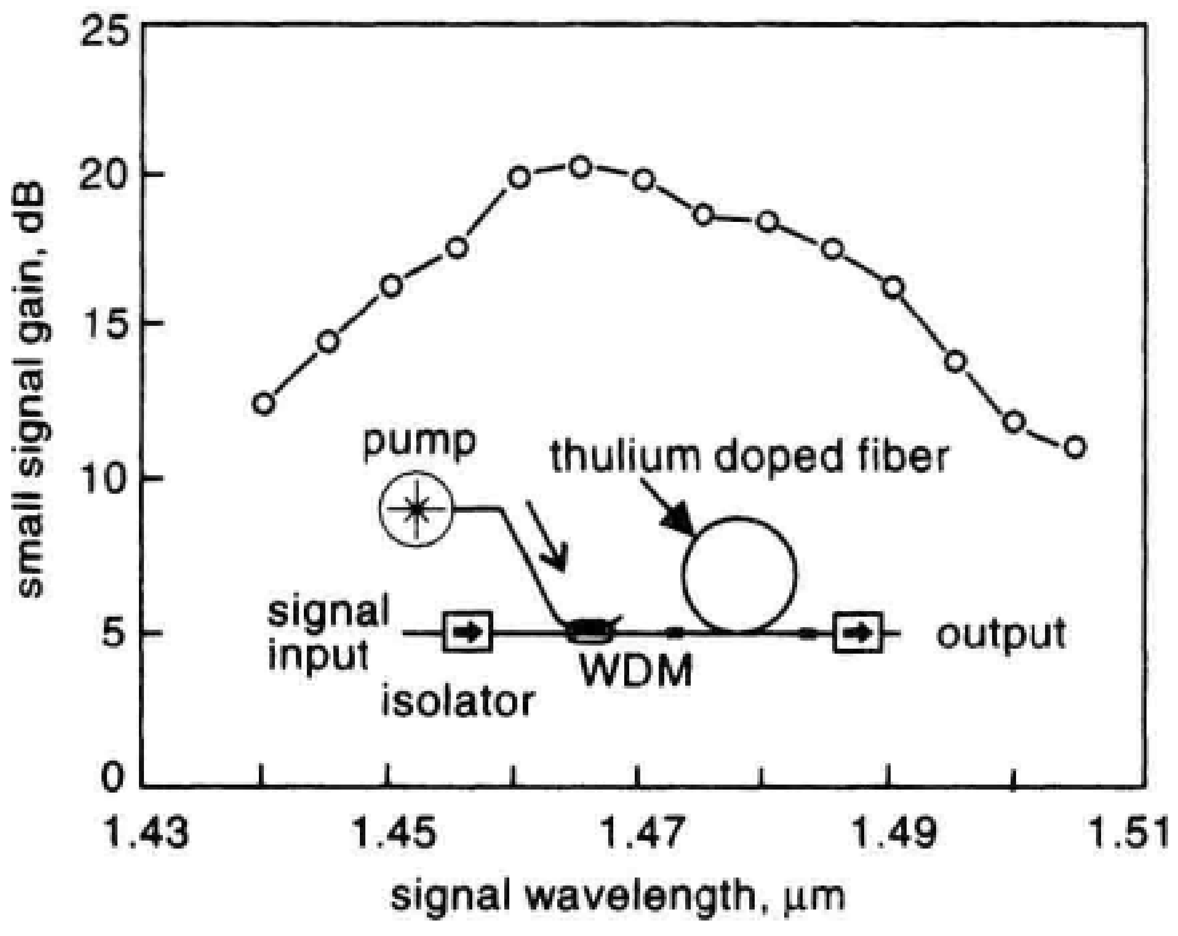

Figure 13.57 Small signal gain spectrum of thulium fluoride fiber amplifier as a function of wavelength [with permission after ref [59] ©1993 IEE].

13.6.2 Gain from Fiber Nonlinearities

Raman Amplifier. When pump-light intensity within an optical fiber becomes large, the glass molecules become excited into different vibrational states. In stimulated Raman scattering (SRS), the difference in energy between two vibrational states can be used to amplify an optical signal. This forms the basis for the Raman fiber amplifier (RFA). Unlike the rare-earth doped fiber amplifiers, the RFA doesn't require the addition of special dopants, the optical fiber in the transmission link acts as the gain medium. The RFA is made by coupling pump light into the transmission fiber. At a signal wavelength of 1.55 μm, pump powers and fiber lengths are of the order of 1 W and tens of kilometers respectively (see Appendix B). The pump laser and signal frequency separation is equal to the Raman shift frequency which depends on the characteristics of the glass fiber. This shift is approximately −12 THz, or +100 nm at a wavelength of 1.55 μm in telecommunications fiber. Therefore to obtain gain in the 1.55 μm wavelength band, the wavelength of the pump laser is set to ~ 1.45 μm. An example of an RFA gain spectrum is shown in Figure 13.58.[61] The useable gain bandwidth is approximately 50 nm (6 THz).

Some simple approximate relations are useful for providing insight into the RFA.[62,63] Assuming that the stimulated Brillouin scattering and/or pump depletion is small, the amplifier gain for a fiber of length L is given by:

$$G \approx e^{\frac{g_r P_o L_{\text{eff}}}{A_{\text{eff}}} - \alpha_s L} \tag{13.69}$$

where P_o is the input pump power (watts) and L_{eff} is the effective length (meters). The Raman efficiency coefficient C_r is defined by $C_r = g_r/KA_{\text{eff}}$ where g_r is the peak Raman gain, $K = 2$ corresponds to nonpolarization maintaining optical fiber and A_{eff} is the effective core area.[62–64] The Raman gain coefficient, C_r, depends on wavelength and the type of optical fiber. Increasing the germanium concentration tends to increase C_r. Measure-

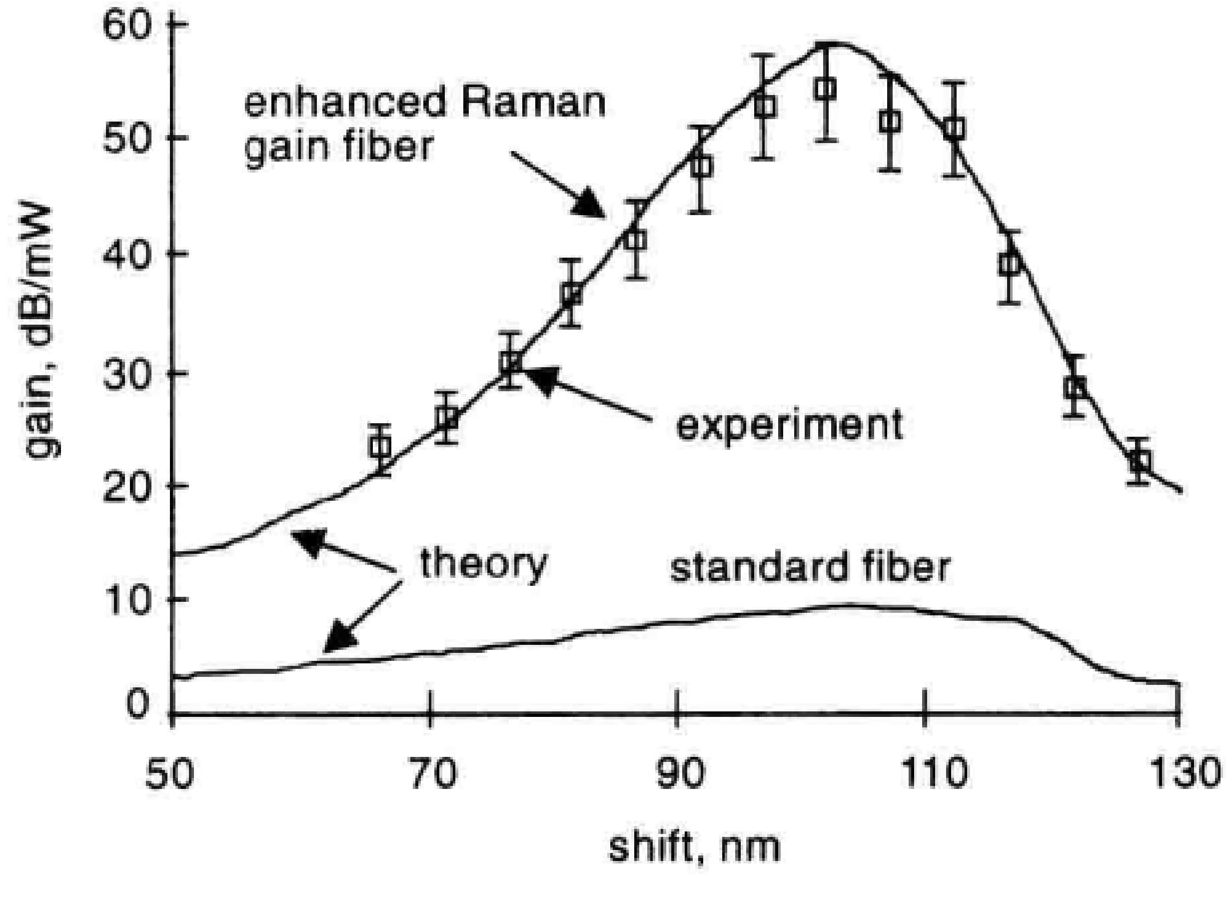

Figure 13.58 Raman gain spectrum for highly doped fiber and standard fiber. Pump wavelength is 1485 nm [with permission after ref [61] ©1990 IEE].

ments of the Raman gain coefficient on different optical fibers in the wavelength range of 1540 nm to 1565 nm yielded a range of values of C_r from 1.8×10^{-4} to 6×10^{-4} W^{-1} m^{-1}.[64] The effective length is reduced compared to the physical length due to fiber losses. L_{eff} is related to the fiber loss at the pump wavelength, α_p (m^{-1}) as:[62]

$$L_{\text{eff}} = \frac{1}{\alpha_p}[1 - e^{-\alpha_p L}] \tag{13.70}$$

Example

Equations 13.69 and 13.70 are illustrated by way of example. The gain and effective length dependence on fiber length are calculated under the following conditions: $C_r = 5 \times 10^{-4}$ W^{-1} m^{-1} (nonpolarization maintaining fiber), pump power is 500 mW, and the losses at the pump and signal wavelengths are assumed to be 0.25 dB/km. The exponential loss factor is first calculated using $\alpha = 0.001 \times \ln(10^{0.25/10})$ m^{-1}. The effective length is next calculated using Equation 13.70 which is used in Equation 13.69. The results are plotted as a function of fiber length in Figure 13.59. Figure 13.59a shows the gain/loss for the case of no pumping and also with 500 mW of pump power applied. Figure 13.59b shows the effective length, as

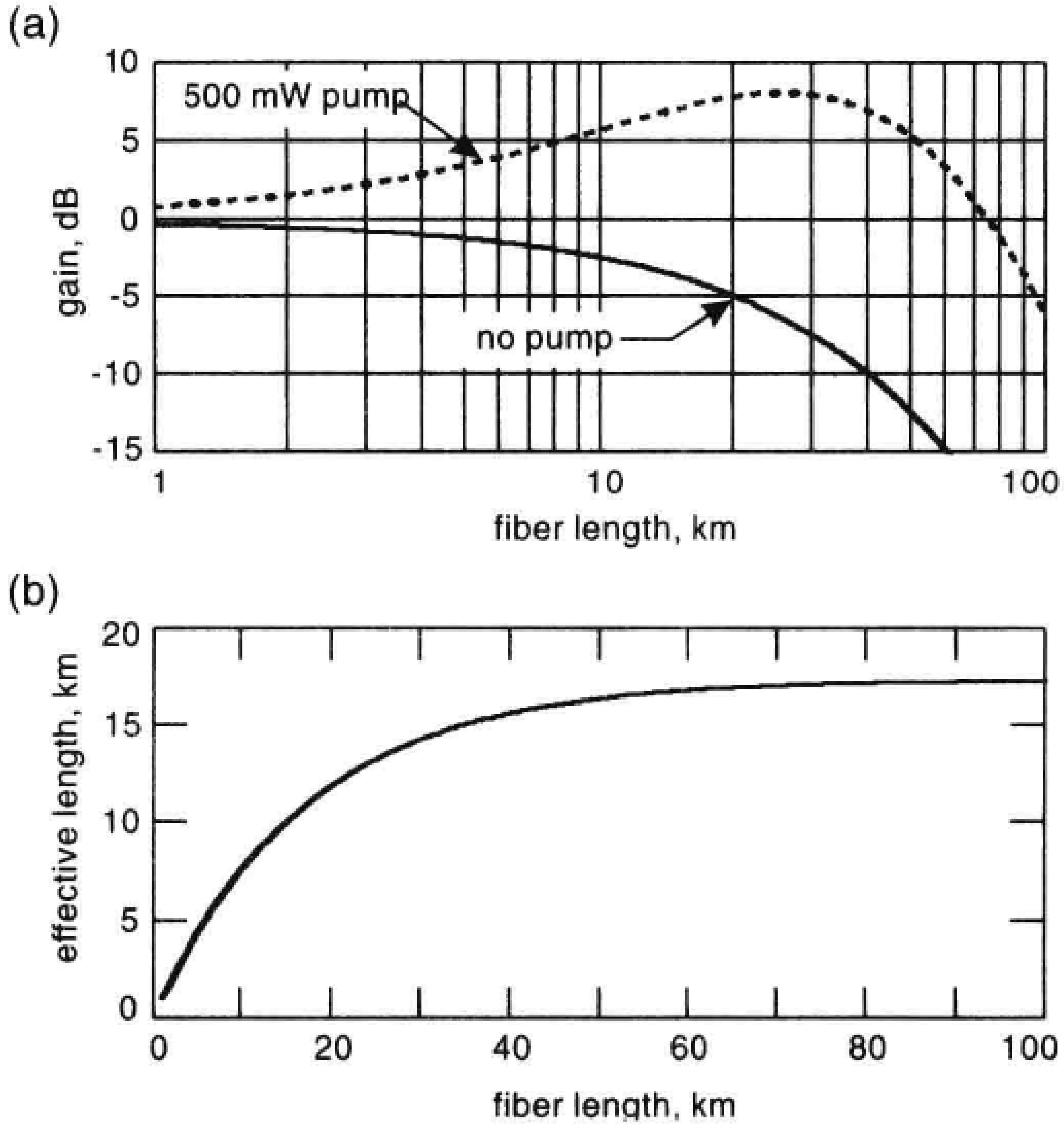

Figure 13.59 (a) Raman gain dependence on fiber length. (b) Effective fiber length as a function of actual length.

limited by propagation loss, as a function of actual fiber length. For a given pump power there is an optimum fiber length. Beyond the optimum length, the RFA gain decreases.

Stimulated Brillouin Scattering: Brillouin Amplifier. The Brillouin amplifier is based on the acoustic waves (phonons) created when high-intensity light passes through an optical fiber. The optical field causes electrostriction in the fiber which then creates acoustic waves. These acoustic waves scatter light in the backward direction creating optical gain for signals, at the proper frequency, traveling in the opposite direction as the original high intensity light. The gain spectrum is shifted approximately 11 GHz from the pump frequency in silica fiber at 1.55 μm. This is compared to a shift of approximately 6 THz for the Raman effect. The exact shift depends on factors such as the fiber geometry and the residual stress in the glass. The SBS gain spectrum is also quite narrow, on the order of 10 ~ 20 MHz as indicated by the SBS ASE spectrum shown in Figure 13.60. Stimulated Brillouin scattering (SBS) is detrimental in optical links employing narrow linewidth lasers. Even at low power levels, on the order of 1 mW, SBS can create significant backscatter of the forward propagating signal. As a result of the narrow gain bandwidth of the SBS amplifier, it hasn't yet attracted much attention for amplification of telecommunications signals. SBS has received significant attention due to the unwanted optical backscatter it creates.

13.6.3 Semiconductor Amplifiers

The semiconductor optical amplifier (SOA) provides a wavelength flexible solution to optical amplification. It offers efficient economical amplification at every telecommunications wavelength and is a contender for 1.3 and 1.55 μm amplification. There are a number of technical obstacles that have limited their deployment in communications applications. This includes: gain-saturation-induced-crosstalk, gain-ripple, polarization-dependent gain, and poor mode-match to optical fiber resulting in excess optical loss and an increase in noise figure. Device structure improvements to improve the SOA along with the utilization of gain clamping techniques to reduce crosstalk are improving their applicability to communications systems.[65,66,67]

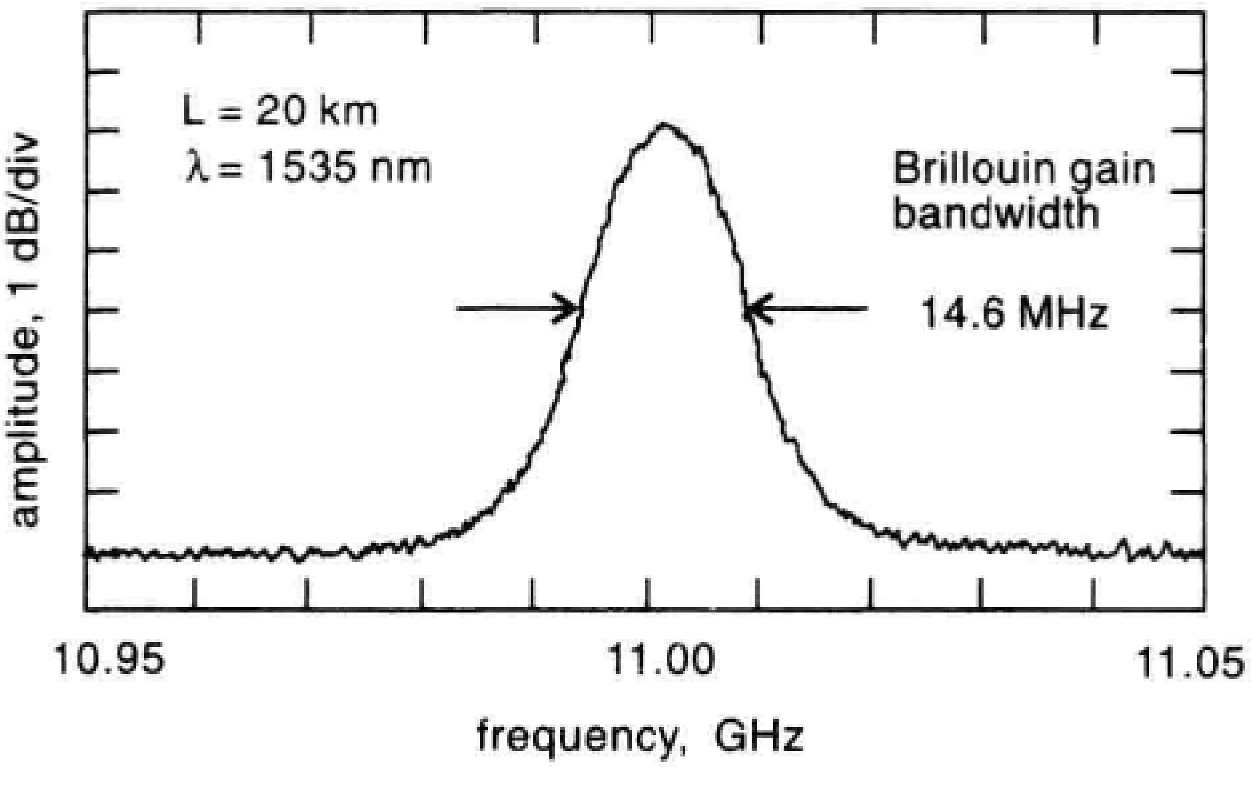

Figure 13.60 Brillouin gain spectrum for 1.3 μm zero dispersion optical fiber.

13.6.4 Measurement of Other Types of Optical Amplifiers

In this chapter, optical and electrical methods for noise figure and gain measurement were discussed with an emphasis on their application to the EDFA. Many of these techniques can be applied to the various non EDFA amplifiers discussed. A brief discussion is given here concerning the applicability of the measurement methods to other types of optical amplifiers.

With the optical method, the optical source subtraction technique can be applied, in principle, to any of the amplifiers discussed above. The polarization nulling and time domain extinction methods require certain assumptions on the amplifier polarization dependence and gain recovery time constants which must be considered. The polarization-nulling method works best for amplifiers with polarization-independent gain and low polarization mode dispersion. The TDE method requires instrumentation capable of gating optical signals rapidly compared to the recovery time of the optical amplifier under test. This may prove very challenging in amplifiers with short gain recovery times (< 1 ns) such as the Raman fiber amplifier (RFA).

The electrical noise figure methods, while more complicated, are quite versatile if performed properly. They can be applied to all optical amplifiers. It is beyond the scope of this text to provide an analysis of each technique for each type of optical amplifier. However, as a suggestive guide, Table 13.7 indicates which technique(s) may be most applicable for the most commonly used amplifiers.

13.7 SOURCES OF MEASUREMENT ERRORS

The characterization of optical amplifiers can involve a variety of instrumentation with many possible configurations and measurement procedures. This tends to make the analysis of measurement error specific to the particular experimental arrangement at hand. There are, however, common sources of measurement error that contribute to the measurement uncertainty.[68] The major sources of measurement uncertainty with some typical values are listed here:

- Connector uncertainty: ± .25 dB;
- OSA effective optical noise bandwidth: ± 0.1 dB;

Table 13.7 Guide to Measurement Methods

Amplifier	Source subtraction	Time-domain extinction	Polarization extinction	Electrical method
EDFA	yes	yes	yes	yes
PDFA	yes	yes (need rapid gate)	yes	yes
Raman	yes	no	depends on PMD	yes
Semiconductor	yes	no (unless gain-clamped)	yes	yes

- OSA scale fidelity: ± 0.05 dB;
- OSA polarization dependence: ± 0.1 dB;
- Power meter amplitude accuracy: ± 0.1 dB; and
- Amplitude instability due to interferometric effects.

From this list, it is clear that eliminating optical connectors at the amplifier and using fusion splices instead will significantly improve the measurement uncertainty. Most of the other uncertainties are addressed by the instrument specifications. The use of polarization randomizers and measurement averaging can reduce the uncertainty due to polarization dependencies in the test equipment.

13.8 USEFUL CONSTANTS FOR EDFA MEASUREMENTS

Table 13.8 includes a list of physical constants that may be useful for optical amplifier noise and gain calculations.

13.9 SUMMARY

In this chapter a variety of measurement techniques were discussed related to amplifier gain and noise figure characterization. The various measurement techniques covered represent a subset, though significant, of the diverse set of methods available for characterization of optical amplifiers.

Some discussion was given to the inner workings of the EDFA to familiarize the reader who is new to this kind of optical amplifier. The discussions on gain and noise in Sections 13.3 and 13.4 provide background information helpful for the discussion on noise figure and measurement techniques. In Section 13.5, the measurement methods for noise figure and gain were grouped into two broad categories: OSA-based, and electrical spectrum analyzer-based. The optical methods included the source subtraction method, the polarization-extinction technique, and the TDE technique. The TDE was extended with the addition of a broadband EELED to permit measurement of the amplifier dynamic gain.

Table 13.8 Useful Physical Constants

Description	Symbol	Value	Units
Electron charge	q	1.602×10^{-19}	coul.
Velocity of light	c	2.99793×10^{8}	ms^{-1}
Planck's constant	h	6.625×10^{-34}	$J\text{-}s^{-1}$
Boltzmann constant	k	1.3806×10^{-23}	$J\text{-}K^{-1}$
1 electron volt	1 eV	1.602×10^{-19}	J

WDM characterization EDFAs was discussed in terms of relevancy of the single-channel techniques previously discussed. An approach was presented to measure the WDM-gain spectrum that uses a reduced set of saturating sources. This technique reduces test costs when large numbers of WDM channels are required.

The electrical technique for noise figure measurement was discussed. This method provides the most complete characterization of the noise performance of an optical amplifier. The electrical method tends to be less tolerant to errors in the measurement technique.

A brief survey of other types of optical amplifiers was given in Section 13.6. This provides a quick appreciation of other existing amplifier technologies. A discussion was also given concerning the relevancy of the measurement methods to these amplifier types. The dominant causes of measurement uncertainty in terms of instrument limitations was outlined in Section 13.7. Finally, the most often used physical constants for noise figure calculations is tabulated in Section 13.8 to save the reader the time required to search this information in texts on physics.

REFERENCES

1. Nilsson, J., Lee, Y.W., Kim, S.J., Lee, S.H., and Choe, W.H., 1996. Analysis of AC gain tilt in erbium-doped fiber amplifiers. *IEEE Photon. Technol. Lett.* 8 (4):515–517.
2. Desurvire, E., Giles, C.R., and Simpson, J.R. 1989. Gain saturation effects in high-speed, multichannel erbium-doped fiber amplifiers at λ=1.53 μm. *J. Lightwave Technol.* 7 (12):2095–2104.
3. Freeman, J. and Conradi, J. 1993. Gain modulation response of erbium-doped fiber amplifiers. *IEEE Photon. Technol. Lett.* 5(2): 224–226.
4. Giles, C.R. and Desurvire, E. 1989. Transient gain and crosstalk in erbium-doped fiber amplifiers. *Optics Lett.* 14:880–882.
5. Taylor, M.G. 1993. Observation of new polarization dependence effect in long haul optically amplified system. *IEEE Photon. Technol. Lett.* 5 (10):1244–1246.
6. Gimlett, J.L., Iqbal, M.Z., Curtis, L., Cheung, N.K., Righetti, A., Fontana, F., Grasso, G. 1989. Impact of multiple reflection noise in Gbit/s lightwave systems with optical fiber amplifiers. *Electron. Lett.* 25 (20):1393–1394.
7. Kobayashi, M., Ishihara, T., and Gotoh, M. 1993. Power penalty due to optical reflections in erbium-doped fiber preamplifier. *IEEE Photon. Technol. Lett.* 5 (8):925–928.
8. Snitzer, E. 1961. Optical maser action of Nd3+ in a barium crown glass. *Phys Rev. Lett.* 7: 444–449.
9. Koester, C.J., Snitzer, E.A. 1964. Amplification in a fiber laser. *Applied Optics* 3 (10):1182.
10. Mears, R.J. et al. 1986. Low threshold, tunable cw and Q-switched fibre laser operating at 1.55 μm. *Electron. Lett.* 22 (3):159.
11. Mears, R. J., Reekie, L. Jauncey, I.M., and Payne, D.N. 1987. High gain rare-earth doped fiber amplifier at 1.54 μm. in *Conference on Optical Fiber Communication/International Conference on Integrated Optics and Optical Fiber Communication Technical Digest Series 1987, Vol. 3,* (Optical Society of America, Washington, DC 1987):167.
12. Delavaux, J-M, P., and Nagel, J.A. 1995. Multi-stage erbium-doped fiber amplifier designs. *J. Lightwave Technol.* 13 (5):703–720.

13. Hill, K.O., Malo, B., Bilodeau, F., Johnson, D.C., and Albert, J. 1993. Bragg gratings fabricated in monomode photosensitive optical fiber by UV exposure through a phase mask. *Appl. Phys. Lett.* 62 (10):1035–1037.
14. Ainslie, B.J. 1991. A review of the fabrication and properties of erbium-doped fibers for optical amplifiers. *J. Lightwave Technol.* 9 (2):220-227.
15. Dieke, G.H., and Crosswhite, H.M. 1963. The spectra of the doubly and triply ionized rare-earths. *Applied Optics,* 2 (7):675–686.
16. Optical fibre lasers and amplifiers, 1996. Edited by P.W. France. Blackie & CRC Press Inc.
17. Desurvire, E. Erbium Doped Fiber Amplifiers, Principles and Applications, John Wiley & Sons, Inc. 1994.
18. Ainslie, B.J., Craig, S.P., and Davey, S.T. 1988. The absorption and fluorescence spectra of rare-earth ions in silica-based monomode fiber. *J. Lightwave Technol.* 6 (2):287–293.
19. Miniscalco, W.J. 1991. Erbium-doped glasses for fiber amplifiers at 1500 nm. *J. Lightwave Technol.* 9 (2):234–250.
20. Horiguichi, M., Shimizu, M., Yamada, M., Yoshino, K., Hanafusa, H. 1990. Highly efficient optical fibre amplifier pumped by a 0.8 μm band laser diode. *Electron. Lett.* 26 (21):1758–1759.
21. Horiguichi, M., Yoshino, M., Shimizu, M., and Yamada, M. 1993. 670 nm semiconductor laser diode pumped erbium-doped fiber amplifers. *Electron. Lett.* 29 (7):593–595.
22. Giles, C.R. and Desurvire, E. 1991. Modeling erbium-doped fiber amplifers. *J. Lightwave Technol.* 9 (2):271–283.
23. Clesca, B., Bayart, D., and Beylat, J.L. 1995. 1.5 μm fluoride-based fiber amplifiers for wide-band multichannel transport networks. *Optical Fiber Techn.* 1:135–157.
24. Ono, H., Nakagawa, K., Yamada, M., and Sudo, S. 1996. Er3+-doped fluorophosphate glass fibre amplifier for WDM systems. *Electron. Lett.* 32 (17):1586–1587.
25. Mori, A., Ohishi, Y., Yamada, M., Ono, H., Nishida, Y., Oikawa, K., and Sudo, S. 1997. *1.5* μm broadband amplification by tellurite-based EDFAs. In *Optical Fiber Communication Conference,* Vol. 6, 1997 OSA Technical Digest Series vol. 6 (Optical Society of America, Washington, D.C.), PD1.
26. Agrawal, G.P. 1995. *Non linear fiber optics.* 2nd ed. San Diego, CA: Academic Press.
27. Mazurczyk, V.J., and Zyskind, J.L. 1994. Polarization dependent gain in erbium doped-fiber amplifiers. *IEEE Photon. Technol. Lett.* 6 (5):616–618.
28. Taylor, M.G. and Penticost, S.J., 1994. Improvement in performance of long haul EDFA link using high frequency polarization scrambling modulation. *Electron. Lett.* 30 (10): 805–806.
29. Bergano, N.S., Davidson, C.R., and Heismann, F. 1996. Bit-synchronous polarization and phase modulation scheme for improving the performance of optical amplifier transmission systems. *Electron. Lett.* 32 (1):52–54.
30. Desurvire, E., Zyskind, J.L., and Simpson, J.R. 1990. Spectral gain hole-burning at 1.53 μm in erbium-doped fiber amplifiers. *IEEE Photon. Technol. Lett.* 2 (4):246–248.
31. Walker, G.R. 1991. Gain and noise characterisation of erbium-doped fiber amplifiers. *Electron. Lett.* 27 (9):744–745.
32. Srivastava, A.K., Zyskind, J.L., Sulhoff, J.W., Evankow, J.D. Jr., and Mills, M.A. 1996. Room temperature spectral hole-burning in erbium-doped fiber amplifiers. In *OFC'96 Technical Di-*

gest, Optical Fiber Communication Conference, Technical Digest Series Vol. 2 (Optical Society of America, Washington, DC, 1996):33–34.

33. Hansen, S.L., Andreasen, S.B., Thorsen, P., and Dybdal, K. 1993. Experimental verification of new EDFA gain-tilt distortion theory. *IEEE Photon. Technol. Lett.* 5 (12):1433–1435.
34. Olsson, N.A. 1989. Lightwave systems with optical amplifers. *J. Lightwave Technol.* 7 (7):1071–1082.
35. Baney, D.M. and Sorin, W.V. 1995. Broadband frequency characterization of optical receivers using intensity noise. *Hewlett-Packard J.* 46(1):6–12.
36. Bonnedal, D. 1993. Single-setup characterization of optical fiber amplifiers. *IEEE Photon. Technol. Lett.* 5 (10):1193–1195.
37. Chou, H. and Stimple, J. 1995. Inhomogeneous gain saturation of erbium-doped fiber amplifiers. In *Optical Amplifiers and their Applications,* Technical Digest Series Vol. 8 (Optical Society of America, Washington, DC, 1995):92–95.
38. Poole, S. 1994. Noise figure measurement in optical fibre amplifiers. In *NIST Technical Digest—Symposium on optical fiber measurements,* Boulder, CO. NIST special publication 864: 1–6.
39. Baney, D.M., and Dupre, J. 1992. Pulsed-source technique for optical amplifier noise figure measurement. *European Conference on Communications.* Paper WeP2.11. Berlin.
40. Bertilsson, K., Andrekson, P.A., and Olsson, B.E. 1994. Noise figure of erbium-doped fiber amplifiers in the saturated regime. *IEEE Photon. Technol. Lett.* 6(10):199–201.
41. Onaka, H., Miyata, H., Ishikawa, G., Otsuka, K., Ooi, H., Kai, Y., Kinoshita, S., Seino, M., Nishimoto, H., and Chikama, T. 1996. 1.1 Tb/s WDM transmission over a 150 km 1.3 μm zero-dispersion singlemode fiber. In *Optical Fiber Communication Conference,* Technical Digest Series Vol. 2 (Washington, DC: *Optical Society of America,* 1996) PD 19.
42. Baney, D.M. and Stimple, J. 1996. WDM EDFA gain characterization with a reduced set of saturating channels. *IEEE Photon. Technol. Lett.* 8(12):1615–1617.
43. Baney, D.M. and Jungerman, R.L. 1997. Optical Noise Standard for the Electrical Method of Optical Amplifier Noise Figure Measurement" in *Optical Amplifiers and Their Applications, Technical Digest Series* Vol. 2 (*Optical Society of America:* Washington, DC) paper MB3.
44. Willems, F.W., van der Plaats, Hentschel, D., and Leckel, E. 1994. Optical amplifier noise figure determination by signal RIN subtraction. In *NIST Technical Digest—Symposium on optical fiber measurements,* Boulder, CO: NIST Special publication 864:7–9.
45. Smart, R.G., Hanna, D.C., Tropper, A.C., Davey, S.T., Carter, S.F., and Szebesta, D. 1991. CW room temperature upconversion lasing at blue, green and red wavelengths in infrared-pumped Pr^{3+}-doped fluoride fibre. *Electron. Lett.* 27:1307–1309.
46. Piehler, D., Craven, D., Kwong, N.K., and Zarem, H. 1993. Laser-diode-pumped red and green upconversion fibre lasers. *Electron. Lett.* 29:1857–1858.
47. Baney, D.M., Rankin, G., and Chang, K.W. 1996. Simultaneous blue and green upconversion lasing in a laser-diode-pumped Pr^{3+}/Yb3+doped fluoride fiber laser. *Appl. Phys. Lett.* 69(12):1662–1664.
48. Baney, D.M., Rankin, G., and Chang, K.W. 1996. Blue Pr^{3+}–doped ZBLAN fiber upconversion laser. *Optics Lett.* 21(17):1372–1374.
49. Petreski, B.P., Murphy, M.M., Collins, S.F., and Booth, D.J. 1993. Amplification in Pr^{3+}–doped fluorozirconate optical fibre at 632.8 μm. *Electron. Lett.* 29:1421–1423.
50. Durteste, Y., Monerie, M., Allain, J.Y., Poignant, H. 1991. Amplification and lasing at 1.3 μm in praseodymium-doped fluorozirconate fibres. *Electron. Lett.* 27(8):626–628.

51. Miyajima, Y., Sugawa, T., and Fukasaku, Y. 1991. 38.2 dB amplification at 1.31 μm and possibility of 0.98 μm pumping in Pr^{3+}–doped fluoride fibre. *Electron. Lett.* 27(19):626–628.
52. Miyajima, Y., Sugawa, T., Fukasaku, Y. 1992. Noise characteristics of Pr^{3+}–doped fluoride fibre amplifier. *Electron. Lett.* 28(3):246–247.
53. Whitley, T.J., Wyatt, R., Szebesta, D., and Davey, S.T. 1993.Towards a practical 1.3 μm optical fibre amplifier. *BT Technol. J.* 11(2):115–127.
54. Yamada, M. et al. 1995. Low-noise and high-power PR^{3+}–doped fluoride fiber amplifier. *IEEE Photon. Technol. Lett.* 7(8):868–871.
55. Dye, S., Fake, M., and Simmons, T.J. 1994. Practical praseodymium power amplifier with a saturated output power of +18 dBm, in Conference on *Optical Fiber Communications, Technical Digest Series,* Vol. 4 (Optical Society of America, Washington DC, 1994):200.
56. Payne, A.S., Wilke, G.D., Smith, L.K., and Krupke, F. 1994. Auger upconversion losses in Nd-doped laser glasses. *Optics. Comm.* 111:263–268.
57. Page, R., Schaffers, K.I., Wilke, G.D., Waide, P., A., Tassano, J.B., Beach, R.J., Payne, S.A., and Krupke, W.F. 1996. Observation of 1300 nm gain in dysprosium-doped chloride crystals in *Optical Fiber Communication Conference, Technical Digest Series,* Vol. 2 (Optical Society of America, Washington DC, 1996).
58. Samson, B.N., Medeiros, J.A., Neto, R.I., Laming, R.I., and Hewak, D.W. 1994. Dyprosium doped Ga:La:S glass for a efficient optical fibre amplifier operating at 1.3 μm. *Electron. Lett.* 30(19):1617–1619.
59. Komukai, T., Yamamoto, T., Sugawa, T., and Miyajima, Y. 1993. 1.47 μm band Tm^{3+} doped fluoride fibre amplifier using a 1.064 μm upconversion pumping scheme. *Electron. Lett.* 29(1):110–112.
60. Dye, S.P., Fake, M., and Simmons, T.J. 1995. Fully engineered 800 nm thulium-doped fluoride-fiber amplifier. In *Optical Fiber Communications, Technical Digest Series,* Vol. 8 (Optical Society of America, Washington DC, 1995):110.
61. Spirit, D.M., Blank, L.C., Davey, S.T., and Williams, D.L. 1990. System apects of Raman fibre amplifiers. *IEE Proc.* 137, Pt. J. (4):221–224.
62. Stolen, R.H. and Ippen, E.P. 1973. Raman gain in glass optical waveguides. *Appl. Phys. Lett.* 22(6):276–278.
63. Aoki, Y. 1988. Properties of fiber Raman amplifiers and their applicability to digital optical communications systems. *J. Lightwave Technol.* 6(7):1225–1239.
64. da Silva, V.L. 1994. Comparison of Raman efficiencies in optical fibers. In *Conference on Optical Fiber Communications, Technical Digest Series,* Vol. 4 (Optical Society of America, Washington, DC, 1994):136–137.
65. Tiemeijer, L.F., Thijs, P.J.A., and Binsma, J.J.M. 1994. Progress in 1.3 μm polarization insensitive multiple quantum well laser amplifiers. In *Optical Fiber Communications, Technical Digest Series,* Vol. 17 (Optical Society of America, Washington, DC, 1994):234–236.
66. Doussiere, P. 1996. Recent advances in conventional and gain clamped semiconductor optical amplifiers. In *Optical Fiber Communications, Technical Digest Series,* Vol. 19 (Optical Society of America, Washington DC, 1994):220–223.
67. Koren, U., Miller, B.I., Young, M.G., Chien, M., Raybon, G., Brenner, T., Ben-Michael, R., Dreyer, K., and Capik, R.J. 1996. Polarization insensitive semiconductor optical amplifier with integrated electroabsorption modulators. *Electron. Lett.* 32(2):111–112.
68. Leckel, E., Sang, J., Muller, R., Ruck, C., and Hentschel, C. 1995. Erbium-doped fiber amplifier test system. *Hewlett-Packard J.* 46(1):13–19.

APPENDIX

A

Noise Sources in Optical Measurements

Wayne V. Sorin

This appendix discusses some of the dominant noise sources that limit the sensitivity in both coherent and direct-detection optical receiver configurations. Each noise source will be dealt with independently with the understanding that the total noise is found by summing the squares of the individual noise terms. For comparison purposes all noise sources will be referenced to the photodiode output current (see Figure A.1). This reference position is a convenient location for the comparison of both optically and electrically generated noises. The photocurrent noise can be easily related to optical power sensitivity by use of the photodiode responsivity, which is approximately 1 A/W at wavelengths around 1.55 μm. Except for a change of units, the numerical values for photocurrent and optical power are almost identical. To provide a relatively easy way for comparing the magnitude of different noise sources, the concept of relative intensity noise (RIN) will be introduced. This describes noise as a fractional value, where the noise power in a 1 Hz bandwidth is normalized by the average power.

Each section will first give a general expression for describing the noise source. After this, examples will be given to illustrate how the expressions are used and to give a feeling for their magnitudes. For those who are interested, a simple derivation will be given near the end of each section. This derivation is not intended to be rigorous, but is hoped to provide a physical understanding for the process which generates the noise. The noise associated with optical amplification will be covered in Chapter 13.

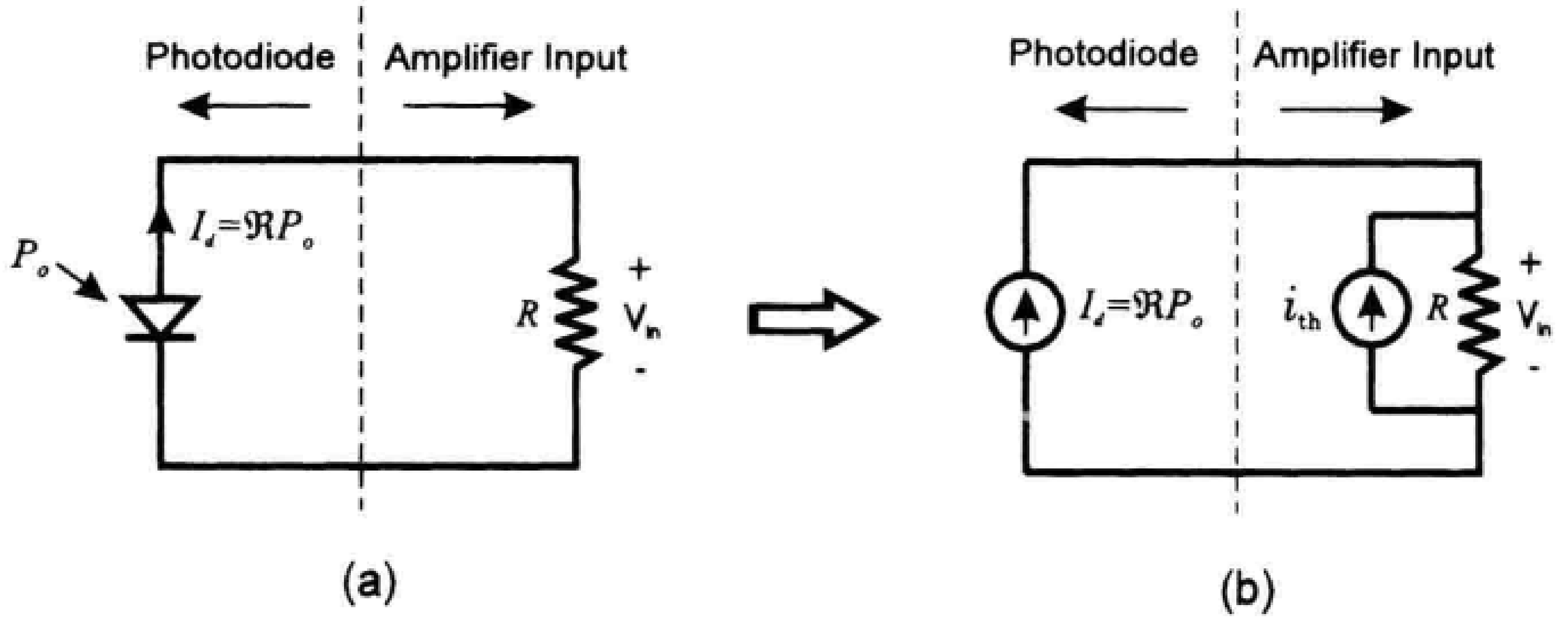

Figure A.1 (a) Simplified illustration of a photodiode connected to an electrical amplifier. (b) The equivalent circuit modeling the photodiode output and thermal resistive noise using ideal current sources.

A.1 ELECTRICAL THERMAL NOISE

One common noise source, which needs to be considered in almost every detection process, is the thermal noise generated in the receiver electronics. If the receiver amplifying process is considered ideal, so that no excess noise is generated, the resulting receiver noise will be determined by the thermal noise (also known as Johnson noise) generated by the resistance first experienced by the photocurrent. As this resistance is made larger the optical power sensitivity is improved. This result will become more evident in the following discussions.

Thermal noise from a resistor can be modeled as being generated by either a voltage or current noise source. Since the signal from a photodiode looks as if it were generated by a current source, it is more convenient to use the current noise-source model for describing thermal noise. This allows the current noise to be directly compared to the generated photocurrent.

Figure A.1a shows the basic configuration for generating a signal voltage using a photodiode and external resistor. Figure A.1b is a simplified equivalent circuit which uses current sources to model the photodiode and thermal noise generated by the resistor. For simplicity the circuit capacitances have been omitted, but they would need to be included for determining the effective noise bandwidth of the circuit. As modeled in Figure A.1b, the thermally generated rms current noise $\hat{i}_{th}$ in a 1 Hz bandwidth is given by

$$\hat{i}_{th} = \sqrt{\frac{4\,kT}{R}} \quad [A/\sqrt{\text{Hz}}] \tag{A.1}$$

where R is the resistance which the photocurrent first experiences, $k = 1.38 \times 10^{-23}$ J/K is Boltzman's constant and T is the temperature of the resistor in Kelvin. The caret above the rms current symbol is used to indicate that the current noise is normalized to a 1 Hz bandwidth. This normalized expression is useful when comparing the magnitude of the thermal noise with the other noise sources in the system. The total rms current (i_{th}) noise is obtained by multiplying Equation A.1 by the square root of the receiver bandwidth ($i_{th} = \hat{i}_{th}\sqrt{\Delta f}$).

As seen from Equation A.1, the thermal current noise (or optical power sensitivity) is reduced by making the resistance larger. This is the opposite result when considering standard, voltage-based electronic circuits. Although a larger resistor reduces receiver noise, the actual value used is usually a compromise between sensitivity and receiver bandwidth. It should be pointed out that for a transimpedance receiver, the resistance in Equation A.1 is the feedback resistance and not the effective input impedance seen by the photodiode.

In practice, the actual noise at the output of the amplifier will be larger due to the excess noise added in the amplifying process. But Equation A.1 is still useful since it predicts the best possible performance given a specific receiver impedance. The room temperature ($T \sim 300$ K) current noise for some representative values of receiver resistance are given in Table A.1

Simple Derivation. This derivation is not meant to be rigorous or complete but will try to provide a physical understanding for the magnitude of the thermal noise using a few basic concepts. The first of these concepts is that the magnitude of the noise is proportional to the degrees of freedom (or modes) that can exist within the system. Another of the concepts comes from thermodynamics which states that the thermal energy for each degree of freedom is equal to $\frac{1}{2}kT$.

First we will determine the noise power (energy per unit time) associated with the thermal energy of the resistor. This can be obtained by multiplying the thermal energy per mode by the number of modes per second that the system can respond to. The number of modes (degrees of freedom) is equal to the number of orthogonal responses possible by the electrical circuit. In the context of this problem, an electrical circuit with a bandwidth of Δf can generate $2\Delta f$ different orthogonal responses in a 1 s time interval. The factor of two comes about since at any one frequency there are two degrees of freedom corresponding to the two orthogonal phase states ($\cos(\omega t)$ and $\sin(\omega t)$). For example, an electrical

Table A.1 Thermally generated current noise for various resistance values.

R	$\hat{i}_{tn}$ *(pA/$\sqrt{Hz}$)*
50 Ω	18
100 Ω	13
1 KΩ	3.9
10 KΩ	1.3
100 KΩ	0.39
1 MΩ	0.13
10 MΩ	0.04

circuit with a bandwidth of 1 kHz can generate 2000 independent orthogonal responses in a 1 s time interval. The thermal noise power generated by a resistor is given by

$$P_{\text{thermal}} = \frac{\text{energy}}{\text{mode}} \times \frac{\text{modes}}{\text{second}} = \tfrac{1}{2}\, kT \times 2\Delta f = kT\Delta f \tag{A.2}$$

where k is Boltzman's constant and Δf is the effective noise bandwidth of the electrical circuit. At thermal equilibrium, this is the noise power that is delivered from one resistor to an equivalent matched load. It should be noted that this result is independent of the value of the resistance used in the circuit. The resistance comes in later when an equivalent current noise-source is introduced to generate this thermal noise power.

Now we will introduce a fictitious current source in parallel with the resistor which is assumed responsible for generating the thermal noise power. Figure A.2 shows two resistors connected together, each with their equivalent noise current sources. At thermal equilibrium, the noise power delivered from one resistor to the other is equal to the value $kT\Delta f$ obtained from Equation A.2. Since the two resistors are in parallel, the current source for one of the resistors delivers only half of its current to the other resistor. This value of ½ i_{th} must then be responsible for the thermal noise power $kT\Delta f$ transferred from one resistor to the other. Using this reasoning we get the relationship

$$(\tfrac{1}{2}\, i_{th})^2 R = kT\Delta f \quad [W] \tag{A.3}$$

where i_{th} is the rms current generated by the equivalent noise current source in parallel with the resistor. Rearranging Equation A.3 gives the familiar expression of

$$i_{th} = \sqrt{\frac{4kT\Delta f}{R}} \quad [A] \tag{A.4}$$

This result is valid for frequencies encountered in typical electrical circuits. At very high frequencies, where the photon energy becomes greater than the thermal energy ($h\nu > kT$) this expression is no longer valid. At room temperature this occurs for frequencies greater than about 6000 GHz ($\lambda < 48$ μm).

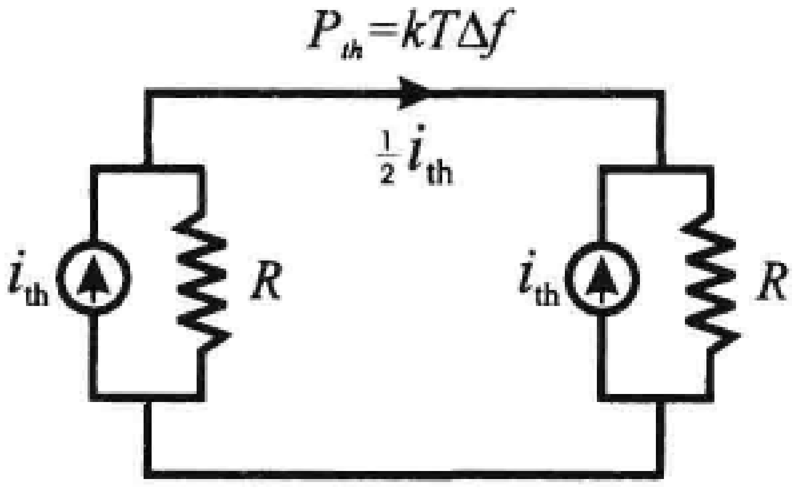

Figure A.2 Thermal noise power transfer between matched resistors at thermal equilibrium.

A.2 OPTICAL INTENSITY NOISE

Another form of noise often encountered in optical measurements is the intensity noise that exists on the optical signal even before the detection process. Intensity noise can originate from several sources. From a fundamental origin, intensity noise occurs from the optical interference between the stimulated laser signal and the spontaneous emission generated within the laser cavity. Laser sources such as distributed feedback (DFB) lasers and Fabry-Perot (FP) laser diodes typically exhibit intensity noise whose value depends on pump levels and feedback conditions. Environmentally varying external feedback can effect the stability of a laser resulting in large variations in its intensity noise.

Intensity noise also exists in nonlaser sources such as edge-emitting light-emitting diodes (EELEDs) and erbium doped-fiber amplifiers (EDFAs). These sources generate amplified spontaneous emission (ASE) whose intensity noise statistics differ from that of lasers. For ASE sources, intensity noise is generated by the interferometric beating between the various frequencies within the spectrum of the ASE. This effect is described in detail at the end of this intensity noise section.

A useful way of describing and comparing intensity noise is to express it as a ratio of noise power in a 1 Hz-bandwidth normalized by the DC signal power. This description is useful since this quantity becomes independent of any attenuation or the absolute power reaching the photodetector. This fractional noise power per bandwidth is often referred to as relative intensity noise (RIN) and is defined as

$$\mathrm{RIN} = \frac{<\Delta\hat{i}^2>}{I_{dc}^2} \quad [\mathrm{Hz}^{-1}] \tag{A.5}$$

where $<\Delta\hat{i}^2>$ is the time-averaged intensity noise power in a 1 Hz bandwidth and I_{dc} is the average DC intensity. Since RIN is a normalized parameter, Equation A.5 is equally valid if the parameters $\Delta\hat{i}$ and I_{dc} refer to optical intensity, detected photocurrent or even receiver output voltage. In practice, RIN can be easily calculated using an electrical spectrum analyzer to measure the time-averaged photocurrent noise power per unit bandwidth $<\Delta\hat{i}^2>$, and a DC ammeter to determine the average DC photocurrent, I_{dc}. The contributions caused by thermal and shot noise should be subtracted from the measured noise power to obtain a more accurate value for the actual intensity noise on the incoming optical signal.

Example

This example illustrates how a typical RIN measurement is made. The output of a DFB laser is detected by a transimpedance receiver which is connected to an electrical spectrum analyzer using a bias-tee to block the DC voltage. Using a voltmeter, the DC voltage from the transimpedance detector is measured to be 5 V. On the spectrum analyzer, the electrical noise power in a 1 Hz noise bandwidth is determined to be −118 dBm. This noise level is typically different than the displayed electrical power since it requires taking the effective noise bandwidth of the analyzer into account. Since the spectrum analyzer calculates electrical power based on a 50 ohm load, −118 dBm (1.6×10^{-15} W) corresponds to a rms noise voltage of 2.8×10^{-7} V in the 1 Hz bandwidth. Dividing this noise voltage by the above 5 V and squaring the ratio gives RIN = 3.1×10^{-15} Hz^{-1} or expressed in decibels, −145 dB/Hz. In this example, we have assumed that the optical intensity noise is the dominant noise source. If this is not the case we would need to subtract the other noise sources before calculating the RIN.

In general, RIN is a function of frequency but for cases where the noise spectrum is flat over the frequency range of interest, it is expressed as a single number. For the case of a flat noise spectrum, the total rms current noise caused by RIN is given by

$$i_{\text{rin}} = I_{dc}\sqrt{\text{RIN}\,\Delta f} \quad [A] \tag{A.6}$$

where Δf is the effective noise bandwidth of the receiver.

Special Case for ASE Sources. ASE can be generated from sources such as EELEDs, superluminescent diodes (SLD) and EDFAs. These broadband sources typically have very short coherence lengths and are important in performing wavelength dependent insertion-loss measurements (see Chapter 9) and for making optical low-coherence reflectometry measurements (see Chapter 10). The intensity noise from these broadband optical noise sources can also be used for calibrating the frequency response of wide-bandwidth photodetectors.1 They also show potential as an optical-to-electrical noise standard for calibrating the frequency response of a photodiode and electrical spectrum analyzer combination. This calibration is important when using an electrical spectrum analyzer to measure the noise figure of an EDFA.

An interesting property of these broadband optical noise sources is that their RIN depends only on their optical spectral width $\Delta\nu_{\text{ase}}$ and is approximately given by the simple expression

$$\text{RIN} \cong \frac{1}{\Delta\nu_{\text{ase}}} \quad [\text{Hz}^{-1}] \tag{A.7}$$

where it is assumed that the light is unpolarized and exists in a single spatial mode. For polarized light, the RIN is increased by a factor of two. Equation A.7 is valid for frequencies that are small compared to the spectral width of the ASE source. At higher frequencies, the intensity noise decreases in magnitude.[2] Since spectral widths can easily be in the THz range, this roll-off is often not observed on the detected photocurrent. A more complete discussion of this result is given in the simple derivation at the end of this section.

Example

Consider the ASE output from an EDFA without an input signal. Assuming the ASE has a frequency extent of 10 nm centered at 1.55 μm, the spectral width for this noise source is equal to about 1250 GHz. The RIN on this output will be approximately RIN $\cong 8 \times 10^{-13}$ Hz^{-1} or −121 dB/Hz (using Equation A.7) and can be considered spectrally flat over any practical electrical bandwidth. If this signal is sent through a 1 nm interference filter the RIN would increase 10 dB to −111 dB/Hz. This result illustrates that filtering an ASE signal causes it to become more noisy when measuring noise as a fractional quantity. For this case, the absolute noise power actually decreased but at a slower rate than the DC power. Understanding these differences can be important in certain applications.

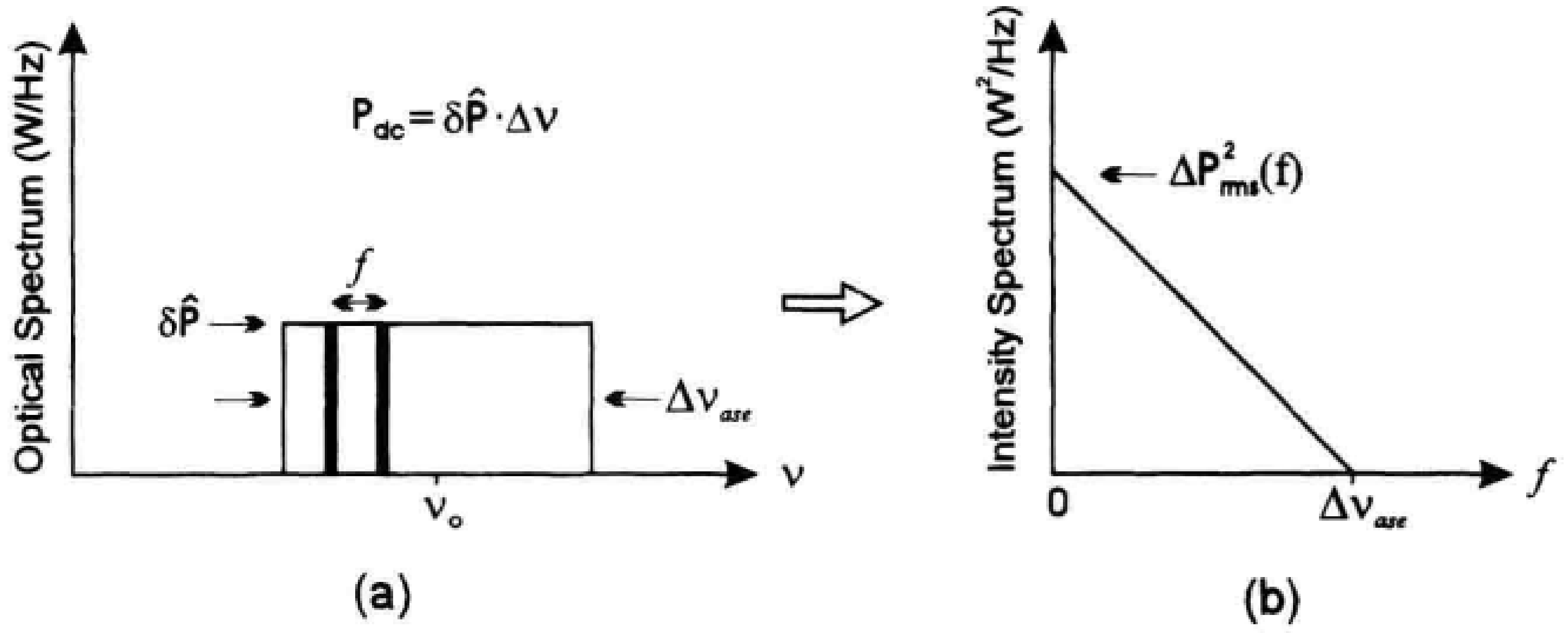

Figure A.3 (a) The optical power spectral density for a thermal light source with a rectangular shaped spectrum. (b) The resulting power spectral density for the optical intensity fluctuations.

Simple Derivation. The purpose of this derivation is to provide a physical understanding for the intensity noise that accompanies a broadband thermal-like optical noise source. These results are also valid for sources which generate ASE such as fiber amplifiers and EELEDs. This example does not describe sources such as lasers, whose statistical properties are different because of gain saturation effects caused within the laser cavity.

To make the analysis simpler, we will assume a thermal light source which has a rectangular shaped optical spectrum as shown in Figure A.3a. This spectral shape could be obtained by filtering an ASE source with a flat-topped bandpass filter such as a grating-based monochrometer. Let the optical power in a 1 Hz slice of bandwidth be given by $\delta\hat{P}$. The total cw optical power P_{dc} can be found by summing the power in all the individual 1 Hz slices to get

$$P_{dc} = \delta\,\hat{P}\Delta\nu_{\text{ase}} \quad [W] \tag{A.8}$$

where $\Delta\nu_{\text{ase}}$ is the spectral width, in Hertz, of the optical source.

Next we will determine the rms optical noise power (or noise intensity) in a 1 Hz bandwidth centered at a beat frequency f that is small compared to the spectral width, $\Delta\nu_{ase}$. The origin of this intensity noise comes from optical interference or beating between the various 1 Hz spectral slices what make up the optical spectrum. This is sometimes referred to as spontaneous-spontaneous beat noise.[2] The first step in calculating the total rms noise power is to determine the rms power from the beating of just two of the many 1 Hz spectral slices. After this, all these contributions will be summed to get a total rms noise value. Assuming a polarized optical signal from a singlemode fiber, the rms noise from just two of the spectral slices (separated by a frequency f) is given by

$$\Delta\hat{P}_2(f) = \, < [2\sqrt{\delta\hat{P}\delta\hat{P}}\cos(2\pi ft)]^2 >^{\frac{1}{2}} = \sqrt{2\delta\hat{P}\delta\hat{P}} \quad [\text{W/Hz}] \tag{A.9}$$

where f is the base-band frequency at which the intensity beating occurs.

To calculate the total rms noise power at a given frequency f, all the spectral slices separated by f need to be combined together. For small values of the frequency spacing, the total number of pairs of 1 Hz slices that can beat together is approximately equal to the spectral width $\Delta\nu_{ase}$. Since these noise contributions are uncorrelated, the total value will increase as the square root of the number of individual beating terms ($\sqrt{N} \approx \sqrt{\Delta\nu_{ase}}$). Using this reasoning we can write the total rms noise power in a 1 Hz bandwidth as

$$\Delta\hat{P}_{rms}(f) \cong \sqrt{2\delta\hat{P}\delta\hat{P}} \cdot \sqrt{\Delta\nu_{ase}} \quad [\mathrm{W/Hz^{-1/2}}] \tag{A.10}$$

where it is assumed that the frequency spacing f between beating terms is small compared to the optical spectral width ($f << \Delta\nu_{ase}$). Since optical spectral widths can be greater than 1000 GHz, this assumption can be valid over the entire rf electrical spectrum. For larger frequencies, the noise drops off since there are less terms that can be mixed together to generate the larger beat frequencies. Figure A.3b shows a plot of $\Delta^2_{Prms}(f)$ as a function of frequency. This quantity would be displayed on an electrical spectrum analyzer when measuring the detected photocurrent. For frequencies above $\Delta\nu_{ase}$, there is no intensity noise since the frequency slices would need to be spaced further than the spectral width of the source.

The peak RIN is found by taking the ratio of Equations A.10 and A.8 and squaring the result.

$$\mathrm{RIN} = \frac{\Delta P^2_{rms}(f)}{P^2_{dc}} \cong \frac{2}{\Delta\nu_{ase}} \quad [\mathrm{Hz^{-1}}] \tag{A.11}$$

This result is valid for the case of polarized light and for frequencies much less than the spectral width of the source ($f << \Delta\nu_{ase}$). If the light source was unpolarized, the RIN would be decreased by a factor of two and we would get the result given in Equation A.7. The decrease in RIN for unpolarized light can be understood by considering the effect of adding an additional uncorrelated (orthogonally polarized) signal of equal power. The total power would double but the noise power would increase by only $\sqrt{2}$, therefore resulting in a smaller RIN. If the spectral shape of the broadband noise source is not rectangular, the RIN will be modified slightly. For the cases of a Gaussian and Lorentzian shaped spectrum, Equation A.11 should be multiplied by 0.66 and 0.32 respectively.[2] For this result, $\Delta\nu_{ase}$, is measured as the full-width-half-maximum (FWHM) spectral width of the source.

One interesting way to think of the RIN from an ASE source is in terms of degrees of freedom. That is, the fractional intensity noise in a 1 Hz bandwidth is inversely proportional to the degrees of freedom the optical signal possesses in a one second time interval. This concept can be useful in predicting how the RIN will change under various conditions. For example, it tells us that if we remove half the degrees of freedom by polarizing an unpolarized signal, the RIN will increase by a factor of two. It also tells us that if a spatially incoherent broadband source (for example, a surface-emitting LED or a Tungsten lamp) excites a multimode fiber the result given by Equation A.11 should be reduced by the number of spatial modes in the fiber.

A.3 PHOTOCURRENT SHOT NOISE

Electrical shot noise occurs because of the random arrival time of the electrons that make up an electrical current. It usually becomes an important noise source when trying to measure a small signal in the presence of a large DC background. This case normally occurs in coherent detection schemes where a small AC current is being measured in the presence of the large background due to the DC local oscillator current. The rms shot-noise current in a 1 Hz bandwidth is given by

$$\hat{i}_{\text{sn}} = \sqrt{2qI_{\text{dc}}} \quad [A/\sqrt{\text{Hz}}] \tag{A.12}$$

where $q = 1.6 \times 10^{-19}\ C$ is the charge of an electron and I_{dc} is the DC photocurrent. Without frequency filtering, shot noise is spectrally flat and therefore has the above value at each measurement frequency. To calculate the total rms shot noise current (i_{sn}) for an electrical circuit with an effective noise bandwidth (Δf), Equation A.12 should be multiplied by the square root of the bandwidth ($i_{\text{sn}} = \hat{i}_{\text{sn}}\sqrt{\Delta f}$).

An interesting observation can be made when comparing shot noise with thermal noise. Since the shot-noise level depends on signal current, there will be a point for increasing DC current when the shot-noise value exceeds the fixed thermal noise. It turns out that for a photodiode feeding into a resistor, the shot noise starts to exceed the thermal resistor noise when the voltage across the resistor becomes larger than 52 mV. This voltage level is independent of the value of the resistor. This result is useful in practice since it provides an easy method for determining which of the two noise sources is dominant. If the amplifying process generates excess noise, the value of 52 mV needs to be increased accordingly. Another point to mention is the special meaning that the shot-noise limit has in a coherent detection process. In this regime, the receiver has optimum sensitivity with a noise equivalent power equal to a single photon per integration time of the receiver.

Although RIN is defined as the fractional intensity noise on an optical signal (see Equation A.5), it can also be used in a nonconvential way to describe the level of shot-noise on a dc photocurrent. By dividing the shot-noise current by the dc current and squaring the result, we get an expression equivalent to RIN. Expressing the shot noise this way, allows easy comparisons with other noise sources expressed in a similar manner. Using Equations A.5 and A.12, shot noise produces an effective RIN given by

$$\text{RIN}_{\text{sn}} = \frac{2q}{I_{\text{dc}}} \quad [\text{Hz}^{-1}] \tag{A.13}$$

This result is useful for determining the required dc photocurrent needed to make an accurate RIN (see Section A.2) measurement on an optical signal. The RIN_{sn} decreases with dc photocurrent while the true optical RIN is independent of the dc signal. To make an accurate RIN measurement, one must ensure that a large enough dc photocurrent is detected to prevent shot noise from being the dominant noise source. For example, to measure a RIN of −155 dB/Hz on a DFB laser requires a photocurrent on the order of $I_{\text{dc}} = 1$ mA or greater. Representative values of shot noise for different dc photocurrents are shown in Table A.2.

Table A.2 Representative shot-noise values.

I_{dc}	i_{sn} $(pA/\sqrt{Hz})$	RIN_{sn} (dB/Hz)
100 nA	0.18	−115
1 μA	0.57	−125
10 μA	1.8	−135
100 μA	5.7	−145
1 mA	18	−155

Simple derivation The following discussion shows a simple derivation for the shot-noise expression given in Equation A.12. Shot noise can be thought of as being generated by the random arrival time of electrons that make up a dc photocurrent. Figure A.4 illustrates this random arrival-time process. Each vertical arrow represents the detection of a single particle at a specific time. In a nonrigorous manner these particles could also be photons, but for the purpose of this derivation they will be assumed to be electrons. The above random arrival time can be described by a Poisson probability process. This type of process has the characteristic that in any given time interval, the variance (or rms uncertainty) in the number of electrons is equal to the square root of the average number.

$$\Delta N_{\text{rms}} = \sqrt{N} \tag{A.14}$$

This variation in the average number of arriving electrons during any specified time interval leads to the generation of shot-noise. The rms shot noise current can be written as the rms variation in detected charge per unit time as

$$i_{\text{sn}} = \frac{q\Delta N_{\text{rms}}}{\Delta t} \quad [A] \tag{A.15}$$

where q is the charge of the electron and Δt is the measurement time interval. The dc photocurrent can be expressed in a similar manner using the average number of electrons per time interval as

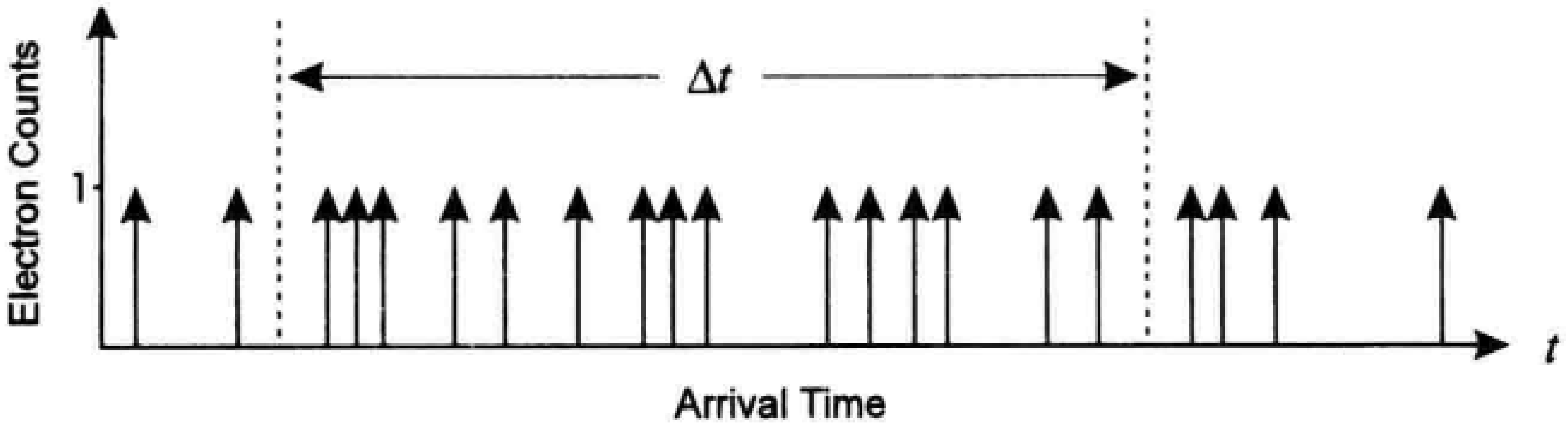

Figure A.4 Random arrival time of photogenerated electrons.

$$I_{dc} = \frac{q\bar{N}}{\Delta t} \quad [A] \tag{A.16}$$

This result allows us to express the rms shot noise current in terms of the dc current using the above three equations.

$$i_{sn} = \sqrt{\frac{qI_{\mathrm{dc}}}{\Delta t}} \quad [A] \tag{A.17}$$

To put this expression into a more commonly used form, we must relate the measurement time interval to an equivalent noise bandwidth. Using Fourier analysis it can be shown that the effective noise bandwidth Δf of a flat-topped rectangular gate function of width Δt is given by

$$\Delta f = \frac{1}{2\Delta t} \quad [\mathrm{Hz}] \tag{A.18}$$

With this result we can now convert Equation A.17 into the familiar expression

$$i_{\mathrm{sn}} = \sqrt{2qI_{\mathrm{dc}}\Delta f} \quad [A] \tag{A.19}$$

which is equivalent to the result given in Equation A.12.

An equivalent argument can be made for the shot-noise intensity on an optical signal by considering photons instead of electrons. Now the random arrival time of the photons leads to a fluctuation in the optical power. For this situation, the above equations can be rewritten by replacing the electrical charge with the photon energy ($q \rightarrow h\nu$) and the current with the optical power ($I_{\mathrm{dc}} \rightarrow P_{\mathrm{cw}}$). When using this classical concept to describe photons, care must be used since it is not rigorous in a quantum mechanical sense and can lead to incorrect results.

Squeezed States As a final comment on shot-noise, an attempt will be made to describe the concept of optical squeezed states.^{3} Squeezed states is a quantum mechanical concept describing the reduction in the "optical shot-noise" on a cw optical signal. Or in other words, removing the randomness in the arrival time (see Figure A.4) of photons and thereby decreasing the associated optical intensity noise. Squeezed states makes use of the uncertainty principle between the position and momentum (in other words, frequency) of a photon. The uncertainty in the photon position can be reduced at the expense of increasing the uncertainty in the photon frequency.

This concept can be understood by replacing the electrons in Figure A.4 with photons. This can be rationalized since for the case of a 100% quantum efficiency detector, there is a one-to-one correspondence between the input photons and the generated electrons. By producing a more equal spacing between photons, the intensity noise is reduced since the uncertainty in the number of photons in a given measurement time becomes less than $\sqrt{\bar{N}}$. The process of "squeezing" the intensity fluctuations out of an optical signal requires that the positions of the individual photons become well defined. Due to the uncertainty principle, this increases the uncertainty of the photon frequency (or momentum) which leads to a broadening of the optical bandwidth. The more the intensity noise is reduced the larger the optical bandwidth becomes. Although squeezed states have been demonstrated experimentally, reducing the shot noise by more than a several dB becomes extremely difficult.[3]

A.4 OPTICAL-PHASE-NOISE TO INTENSITY-NOISE CONVERSION

The conversion of optical phase noise (frequency fluctuations in the optical carrier) into intensity fluctuations occur when multiple reflectors cause time-delayed portions of the optical signal to interfere with each other. This situation is troublesome whenever small signals must be measured in the presence of large background signals. Phase noise can cause degradation in certain types of communication schemes and reflectometry measurement techniques. In reflectometry applications, phase noise can be important in coherent optical frequency domain techniques, where small sinusoidal signals must be measured in the presence of larger background signals. In this section, we discuss the conversion of phase noise into intensity noise for both the incoherent and coherent cases. These cases are distinguished by comparing the coherence time of the source to the differential delays between the interfering optical signals.

Figure A.5a shows the relationship between optical frequency variations and the detected photocurrent after an optical signal is split and recombined with a relative delay τ_o. This interferometric conversion of frequency variations to intensity variations, is a char-

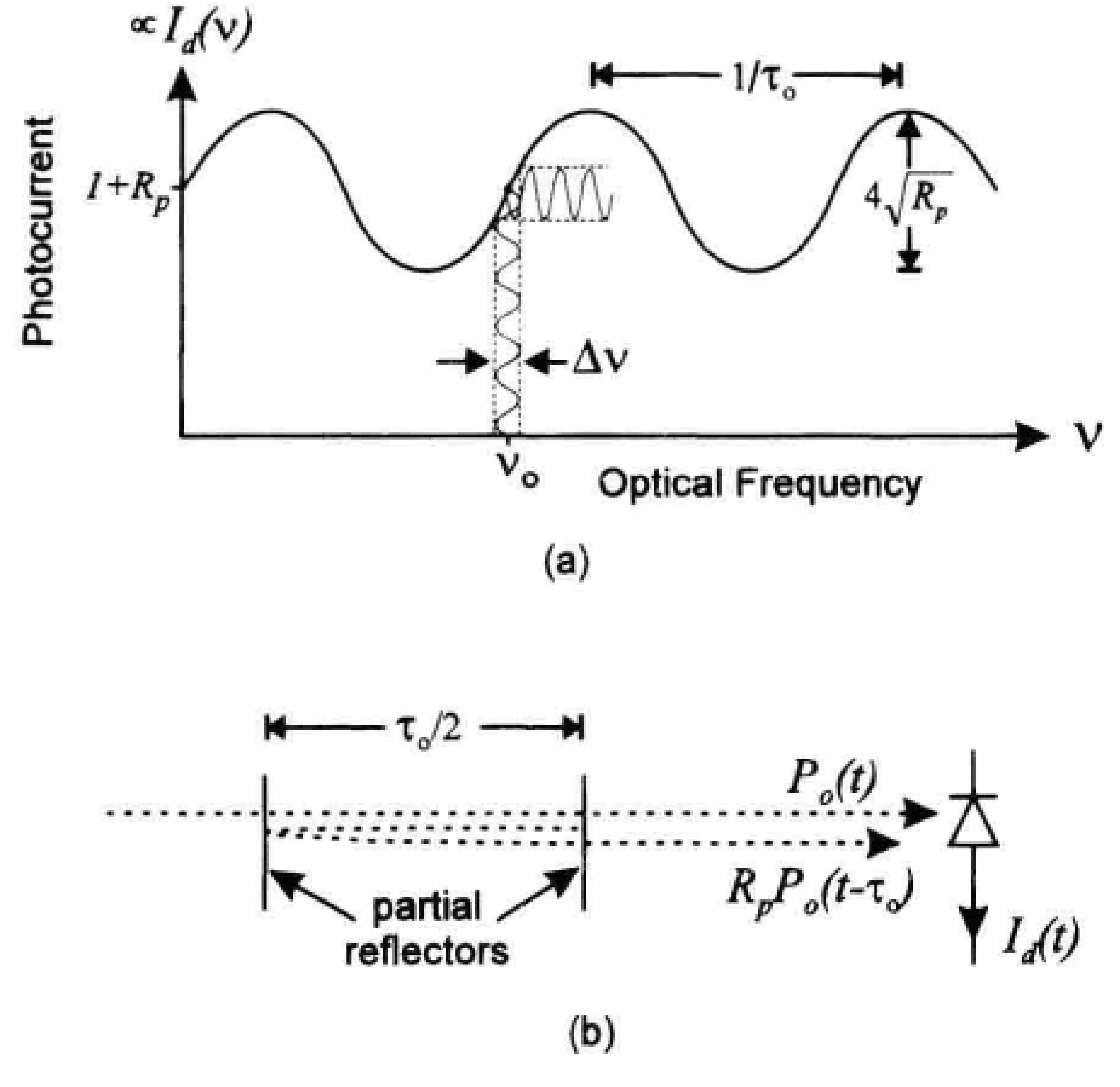

Figure A.5 (a) Conversion of optical frequency fluctuations into intensity variations due to the coherent interference between time-delayed signals. (b) Interfering signals generated by a pair of partial reflectors.

acteristic of optical circuits such as Michelson and Mach-Zehnder interferometers. These effects can also occur after a laser signal passes through weak etalons caused by unwanted reflections in a transmission link (see Figure A.5b). The detected photocurrent for a cw laser signal that passes through one of the above interferometers can be written as:

$$I_d(t) = \mathfrak{R}\, P_o[1 + R_p + 2\sqrt{R_p}\cos(2\pi\tau_o\nu(t))] \quad [A] \tag{A.20}$$

where $\mathfrak{R}$ is the responsivity of the photodetector, P_o is an optical power, τ_o is the differential time delay, R_p is the ratio of the two interfering optical powers and $\nu(t)$ is the instantaneous optical frequency of the laser source. See Chapter 5.2 for a derivation of this equation. Since Equation A.20 describes a coherent interference effect, it is assumed that the coherence time of the laser is longer than the differential time delay, τ_o. This equation also assumes identical polarization states for the two mixing signals.

As shown in Figure A.5, if the optical carrier frequency is centered at the location of maximum slope (quadrature position), the fractional intensity change due to a small frequency change $\Delta\nu(t)$ is given by

$$\frac{\Delta I(t)}{I_{\text{avg}}} \cong K_{\text{fm}}\,\Delta\nu(t) \tag{A.21}$$

where $K_{\text{fm}} = 4\pi\tau_o\sqrt{R_p}/(1 + R_p)$ is the maximum slope from Equation A.20 and can be thought of as the FM discriminator constant. Since the above expression is a linear approximation obtained from a nonlinear expression, it is only valid if constraints are put on $\Delta\nu(t)$. Restrictions on both the magnitude and modulation frequency of $\Delta\nu(t)$ are required. To keep the accuracy of Equation A.21 to better than 10%, the constraint of $\Delta\nu < 0.1/\tau_o$ should be met. See Chapter 5.3.4 for more details on the constraints assumed for Equation A.21.

Example

Consider a DFB laser in a FSK communication link which uses 1 GHz frequency shifts in the optical carrier frequency. Assume the frequency modulated signal has to pass through a poorly constructed optical component with two Fresnel reflections (each with a reflectivity of 4%) spaced by 1 cm in air. From this information we get $\tau_o \cong 67$ psec, $R_p \cong (.04)^2$, and $\Delta\nu = 1$ GHz. Putting these values into Equation A.21, the resulting modulation or noise on the transmitted power is about 3.4%. Since the magnitude of this modulation signal is not constant but changes with polarization and bias position, this type of noise can cause difficulties in predicting system performance.

Coherent Interference. The above FM discriminator process can also convert a laser linewidth into a spectral noise density on the detected photocurrent. The term "coherent interference" assumes that the coherence length of the laser is much longer than the differential distance experienced by the interfering signals. An expression for the maximum RIN due to the conversion of phase noise into intensity noise is given by

$$\text{RIN}_{\Delta\phi} \cong \frac{2R_p}{(1 + R_p^2)}\, 8\pi\tau_o^2\,\Delta\nu_{\text{lw}}\,\text{sinc}^2(\tau_o f) \quad [\text{Hz}^{-1}] \tag{A.22}$$

where the laser lineshape is assumed to be Lorentzian with a linewidth equal to $\Delta\nu_{\mathrm{lw}}$ and the function sinc $(x) = \sin(\pi x)/\pi x$ is used. R_p and τ_o are the same as described in Equation A.20 and A.21. To obtain the maximum value described by Equation A.22, both a quadrature phase relation and matched polarization states are assumed for the two interfering signals. The baseband frequency modulation of the photocurrent is described using the rf frequency variable f. For the assumption of coherent interference to be reasonably valid the constraint of $\Delta\nu_{\mathrm{lw}} < 0.1/\tau_o$ should be met. One practical difficulty with this type of noise is that it can fluctuate between its maximum value given by Equation A.22 and zero depending on the environmental variations in the bias condition shown in Figure A.5. This can result in considerable difficulties when trying to trouble shoot noise problems in optical instruments and communication systems.

Incoherent Interference. Another situation that has a relatively simple analytical description is the incoherent case. Incoherent interference occurs when the coherence length of the laser is much shorter than the differential distance experienced by the two interfering signals. For this situation, the relative intensity noise due to the conversion of laser phase noise to intensity fluctuations is given by

$$\mathrm{RIN}_{\Delta\phi} = \frac{2R_p}{(1 + R_p^2)} \frac{2}{\pi\Delta\nu_{\mathrm{lw}}} \frac{1}{1 + (f/\Delta\nu_{\mathrm{lw}})^2} \quad [\mathrm{Hz}^{-1}] \tag{A.23}$$

where the laser lineshape is again assumed Lorentzian and R_p is equal to the optical power ratio of the two interfering signals. For the assumption of incoherent interference to be valid, the condition $\Delta\nu_{\mathrm{lw}} >> 1/\tau_o$ should be met. The expression in Equation A.23 assumes matched polarization states for maximum interference. If the polarizations states are orthogonal this noise effect goes to zero. Unlike the results given in Equations A.21 and A.22, the assumption of incoherent interference makes the above result independent of environmental changes in the bias of the interferometer. This means that the noise spectrum is much more stable, being independent of path length changes of the interferometer. Using Equation A.23, the laser linewidth can be determined by measuring the 3 dB bandwidth of the current noise spectrum. This technique is often referred to as a delayed self-homodyne linewidth measurement (see Chapter 5.3.3).

Figure A.6 shows the shapes for the power spectral density of the optical intensity noise for both the coherent and incoherent interference cases. The two curves are log plots of Equations A.22 and A.23. For a fixed laser linewidth, the largest low-frequency intensity noise occurs for the incoherent case. Although the noise level for the coherent case is smaller, it can extend to much higher frequencies (much higher than the linewidth of the laser). For the case of partially coherent interference, the noise spectrum will fall somewhere between the coherent and incoherent spectrums plotted in Figure A.6. A more complete result, which is also valid for the case of partial coherence, can be found in Chapter 5.3.4.

An interesting result can be noted for the case of incoherent interference described by Equation A.23. The intensity noise spectrum, assuming equal interfering powers ($R_p = 1$), is identical to that obtained from a thermal-like optical noise source as described near the end of Section A.2. This makes sense intuitively since incoherent interference

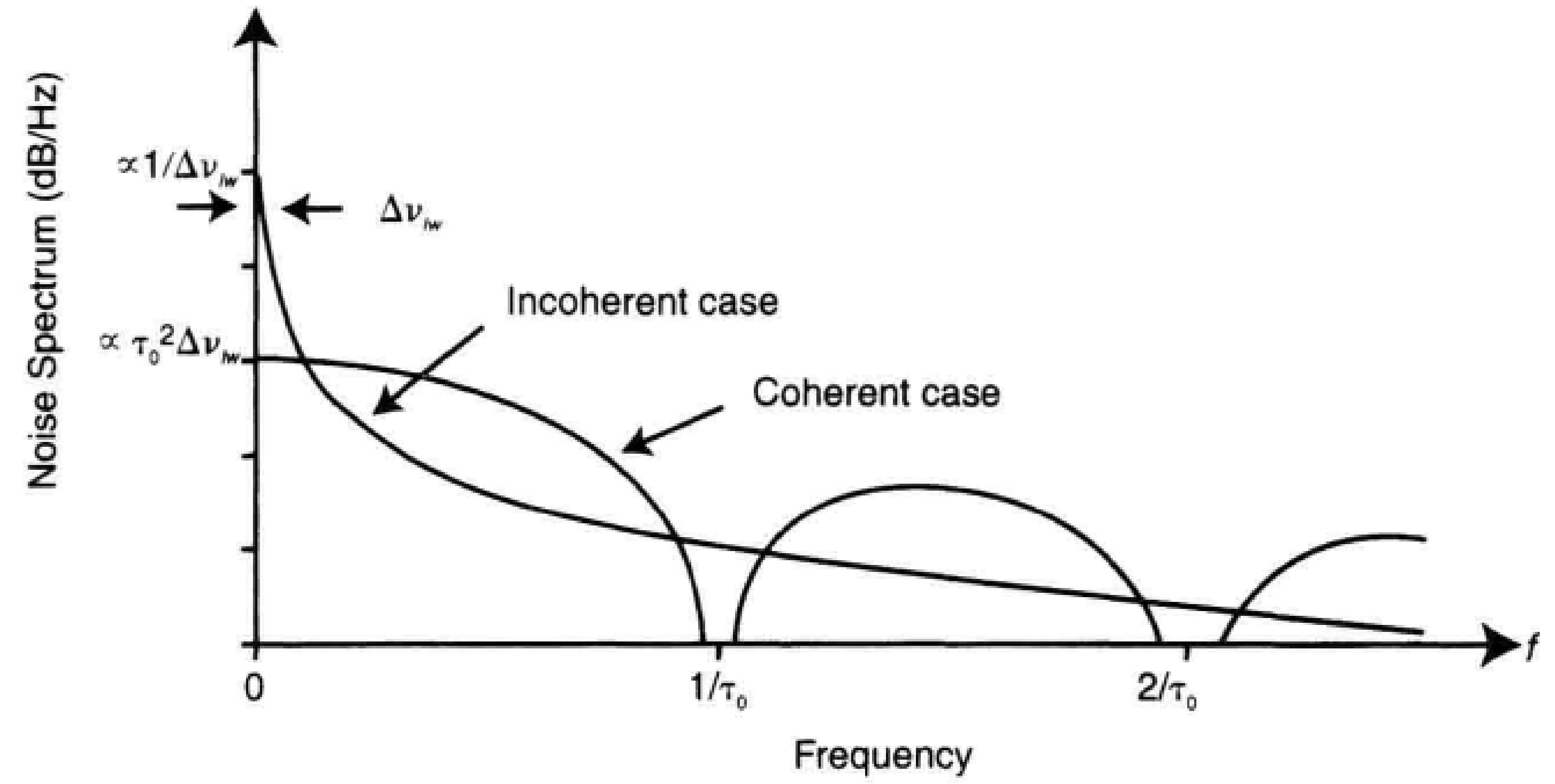

Figure A.6 Power spectral density resulting from the conversion of laser phase-noise into optical intensity noise.

with two equal powers gives a maximally randomized noise signal which is the same as for the case of a thermal noise source. Assuming Lorentzian-shaped optical spectrums, the low-frequency RIN for either case is equal to $2/\pi\Delta\nu_{\text{lw}}$ (Equation A.11 modified for a Lorentzian spectrum).

Example

Consider the case of a cw DFB laser with a Lorentzian linewidth of 50 MHz. The laser signal passes through two 4% reflections spaced by 10 cm before reaching a photodetector. For this situation, we have the case of coherent interference and Equation A.22 can be used. Using $\tau_o = 667$ psec, $R_p = (.04)^2$ and $\Delta\nu_{\text{lw}} = 50$ MHz, Equation A.22 gives a maximum low frequency $\text{RIN}_{\Delta\phi}$ of -117 dB/Hz. This phase-induced intensity noise can dominate over the actual DFB intensity noise which is often on the order of -145 dB/Hz. Also, as mentioned above, this noise can fade in and out depending on environmental variations or shifts in the central laser frequency. The 3 dB bandwidth for this phase noise is determined by the "sinc" function and would be about 750 MHz. In contrast, consider the same two reflectivities (perhaps from two fiber connectors) but now separated by 50 m. For this situation, the interfering signals will be incoherent and the low-frequency phase noise calculated from Equation A.23 becomes $\text{RIN}_{\Delta\phi} = -104$ dB/Hz. This noise spectrum has a 3 dB bandwidth of 50 MHz and its magnitude and shape remains relatively stable, independent of environmental drifts.

As the above example illustrates, phase noise can be a dominant noise source. Due to its environmental dependence it may go unnoticed in an initial system test only to become a problem at a later time. The above equations can be used to estimate the maximum effects of phase noise. In practice, optical reflectometry can be used to estimate the optical reflectivities and their associated time delays which are needed to solve these equations. Combining the measured reflectivities and differential time delay with the spectral linewidth of the laser allows Equations A.22 and A.23 to be calculated.

A.5 SUMMARY

The four noise sources studied in this appendix represent the most common noise sources associated with optical detection. For simplicity, each noise source was considered separately. In real situations, all the individual noise sources need to be combined to determine the total noise level for the detection system. Since the above noises are uncorrelated with each other, the total rms photocurrent noise (i_{total}) is given by summing their squares and then taking the square root. This procedure is shown analytically as

$$i_{\text{total}} = \sqrt{\frac{4kT\Delta f}{R} + 2qI_{\text{dc}}\Delta f + I_{\text{dc}}^2\text{RIN}\,\Delta f + I_{\text{dc}}^2\text{RIN}_{\Delta\phi}\,\Delta f} \quad [A] \tag{A.24}$$

(thermal) (shot) (intensity) (phase)

where the definitions of the parameters can be found in the previous four sections. To keep the expression simple, each noise term is assumed spectrally flat over the bandwidth Δf. If this is not the case, a separate integration over frequency would be required for each term under the square root sign.

Figure A.7 shows the graphical result of combining several of the above noise sources for a high-speed communications receiver. The receiver consists of a room-temperature reversed-biased *pin* photodetector connected to a load impedance of 1 KΩ.

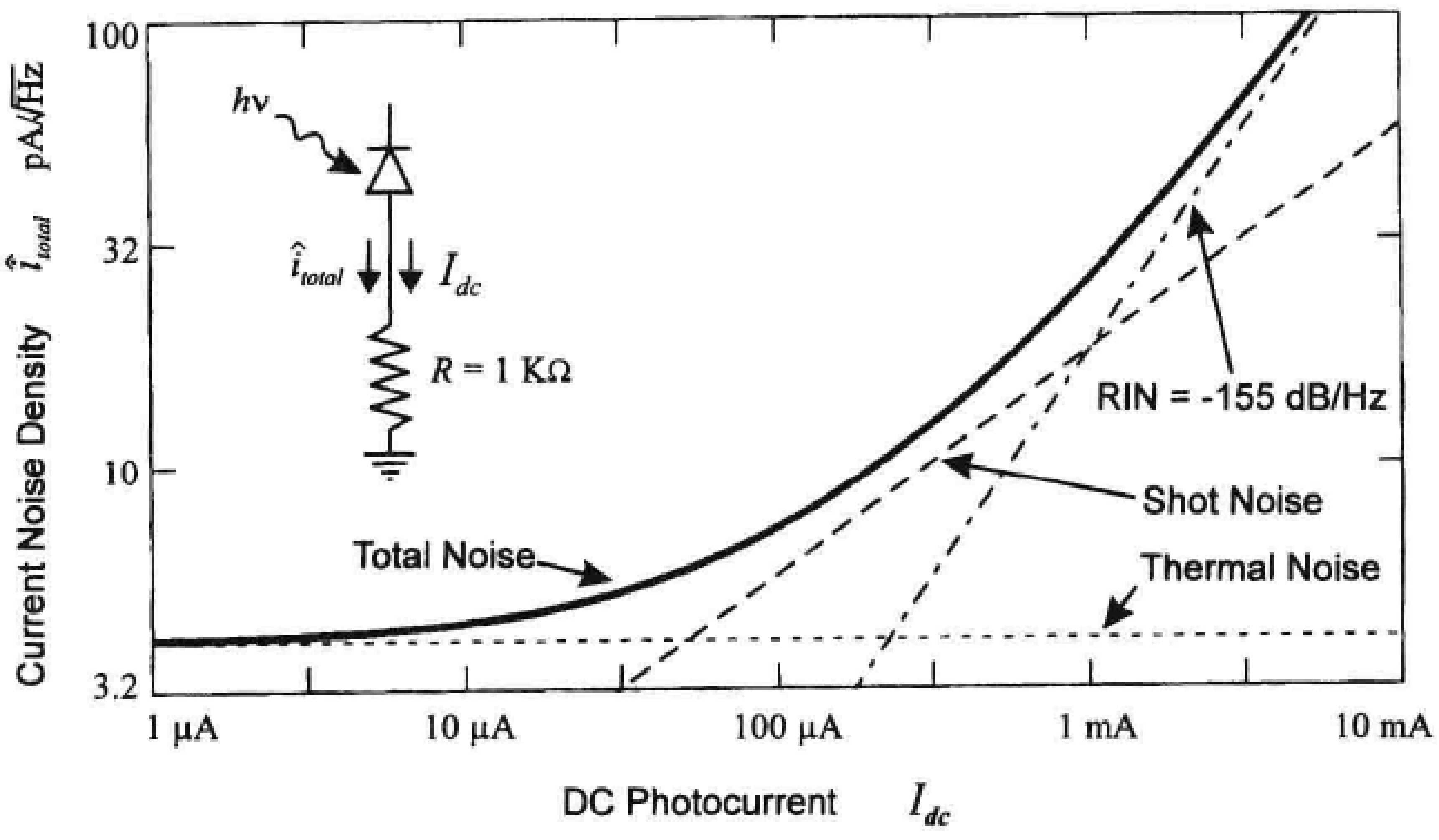

Figure A.7 Total rms photocurrent noise normalized to a 1 Hz bandwidth, caused by the combined effects of thermal, shot, and intensity noise.

To reduce the complexity of the example, the amplification of the photocurrent is assumed ideal so all of the post-detection noise is generated by the thermal noise of the 1 KΩ load resistance. Only the first three noise terms (thermal, shot, and intensity) in Equation A.24 are considered. The optical source is assumed to be a DFB laser with a RIN of −155 dB/Hz. Figure A.7 shows the rms current noise in a 1 Hz bandwidth, as a function of the dc photocurrent. Each of the three noise terms are plotted separately along with the total noise as computed using Equation A.24. For low power levels ($I_{dc} < 52\ \mu A$) the noise is dominated by the thermal noise of the load impedance. For dc currents between 52 μA and 1 mA, the shot noise dominates. And for currents in excess of 1 mA the intensity noise from the DFB source is dominant.

The sensitivity of the receiver to optical power changes can be determined using the total noise current given by Equation A.24. This is simply calculated using

$$\Delta P_{\text{min}} = \frac{i_{\text{total}}}{\mathcal{R}} \quad [W] \tag{A.25}$$

where $\mathcal{R}$ represents the responsivity (in units amps/watts) of the photodiode. This minimum power sensitivity depends on the square root of the detection bandwidth as shown in Equation A.24.

Example

This example determines the sensitivity of a receiver in the presence of a large dc optical power. Consider the case of a reverse-biased photodiode connected to an electrical circuit with an effective noise bandwidth of 500 MHz. Suppose the incident optical power is $P_o = 1.25$ mW and the resulting photocurrent is $I_{dc} = 1.0$ mA. From these values the photodiode responsivity is calculated to be $\mathcal{R} = I_{dc}/P_o = 0.8$ A/W. Assuming that the dominant noise source is the shot noise from the 1 mA dc current, Table A.2 gives a rms noise current density of 18 $pA/\sqrt{Hz}$. Multiplying this value by the square root of the noise bandwidth gives a total rms current noise of $i_{\text{total}} = 0.4\ \mu A$. Equation A.25 can now be used to calculate a receiver sensitivity of 0.5 μW. This sensitivity corresponds to a modulation depth in the input power of 4×10^{-4}.

REFERENCES

1. Baney, D.M., W.V. Sorin, and S.A. Newton. 1994. High-frequency photodiode characterization using a filtered intensity noise technique. *Photon. Tech. Lett.*, 6:1258–1260.
2. Baney, D.M. and W.V. Sorin. 1995. Broadband frequency characterization of optical receivers using intensity noise. *Hewlett-Packard Journal,* 46:6–12.
3. Yamamoto, Y. and W.H. Richardson. 1995. Squeezed States: a closer look at the amplitude and phase of light. *Optics & Photonics News:* 24–29.

APPENDIX

B

Nonlinear Limits for Optical Measurements

Wayne V. Sorin

Nonlinear effects limit the maximum power that can be transmitted along an optical fiber. This maximum power sets limits on transmission distances and measurement ranges. For example, the ultimate dynamic range for an optical reflectometry measurement is set by the maximum probe power and the receiver sensitivity. Being able to estimate the maximum power that can be transmitted along an optical fiber allows instrument designers to predict the ultimate performance of various measurement techniques. This appendix gives a brief physical description of some of the basic nonlinear effects commonly experienced in fiber optic transmission links. Simplified analytical expressions are presented, allowing maximum power levels to be estimated. Approximate numerical values will be given for standard step-index telecommunications fiber (numerical aperture ~ 0.1) at 1.55 μm. To obtain accurate power limits for specific measurement cases, a more in-depth analysis will probably be required. The provided references[1,2] may help develop a fuller understanding of these nonlinear effects.

B.1 RAMAN LIMIT

Raman nonlinearities occur when a strong optical signal excites molecular resonances within the optical fiber. These molecular vibrations modulate the incident light to generate new optical frequencies. Besides generating new frequencies, these same molecular vibrations also provide optical amplification for the newly generated light. At room temperature, the majority of these new frequencies are generated on the lower frequency side (longer-wavelength side) of the optical carrier. For silica glass, the peak of these new frequencies occurs at about 13 THz below the optical-carrier frequency. This corresponds to a wavelength shift of about 100 nm for signals at 1.55 μm resulting in newly generated wavelengths around 1.65 μm.

The critical power for the Raman nonlinearity is defined as the point where one half of the input signal is lost to newly generated frequencies. Since this critical power depends on the interaction length along the fiber, it is convenient to express this Raman limit as a power-length product. This power-length product can be written as[1]

$$P_{cr} L_{\text{eff}} \cong 16 \frac{A_{\text{eff}}}{g_R} \sim 17 \text{ W} \cdot \text{km} \tag{B.1}$$

where A_{eff} is the effective area of the guided mode, g_R is the Raman gain coefficient, P_{cr} is the critical optical power and L_{eff} is the effective fiber length. The value of 17 W · km is obtained using the values of $g_R = 6.5 \times 10^{-14}$ m/W and $A_{\text{eff}} = 70\ \mu\text{m}^2$ (mode diameter ~ 9.4 μm) and is given as a representative value for standard telecommunications fiber at 1.55 μm. This result means that if a 17 W signal is coupled into a 1 km length of fiber, the output will consist of about 8.5 W of the original signal and 8.5 W of newly generated frequencies.

A few comments should be made about the effective fiber length used in Equation B.1. For short fiber lengths, this will usually be equal to the physical fiber length. If the fiber is very long, fiber attenuation will limit the effective length. For this situation, the effective length can be calculated using the expression

$$L_{\text{eff}} = \frac{1}{\alpha}(1 - e^{-\alpha L}) \tag{B.2}$$

where L is the physical fiber length and α is the fiber attenuation constant. For a fiber loss of 0.2 dB/km, the attenuation coefficient is $\alpha = 4.6 \times 10^{-5}\ \text{m}^{-1}$. This means that a very long fiber, with 0.2 dB/km attenuation, has a maximum effective length of about 21 km. Attenuation is not the only parameter that can limit the effective length. When the optical pump consists of short pulses, fiber dispersion can also set a limit for the effective length. For this case, the effective length will be equal to the walk-off distance between the input pulse and the newly generated Raman frequencies. After the Raman signal no longer spatially overlaps the input pulse, it stops experiencing Raman amplification and, therefore, stops extracting energy from the input pulse.

Besides generating new frequencies, a strong optical signal can provide gain for nearby wavelengths. In applications where high-powered 1480 nm lasers are used to remotely pump erbium-doped fiber amplifiers (EDFAs), significant optical gain can occur for communication signals at 1.55 μm. An experimental demonstration of this effect is shown in the upper part of Figure B.1 A pump power of 150 mW at 1480 nm is launched into a long communications-grade optical fiber. The Raman gain is probed using the amplified spontaneous emission (ASE) from an EDFA. The lower portion of Figure B.1 shows the internal Raman gain as a function of wavelength. The internal gain was measured by recording the change in signal strength when the pump power was turned off and on. For this particular experiment, the peak Raman gain was 8 dB centered at about 108 nm (13.8 THz) from the pump wavelength. The 3 dB gain bandwidth was about

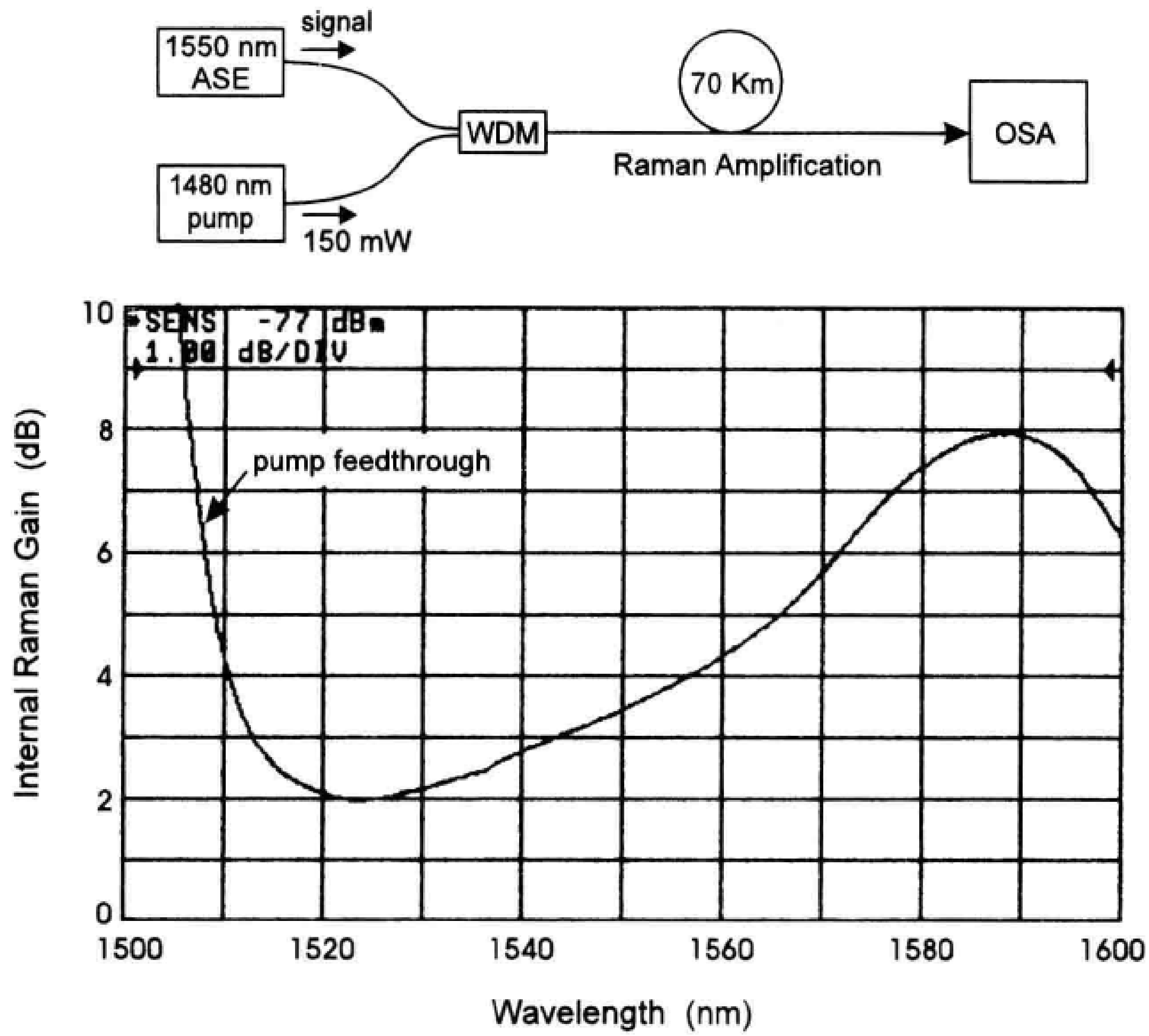

Figure B.1 Raman amplification of a broadband ASE probe signal. High-power lasers at 1480 nm are typically used for remote pumping of erbium-doped fiber amplifiers.

40 nm (5.3 THz). For more information on Raman gain, see Chapter 13 which discusses optical amplification.

B.2 SELF-PHASE MODULATION

High optical intensities temporarily change the refractive index of the optical fiber. The relationship between the optical intensity, I, and fiber index change, δn, can be written as

$$\delta n = n_2 I \tag{B.3}$$

where n_2 is the nonlinear Kerr coefficient. For standard singlemode silica fiber, the Kerr coefficient has been measured to be approximately 2.3×10^{-20} m^2/W.[3] The optical intensity is equal to the guided power divided by the effective mode area (in other words, $I = P/A_{\text{eff}}$). For a high-intensity input pulse, the Kerr effect results in a time-changing index which causes a self-induced phase modulation of the input pulse. This phase modu-

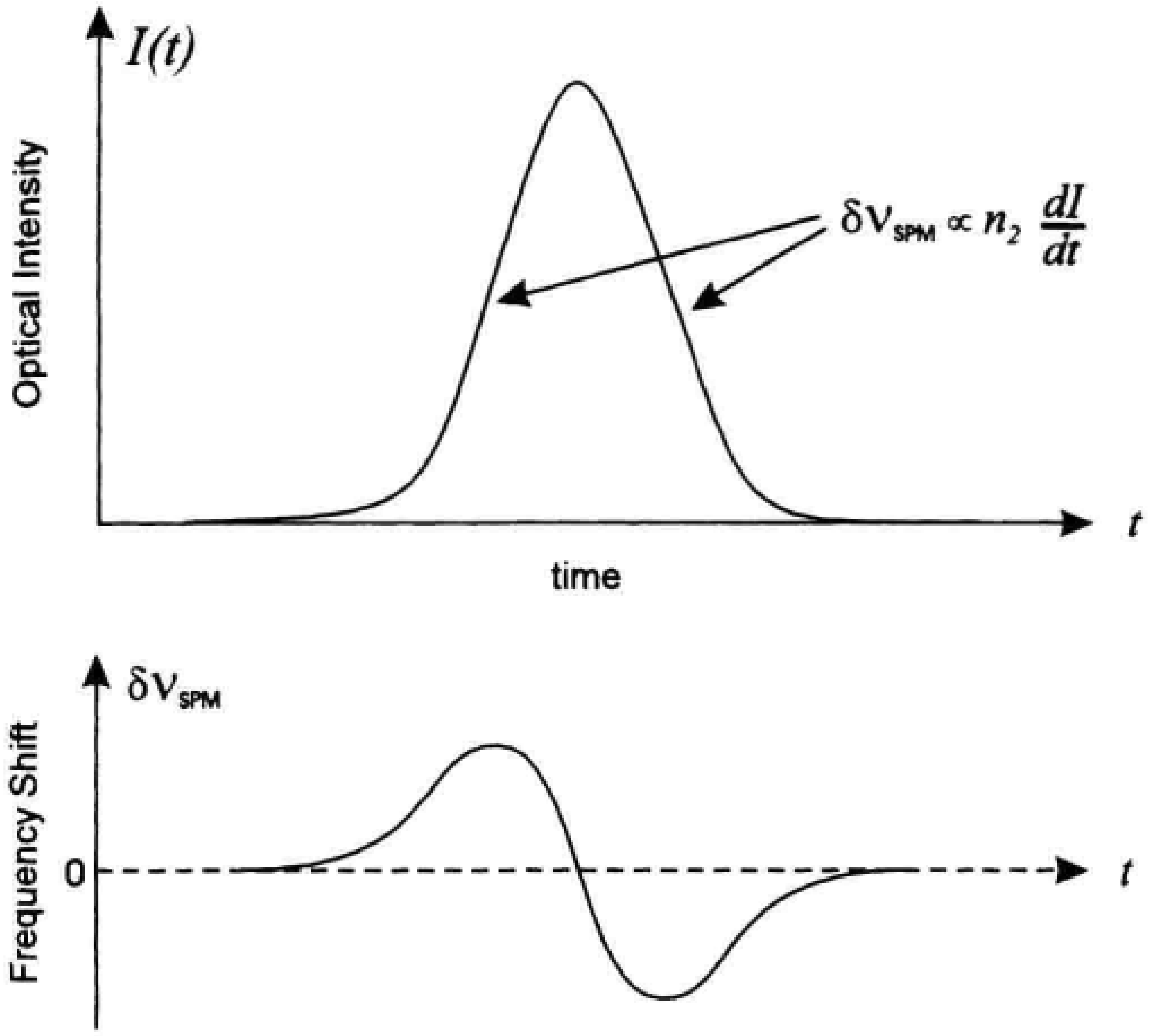

Figure B.2 Self-phase modulation (SPM) generates new frequencies where the intensity changes as a function of time.

lation causes the generation of new optical frequencies. These new frequencies are generated on the rising and falling edges of the pulse where there is a rate-of-change in the intensity. This concept is illustrated in Figure B.2. The bandwidth of the newly generated frequencies is proportional to the product of the nonlinear coefficient and the time derivative of the optical intensity.

The nonlinear Kerr effect plays an important role in the stable propagation of optical soliton pulses. Because of fiber dispersion, newly generated frequencies at the rising and falling edges of the pulse travel at different velocities such that they move towards the center position of the optical pulse. This effect leads to a stable packet of light which does not disperse as it travels along the dispersive fiber.

Just as for the Raman case, we can obtain a power-length product for self-phase modulation. The critical power is the power that causes the optical spectrum of the pulse to double in width due to nonlinear frequency generation.[2] To obtain this relationship, we assume a transform-limited input pulse (in other words, the condition where the product between temporal width and spectral width is a minimum). This power-length product can be approximated as

$$P_{cr}L_{\text{eff}} \cong \frac{\lambda A_{\text{eff}}}{\pi n_2} \sim 1.5\ \text{W} \cdot \text{km} \tag{B.4}$$

where P_{cr} is the critical peak pulse power, L_{eff} is the effective fiber length, λ is the optical wavelength, A_{eff} is the effective mode area, and n_2 is the nonlinear Kerr coefficient. The value of 1.5 W · km is representative of standard telecommunications fiber and is obtained using the values $\lambda = 1.55\ \mu\text{m}$, $A_{\text{eff}} = 70\ \mu\text{m}^2$, and $n_2 = 2.3 \times 10^{-20}\ \text{m}^2/\text{W}$.

The effective length can be limited by either fiber dispersion or fiber attenuation. For example, when short pulses are used, the effective length becomes equal to the dispersion length.[1] After the dispersion length the pulse width starts to spread causing the peak pulse power to decrease. For the case of wider pulses and a long fiber, fiber attenuation limits the effective length as described by Equation B.2. The critical power set by the Kerr effect can be important in coherent measurement techniques where the coherence properties are lost as the probe power is transferred into newly generated frequencies.

In long-haul communication links, self-phase modulation can limit maximum pulsed data rates. This occurs when high input powers are used and the resulting spectral broadening causes excessive pulse spreading due to the fiber dispersion. A related effect, called cross-phase modulation, can cause distortion in phase or frequency modulated communication schemes. This occurs when multiple signals are multiplexed along a single fiber and the intensity changes in one signal cause phase or frequency modulation (in other words, cross-talk) in another signal.

B.3 BRILLOUIN LIMIT

When a narrow-linewidth, high-power signal is guided along an optical fiber it can start to generate an acoustic wave which travels in the same direction as the input optical signal. This acoustic wave has a wavelength equal to approximately one-half the optical wavelength and travels at the acoustic velocity within the fiber. A simplified way to understand the nonlinear Brillouin effect is to think of the acoustic wave as a moving Bragg grating which reflects the input light into the backwards direction. Since the grating is moving in the forward direction, the reflected light is Doppler-shifted to a slightly lower optical frequency. This effect is illustrated in Figure B.3. For a silica fiber at 1.55 μm, the Brillouin frequency shift is about 11 GHz and is determined by the acoustic velocity in the fiber. The linewidth of the reflected signal depends on the losses for the acoustic wave and can range from tens to hundreds of megahertz in standard silica fiber.

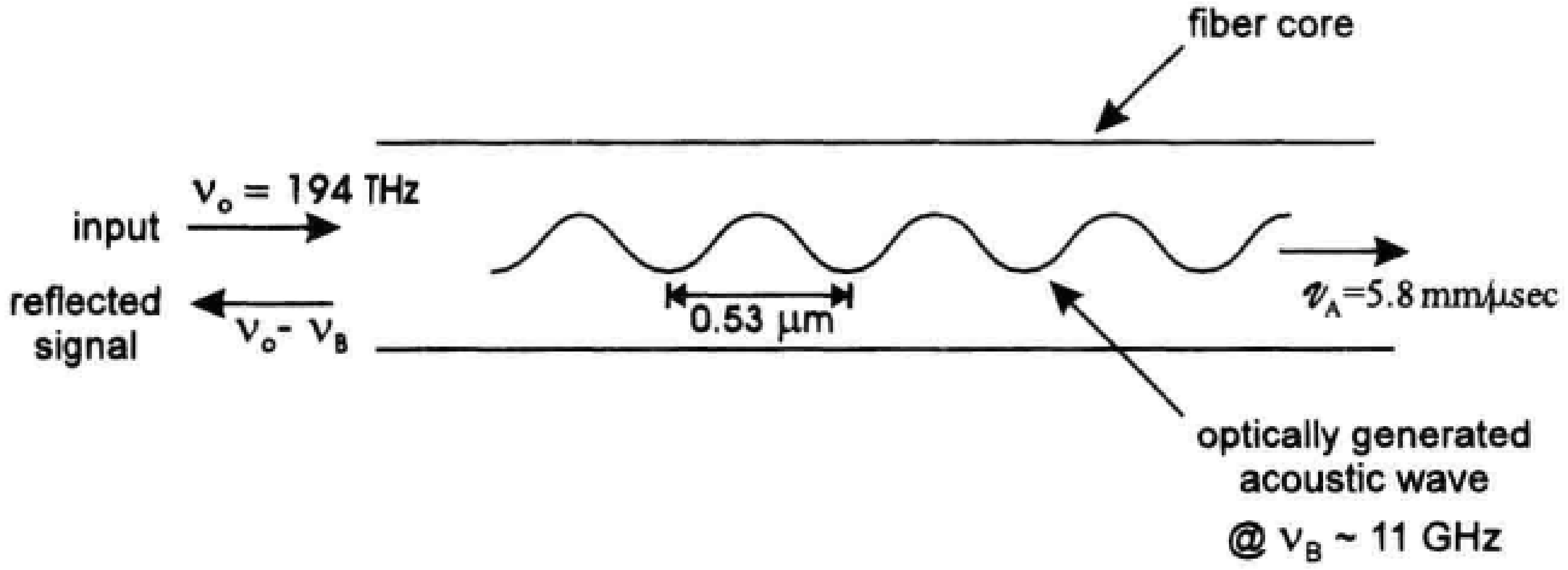

Figure B.3 Brillouin scattering occurs due to an optically generated acoustic wave that acts as a traveling Bragg grating.

As in the cases for Raman scattering and self-phase modulation, we can think of a maximum allowable power set by a power-length product. This power-length product can be written as[1]

$$P_{cr}L_{\text{eff}} \cong 21\left(1 + \frac{\Delta\nu}{\Delta\nu_B}\right)\frac{A_{\text{eff}}}{g_B} \sim 0.029\ \text{W}\cdot\text{km} \tag{B.5}$$

where $\Delta\nu_B$ is the Brillouin linewidth (typically in the range of 10 to 100 MHz), $\Delta\nu$ is the spectral width of the optical input signal and g_B is the peak Brillouin gain coefficient. The value of 29 mW · km is representative of standard telecommunications fiber at 1.55 μm and was obtained using the values $g_B = 5 \times 10^{-11}$ m/W and $A_{\text{eff}} = 70$ μm.[2] This low threshold value assumes a cw input signal with a narrow spectral width ($\Delta\nu < 1$ MHz). When using narrow linewidth laser sources, the critical power caused by Brillouin scattering can be orders of magnitude smaller than Raman scattering or self-phase modulation. For a fiber with a maximum effective length of about 20 km (attenuation of 0.2 dB/km), the critical input power for Brillouin scattering is only 1 or 2 mW.

For pulsed signals, the effective length must be handled differently than for the cases of Raman or self-phase modulation. For Brillouin scattering, the effective length is equal to one-half the pulse-length. This difference occurs since the Brillouin generated optical signal travels in the backwards direction and only interacts with the forward going signal for a limited distance. This effect is very important in long-haul coherent optical time-domain reflectometry measurements. In these measurements, a narrow-linewidth signal ($\Delta\nu < 1$ MHz) is used to probe a long fiber. Based on Equation B.5, the maximum input power would only be 1 or 2 mW. But since the probe signal is pulsed, input powers can be increased by over an order of magnitude before Brillouin scattering starts to deplete the input signal.

B.4 SUMMARY

The following table summarizes the nonlinear effects discussed in the above three sections. Raman nonlinearities usually only need to be considered when very large powers are used. The effects of self-phase modulation can often go unnoticed when using direct

Table B.1 Nonlinearities for standard telecommunications fiber at 1.55 μm.

Nonlinear effect	Power-length product	Frequency shift	Spectral width	Signal type
Raman	~ 17 W · km	~ – 13 THz (~ + 100 nm)	~ 6 THz (~ 50 nm)	cw/pulsed
Self-phase modulation	~ 1.5 W · km	centered on pump	dependent on pulsewidth	pulsed only
Brillouin	~ 0.03 W · km	– 11 GHz (~ + 0.1 nm)	~ 50 MHz	cw/pulsed

detection since the input signal only experiences an increase in its optical spectral width. For narrow linewidth optical signals, Brillouin scattering will most likely be the limiting fiber nonlinearity.

REFERENCES

1. Agrawal, G.P. 1995. *Nonlinear fiber optics.* 2nd ed. San Diego, CA: Academic Press, Inc.
2. Miller, S.E. and A.G. Chynoweth. 1979. *Optical fiber telecommunications.* New York, NY: Academic Press, Inc.
3. da Silva, V.L., Y. Liu, A.J. Antos, G.E. Berkey, and M.A. Newhouse. 1996. *Nonlinear coefficient of optical fibers at 1550 nm.* Boulder, CO: Symposium on Optical Fiber Measurements, NIST pub. 905:61–65.

APPENDIX

C

Fiber Optic Connectors and Their Care

Val McOmber

C.1 BACKGROUND

In the early days of fiber optic development, companies were designing and attempting to field "the best" connector. While there were a few large diameter and plastic fibers in use, the important step of the standardization to a uniform 125 μm diameter glass fiber, for most fiber applications was made. With this standard diameter fiber, one singlemode and twomultimode core sizes (Figure C.1) settled into place. The singlemode core settled on 9 μm (which can sustain singlemode propagation for wavelengths longer than about 1200 nm). The multimode cable needs could not find one core size but settled on both 62.5 and 50 μm cores, with either step or graded-index core-to-cladding transitions. For the purposes of this discussions, the important point is the single, standard outside diameter of the glass. Now connector manufacturers could focus on the mechanical alignment task of holding the fiber and aligning it with another identical size fiber. To achieve this difficult task, there were many different connector types and styles of mechanical assembles designed. The purpose of each connector is to bring together and hold the two cores of the glass fiber ends. The merits of each are in the ability to hold the close tolerances necessary for a good connection, and in the repeatability of multiple connections. Designers from Japan, Europe, and the U.S. were all rushing to find a way to hold the submicron tolerances necessary, at an acceptable cost.

At this point, another standardization appeared. In the connector, the element that holds the fiber, and provides the alignment positioning, is the ferrule (see Figure C.2). The agreement was to make the ferrule's diameter 2.5 mm. After this, a number of connectors appeared on the market at about the same time, each with a major company or region of the world backing it. The first wave of "common" connectors would include the

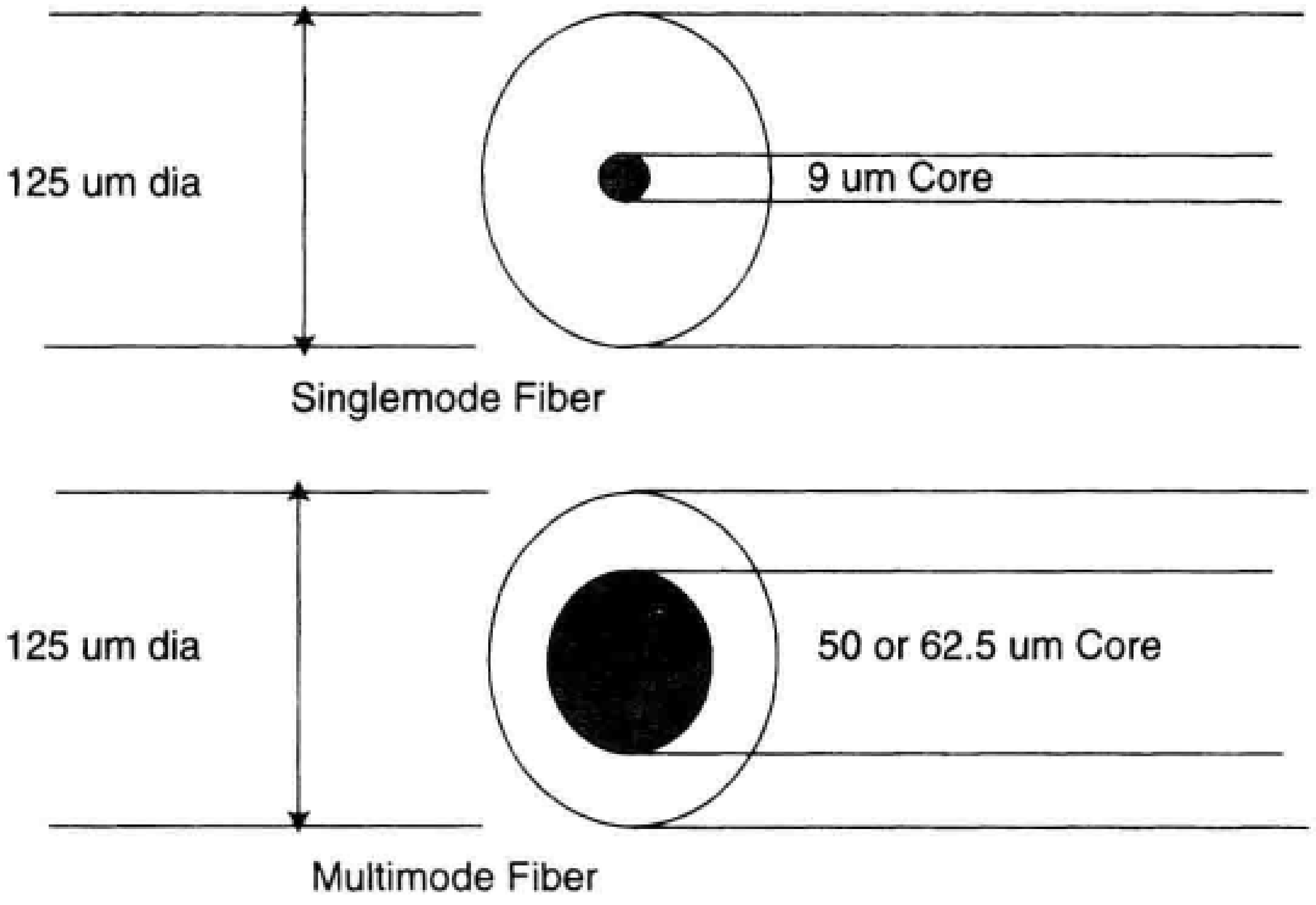

Figure C.1 Common fiber-optic cable has an outside diameter of 125 μm. The active part of the fiber is the core. Most fiber comes in singlemode (with a core of 9 or 10 μm) and multimode (with a core of either 50 or 62.5 μm).

FC, HMS-10, PC, D4, SMA, SC, DIN, ST, and Biconic. Some of these are shown in Figure C.3. Some connectors were designed for performance, while other connectors were designed for cost and volume as the key objective. Often, with these lower cost connectors, very few connections were expected, and after about ten connections the tight tolerances would degrade causing connector performance to degrade.

C.2 CONNECTOR STYLES

While it is acceptable for a particular link or system designer to choose one or another of these connectors (where the system designer could determine the tradeoffs of each connector), it is quite another problem for instrument designers to be able to choose a connector at the exclusion of all others. The instrument designer must either guess the most likely connector (and perhaps lose customers using other connectors), choose the highest-quality connector for the most repeatable measurements (and miss most of the customer base), or design some way to accommodate more than one connector style. The obvious choice required designing another, universal connector adapter, for all connectors. By nature, this connector must be designed for performance and ruggedness. The result of this effort from Hewlett-Packard, with some of the various adapters, is shown in Figure C.4.

After the connector designers learned how to hold connections in close alignment, their attention and efforts shifted to reducing reflections. An example of why reflections became the focus is shown in Figure C.5. This display shows how reflections effect the relative intensity noise (RIN) of a Fabry-Perot (FP) laser. This measure of a laser's noise

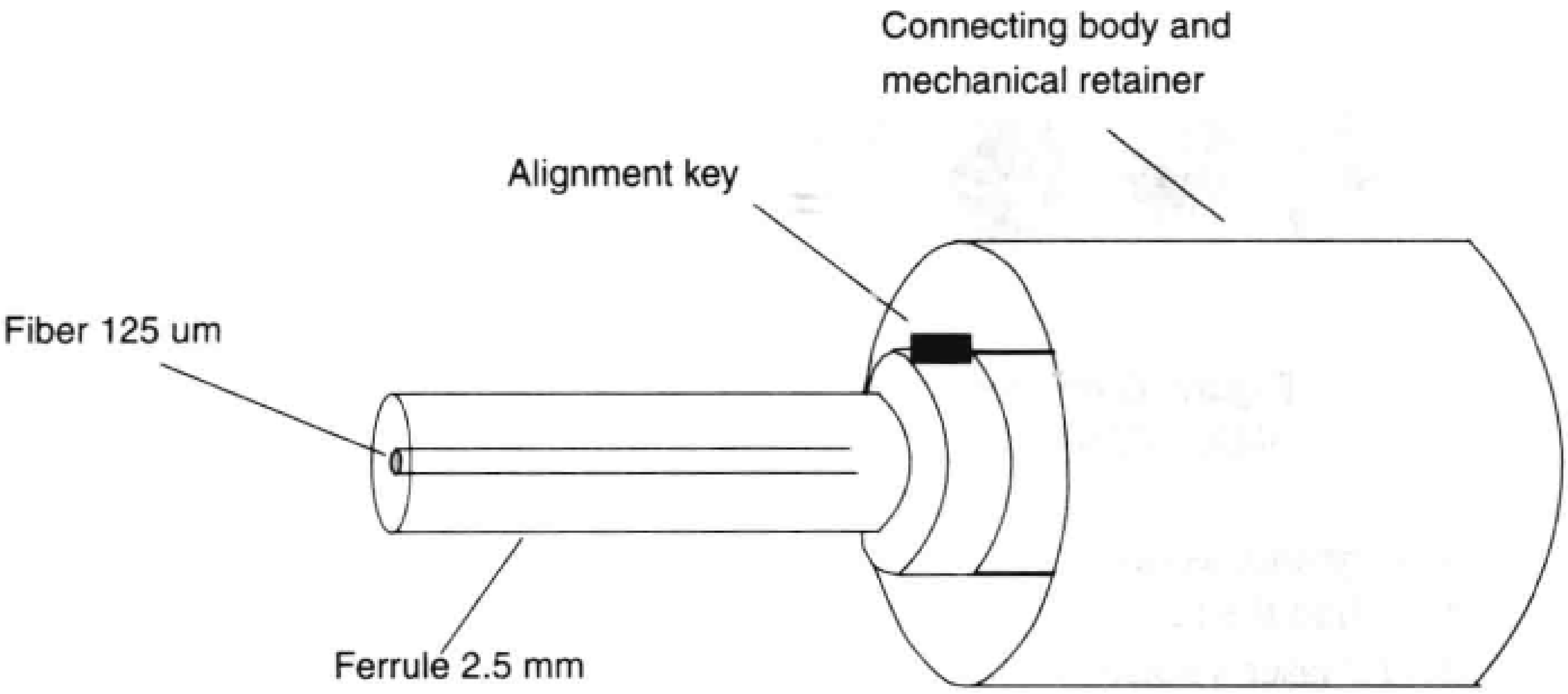

Figure C.2 At the end of a cable is the connector, which contains a mechanical assembly to hold the cable rigid and aligned, and the ferrule which is keyed. Inside, and concentric to the ferrule, is the glass fiber.

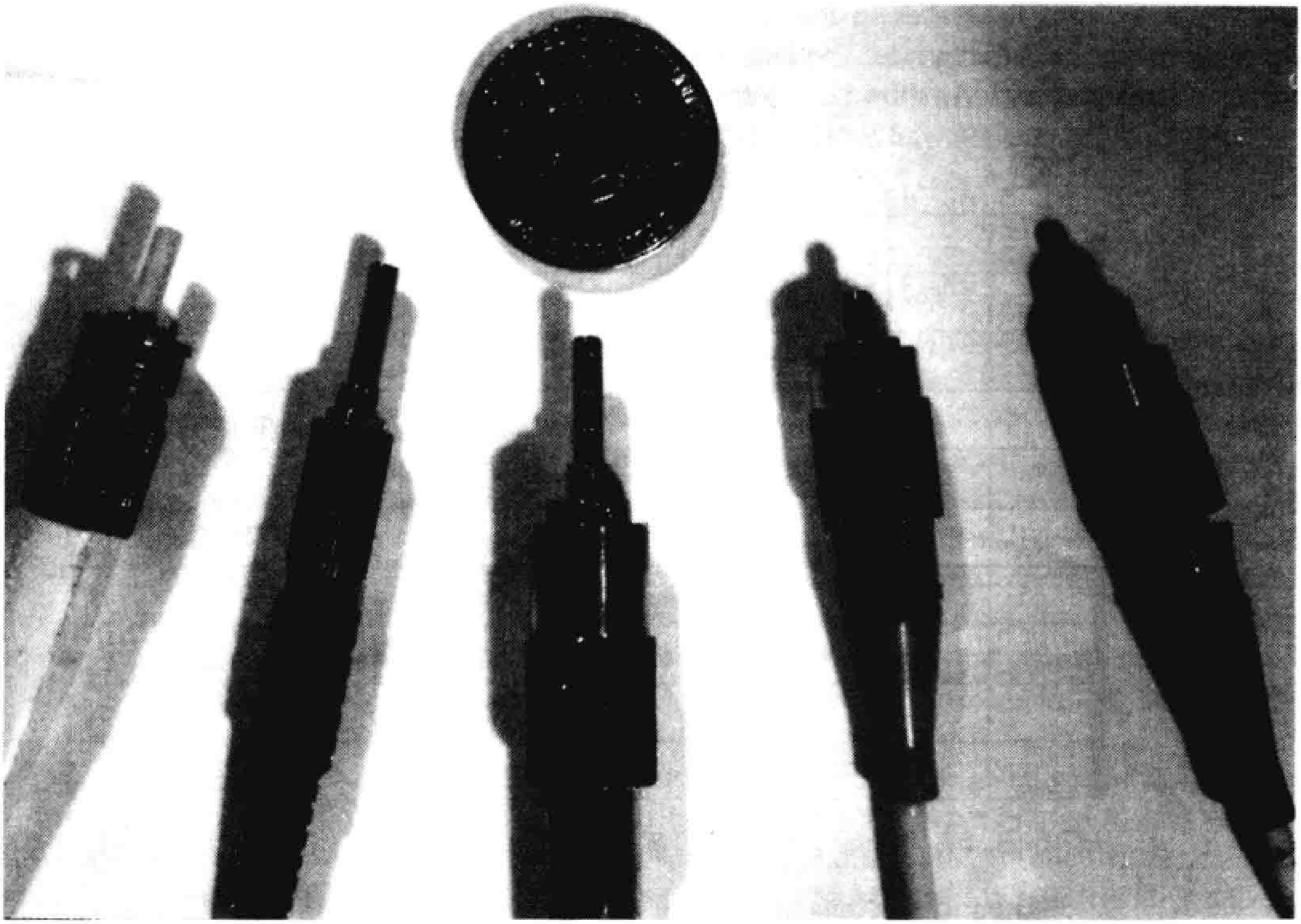

Figure C.3 Photos of five common fiber connectors: ST, DIN, HMS-10, PC, FC.

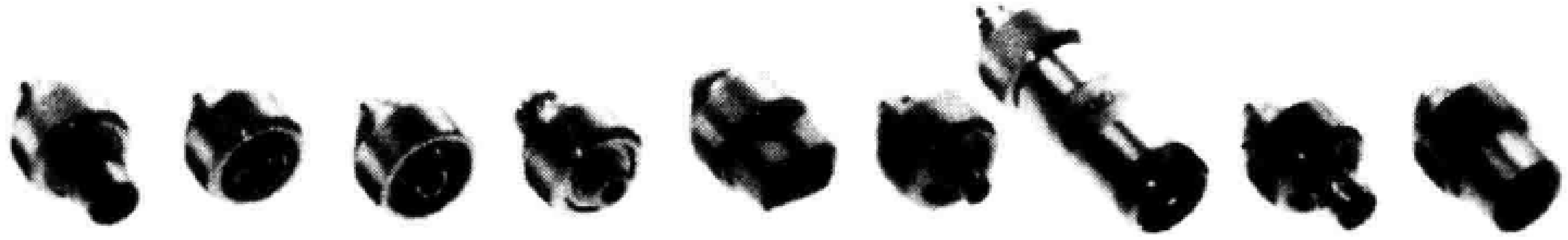

Figure C.4 Photo of HP connector adapters: HMS-10, FC/PC, D4, SMA, SC/SPC/APC, DIN, PC to angle adapter, ST, Biconic.

performance is one of the critical measurements for the laser source. Reflections getting back into the laser cavity can cause most lasers to be adversely affected. In this example, the FP laser's noise increased as much as 15 dB or more, due to an non-optimized connector. Distributed feedback (DFB) and other lasers can also become unstable with such reflections.

C.3 CONNECTOR DESIGN

A look at what makes up most connectors may be illustrative. The main component of the connector is the ferrule. The ferrule holds the glass fiber and is made from metallic or ceramic material. As shown in Figure C.2, most connectors have a common ferrule diameter

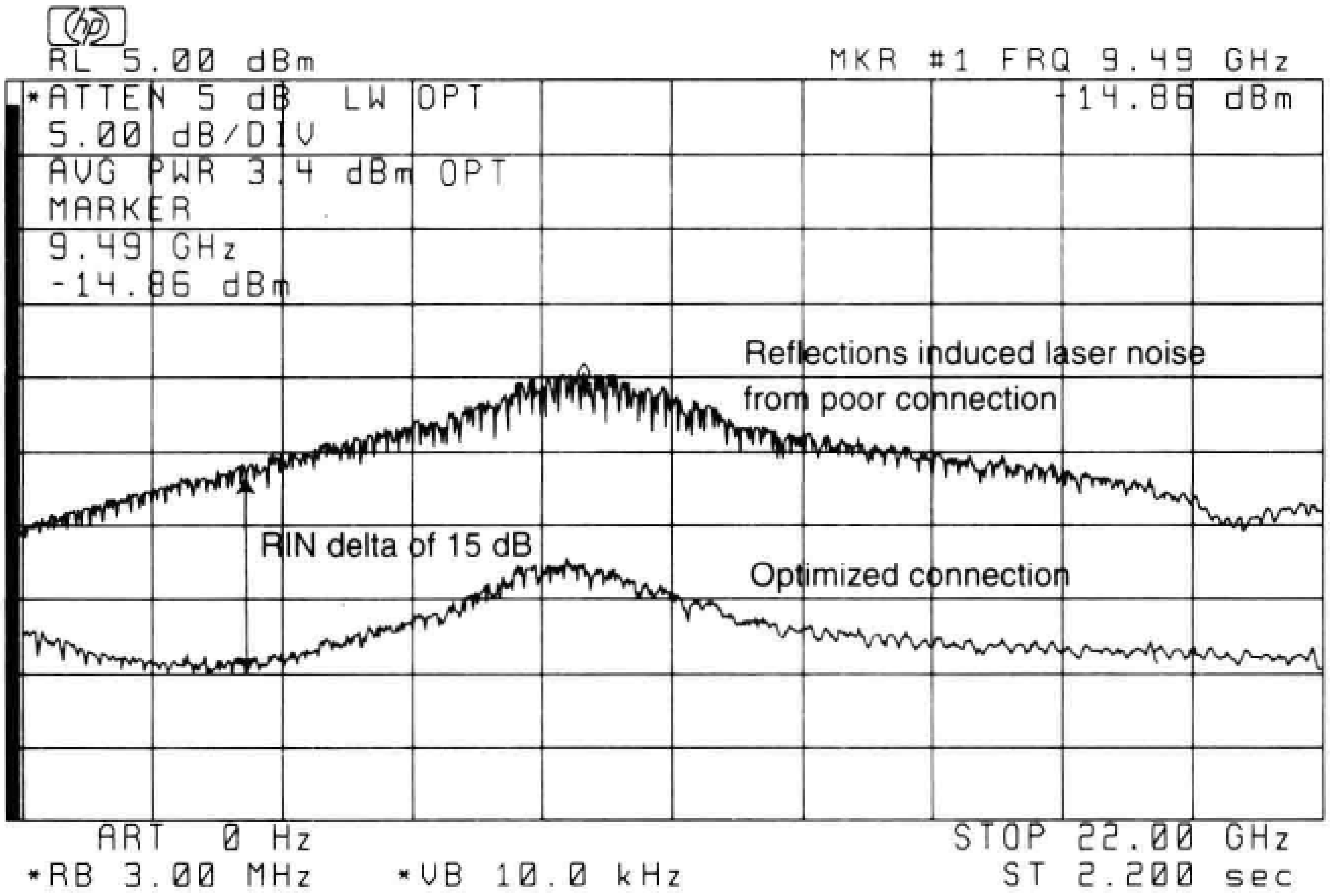

Figure C.5 Reflections from connections affect active components. This RIN measurement shows the effect of two connections, one with more reflections than the other, on a laser source.

of 2.5 mm. The 125 μm glass fiber is centered in the ferrule and exits at its endface where the holding material and fiber are together polished to achieve a smooth endface. Differences in connector types are mainly differences in the mechanical assembly that hold the ferrule in position against another, identical ferrule. The ferrule and the mating sleeve hold the fiber in alignment. The alignment key keeps the fiber from rotating, aids in concentric core matching, and keeps odd shaped cores (such as polarization maintaining fiber) and angled connectors in proper alignment.

Figure C.6 diagrams the major evolution in connector design. In the first (Figure C.6a) is a "fiber connection" or FC connector. These connectors were made with a flat endface. It is polished in such a way that the glass ends up concave and slightly recessed from an otherwise flat face. With this recessed glass there is no glass-to-glass connection. The resulting small gap causes an air-to-glass interface and relatively high reflections (14 dB return loss is the result of a glass-to-air boundary).

The PC, or physical contact connector (Figure C.6b) is polished such that the whole endface, including the glass-fiber tip, ends up with a slight convex shape. This slight rounding (using a radius of about 25 mm) brings the fiber up as the highest point on the endface ensuring a glass-to-glass connection. As long as the fiber and ferrule are kept at the same surface (and clean) the glass-to-glass connection removes the air-gap induced reflections and the return loss is improved from 14 dB to 30 or 35 dB. The FC/PC, ST, SC, APC, and DIN are all physically contacting connectors using the same 2.5 mm diameter ferrule and ferrule construction style. The differences between these connectors are in the mechanical holding assembly that holds the ferrule, the "connection" of the connector. For example the ST is similar to an electrical BNC with a bayonet connection. The FC/PC and HMS-10 uses a threaded sleeve like an electrical SMA connector. The SC is a newer snap-in style.

As applications became more demanding of lower reflections, this PC contact was improved by better polishing. The shape did not change, but a smoother surface allows better glass contact and a return loss of from 45 to as much as 60 dB. Typical construction of this popular cable, called the "super-PC" is shown in Figure C.7. Generally the fiber is held inside a ceramic (Al_2O_3 or ZrO_2) ferrule which is (optionally) contained inside a stainless steel sleeve. Positional concentric accuracy is held to about a micron or less.

It becomes obvious that there is a real danger with these "super-PC" connectors. Any little lint or dust particle can interfere with the glass interface. It doesn't take much to invalidate the critical polish of the fiber end. Finger oil and lint can change a connector with great return loss to a poor one. Worse, the glass face is at the highest point of contact and is very susceptible to damage. Grinding in contaminants and grit can destroy a connector, breaking out pieces of the glass. A cable that is damaged can in turn destroy other connectors and ruin an instrument!

In the quest for improved return-loss performance, the design moved away from very low insertion loss to focus on reflection control. To achieve better return loss, angled fiber ends were introduced (Figure C.6c). With an angled endface, the light could have a large reflection at the surface, but the angle causes the reflected light to go into the cladding and dissipate before the reflected light gets back to the source. This newer connector has a strong future, but the problem of a lack of standardization remains. They come in both an air-gaped

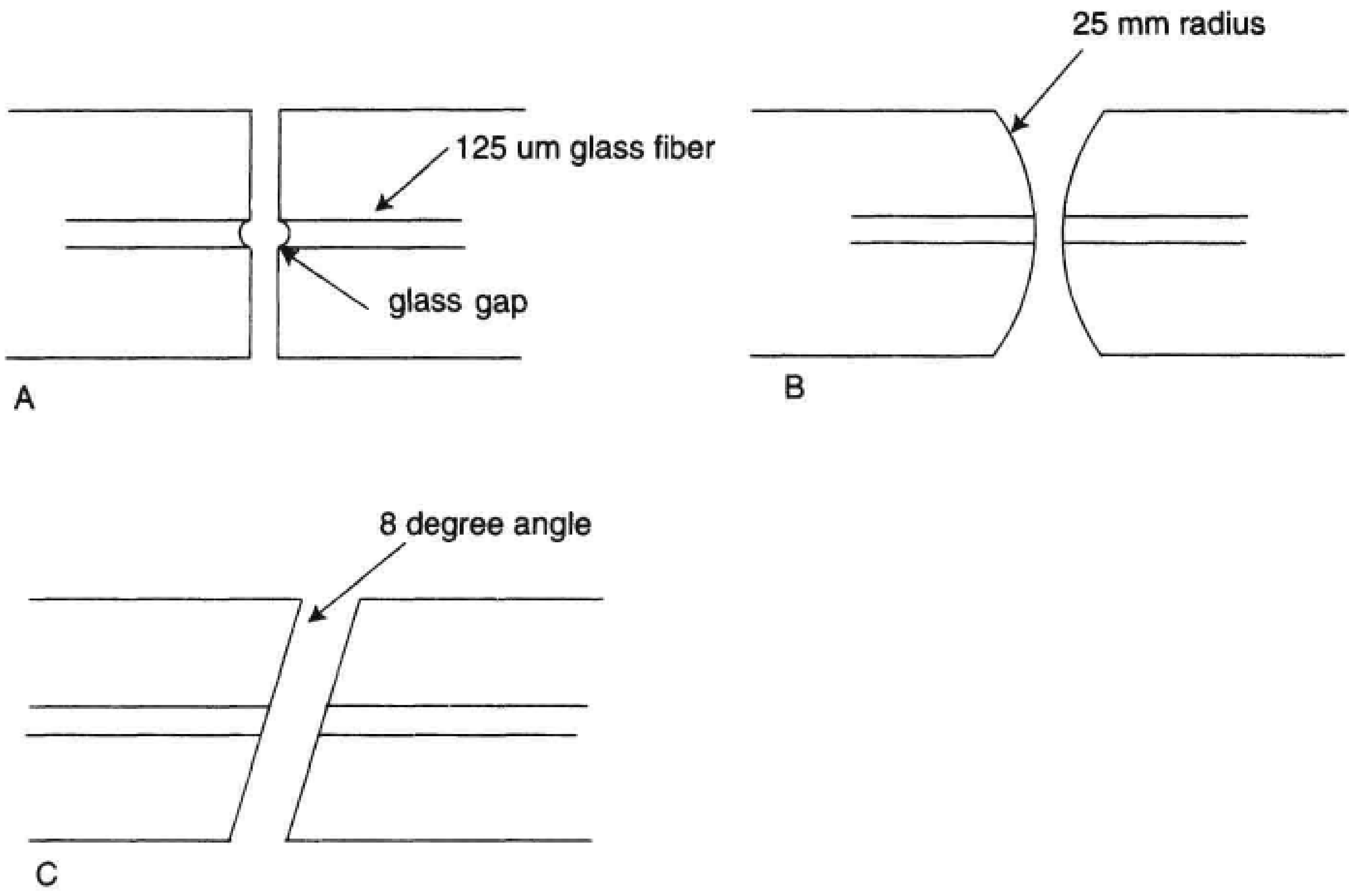

A = Fiber Connection (FC) B = Physical Contact (PC) C = Angled Fiber Connection (APC)

Figure C.6 Major developments of fiber-optic endfaces.

and physical contact form (lower loss), and each have different angled orientations possible. Also, while most connectors use an 8 degree angle, there are both "flat" angled and "non-flat" angled versions available (Figure C.8). Thus, trying to mate different angled connectors might not only be ineffective, but could damage the connector.

Given all these choices, the FC/PC style emerged as the most popular connector, capturing the vast majority of instrumentation applications. While not the highest performing connector, it seems to be a good compromise of performance, reliability, and cost. If cleaned well, the PC connector can withstand many insertions and meet most instrumentation needs.

Even with the popularity of the FC/PC, new design efforts are continuing. Just as this book is going to press, a new E2000 connector was announced. Like the SC, it is a push-in, pull-out assembly with the added feature of automatic covering caps for both the fiber and the receptacle. This cover will block dust, fingers, and laser light (eye protection). As Figure C.9 shows, in this new connector style, the design of the endface has also changed. Called a Pilzferrule, this connector has a raised core in the ferrule producing a mesa or button-top (*pilz* means mushroom in German) on the endface. This core uses an active centering operation (like the HMS10) for better fiber position control, better return loss, and lower insertion loss, all at a lower cost.

An example of the risk in choosing a new cable with a "better" connector comes from a service alert issued by Hewlett-Packard for their popular power meter. The

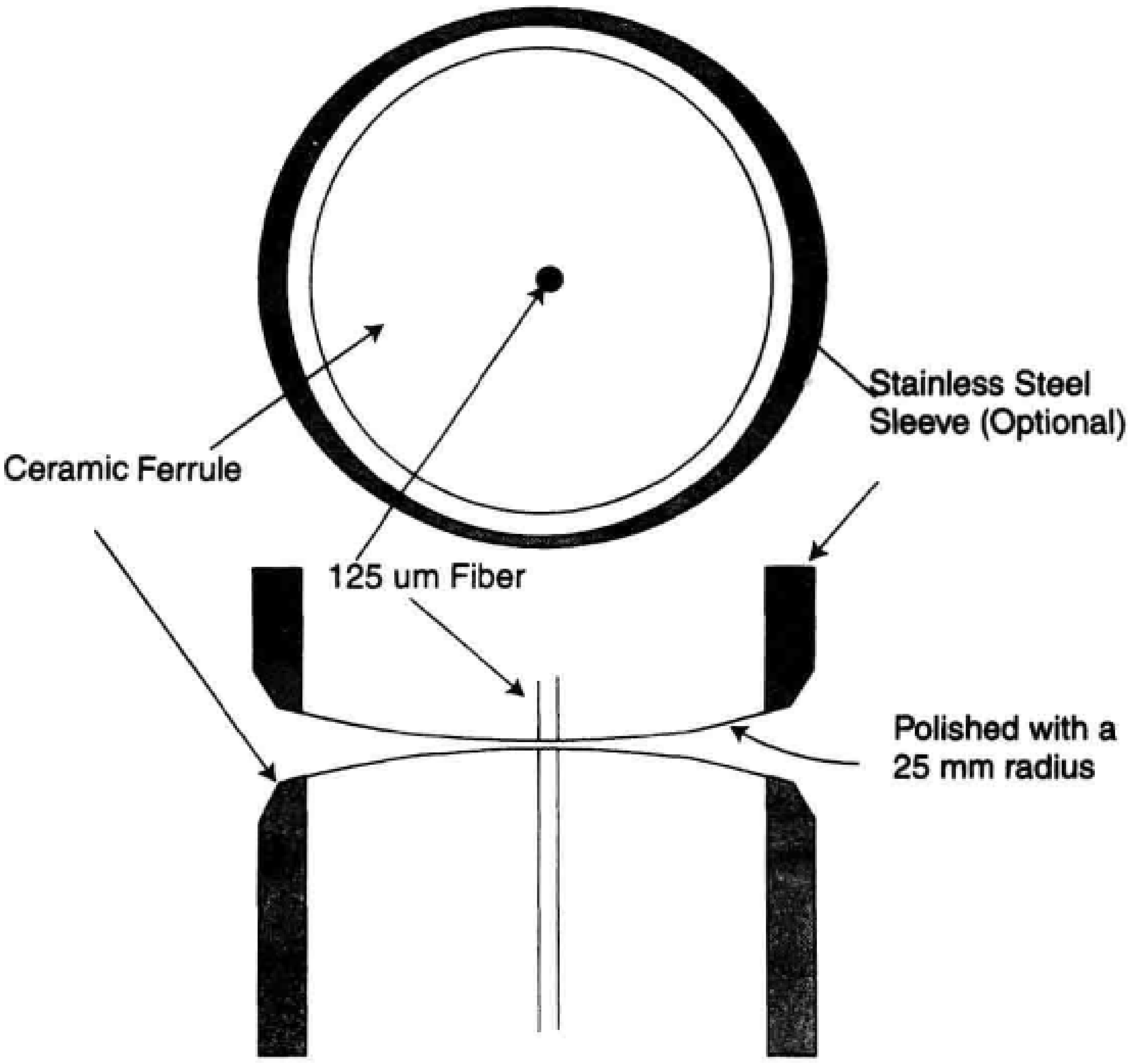

Figure C.7 Construction details of a standard PC connector.

HP 81532A power sensor module uses a special connector with a lens interface to position the fiber end preciously to achieve very accurate power measurements (Figure C.10) from either a PC or a flat-angled connector (the only kind available at its introduction). In this connector, there is a positioning sleeve to hold the end face at a known distance from the lens. However, as Figure C.11 shows, the "nonflat" angled fiber end hits the lens, before the stop ring, causing damage. Also, as in Figure C.12, another "nonstandard" angled fiber connector can cause a missed placement and loss of accuracy in the measurement. The alert also calls out the Pilzferrule-style cable. Similar to the "nonflat" angled case, this Pilzferrule's raised mesa, (Figure C.9), is too high. The mesa top hits the glass before the positioning sleeve stops it. While the Pilzferrule is a very good connector and can be used with many PC style connectors, the design change of this (and other) connectors is unsuited for the power sensor and is damage causing. Thus, while unfortunate, the user must be aware of what kind of connector and fiber to use with each instrument and system for best performance.

So, if reflections are a major concern, and an angled-fiber end cannot be used, what other options and insights are there? One of the causes of reflections is off-center fibers. Singlemode fiber, core is 9 μm. For typical predrilled ceramic-ferrule connectors, the centering, gluing, and other alignment processes used to place the fiber in the center of the end face can leave two fibers as much as a micron off center with each other. To offset

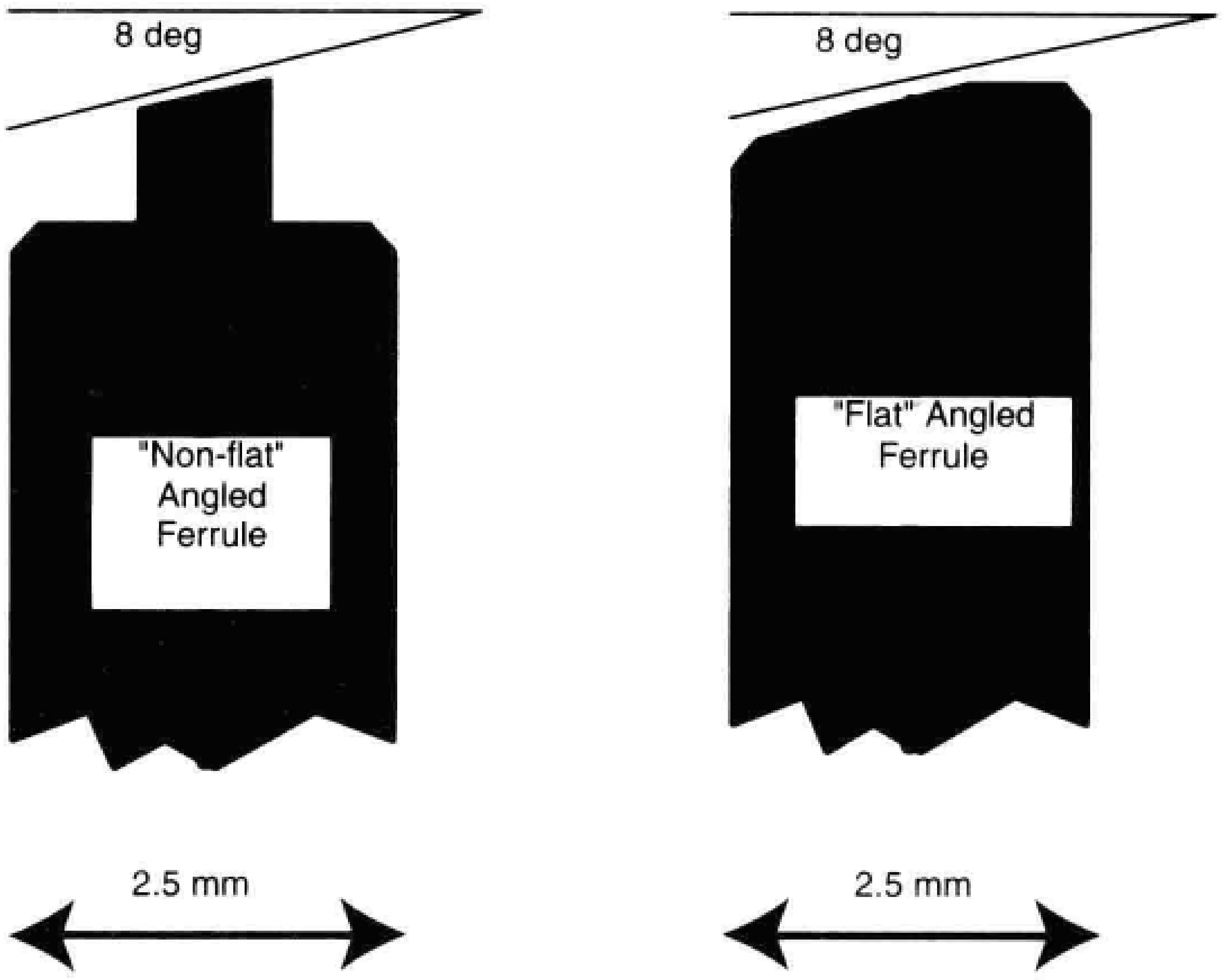

Figure C.8 Angled connectors come in both "flat" and "nonflat" angled ferrules.

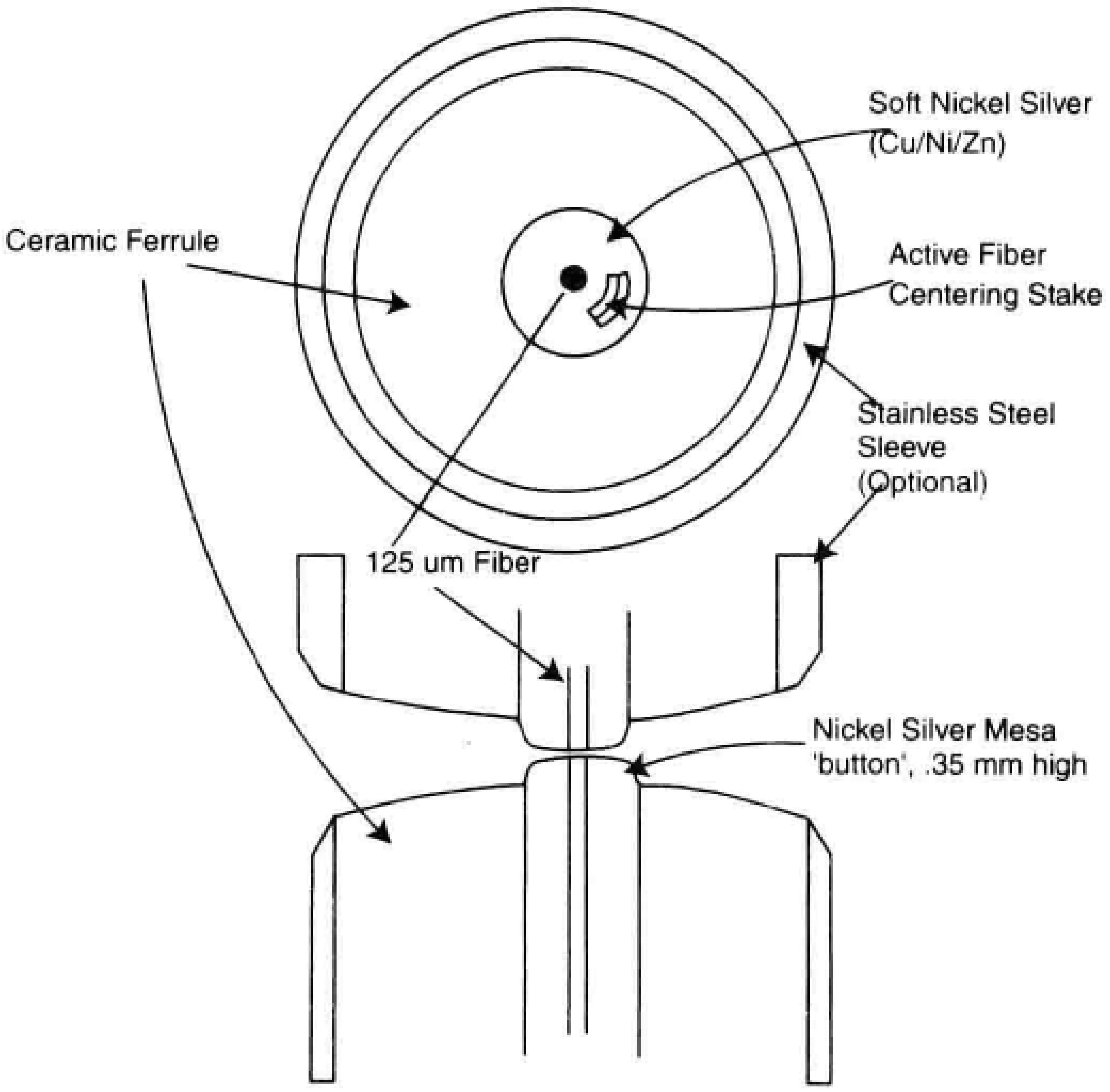

Figure C.9 Construction details of a PC Pilzferrule (mesa or button) connector.

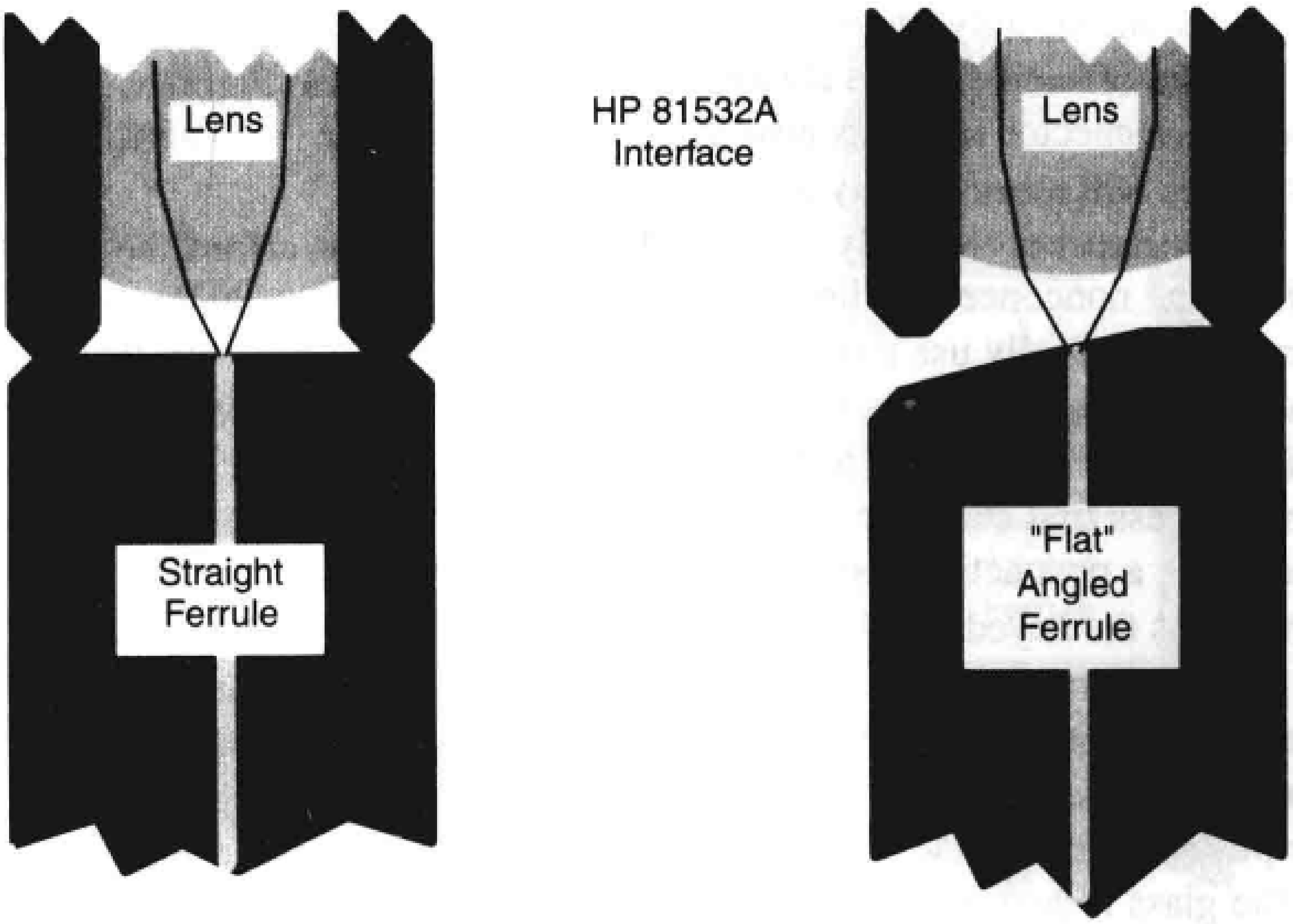

Figure C.10 The HP 81532A works with both straight and flat-angled connectors. The lens is protected and the correct distances are maintained.

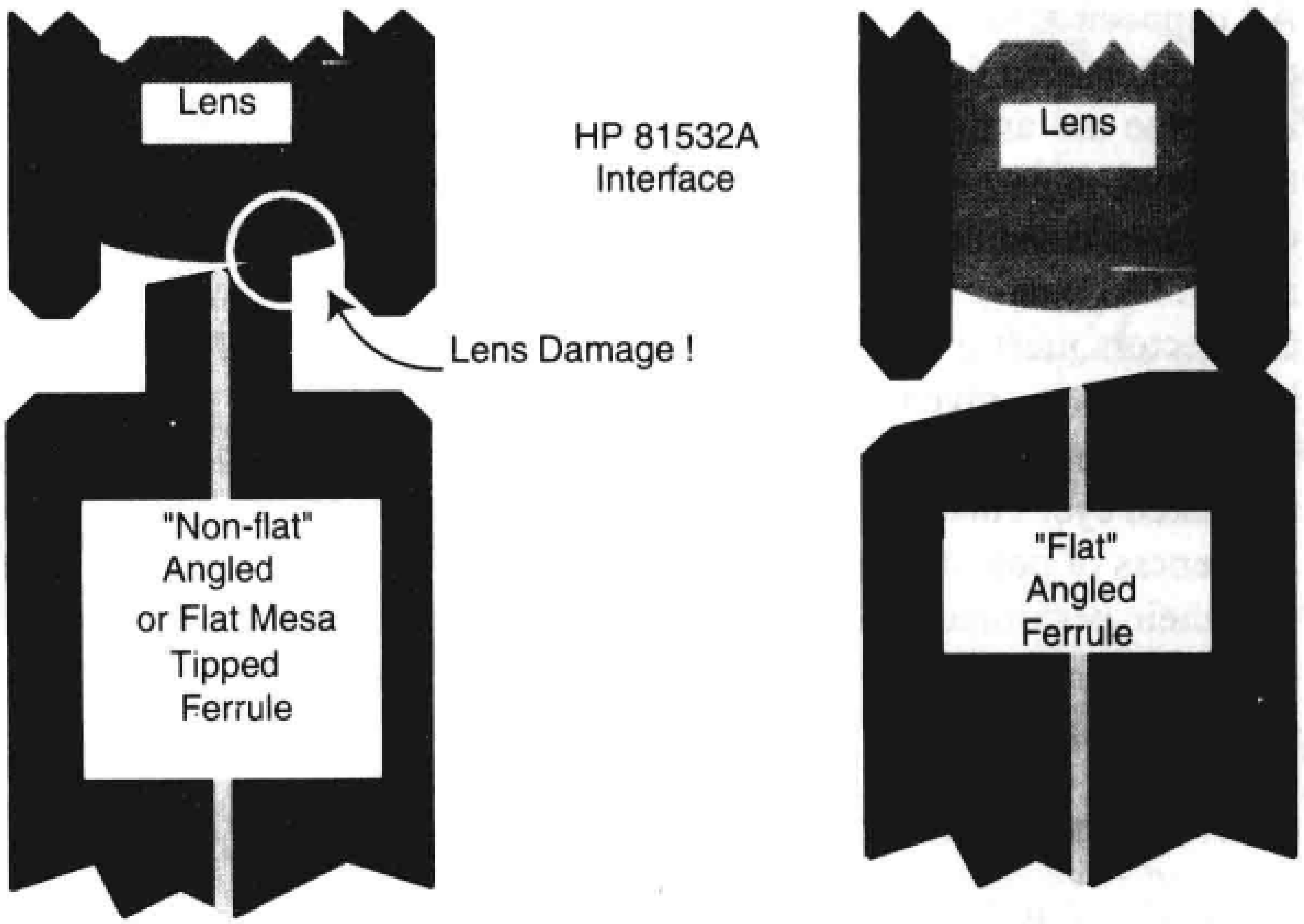

Figure C.11 There is a risk of damaging the lens with some connector styles.

this nonconcentricity, the ferrule is positioned, relative to the connector's alignment key, so that the off-axis fiber is always in the same sector; see Figure C.13. Thus, mating with another connector which is also off center, if that fiber is located in the same sector, the two cores will more closely align.

Instruments that rely on tight tolerances can not afford the "cheaper" connectors with large nonconcentricities. Looking for tighter matches, high-quality measurement instruments typically use a connector like the Diamond (HMS-10) that has concentric tolerances of a few tenths of a micron. Figure C.14 details the HMS-10 connector design. The Diamond process uses a soft nickel silver (Cu/Ni/Zn) inner ferrule that holds the fiber. The process first stakes the soft nickel silver to fix the fiber in a near center location, and then uses a post active staking to shift the fiber into the desired position, within 0.2 μm. This, plus the keyed axis location makes for very good alignments.

The drawback to this connector is the soft endface. Care must be given to keep the endface from excessive scratching and wear. Small wear to the soft material is not a problem if the glass face is not impacted, but, damage can easily occur. The soft material can be pushed with a piece of grit, moving the fiber position, or changing the mating surface. If the glass is scratched, then all of the careful polishing is lost and reflections and insertion loss will soar. Yet, with proper care and cleaning they can last. Some of these HMS-10 soft-center connectors have been in service for years, with many connections per day, maintaining a very good return loss (high glass-surface quality).

C.4 CONNECTOR CARE

All connectors must be viewed like a high quality lens of a good camera, a stray fingerprint can cause a lot of grief. The weak link in many systems, and in instrument reliability, is the use and care of the connector. Because current connectors are so easy to use, there tends to be reduced vigilance in connector care and cleaning. It only takes *one* time of a missed cleaning for a piece of grit to permanently damage the glass and ruin the connector. Too many times an instrument must be serviced to replace damaged connectors. Connectors must be replaced, and thousands of dollars and lost time could be avoided if better care were given to the fiber optic connector.

Fiber optic connectors are susceptible to damage that is not immediately obvious to the naked eye. This damage can have significant effects on measurements being made. An awareness of potential problems, in conjunction with good cleaning practices, can ensure that their performance is optimized. With glass-on-glass interfaces, it is clear that any degradation of a ferrule or fiber endface, any stray particles or finger oil on the endface, can have a significant effect on connector performance.[1]

C.4.1 Connector-Care Actions

The first step in reducing connector-induced effects is care in choosing a connector style. Some questions to ask are: Will the connector need to make multiple connections? What is the reflection tolerance? For example a DFB laser needs high isolation to remain stable

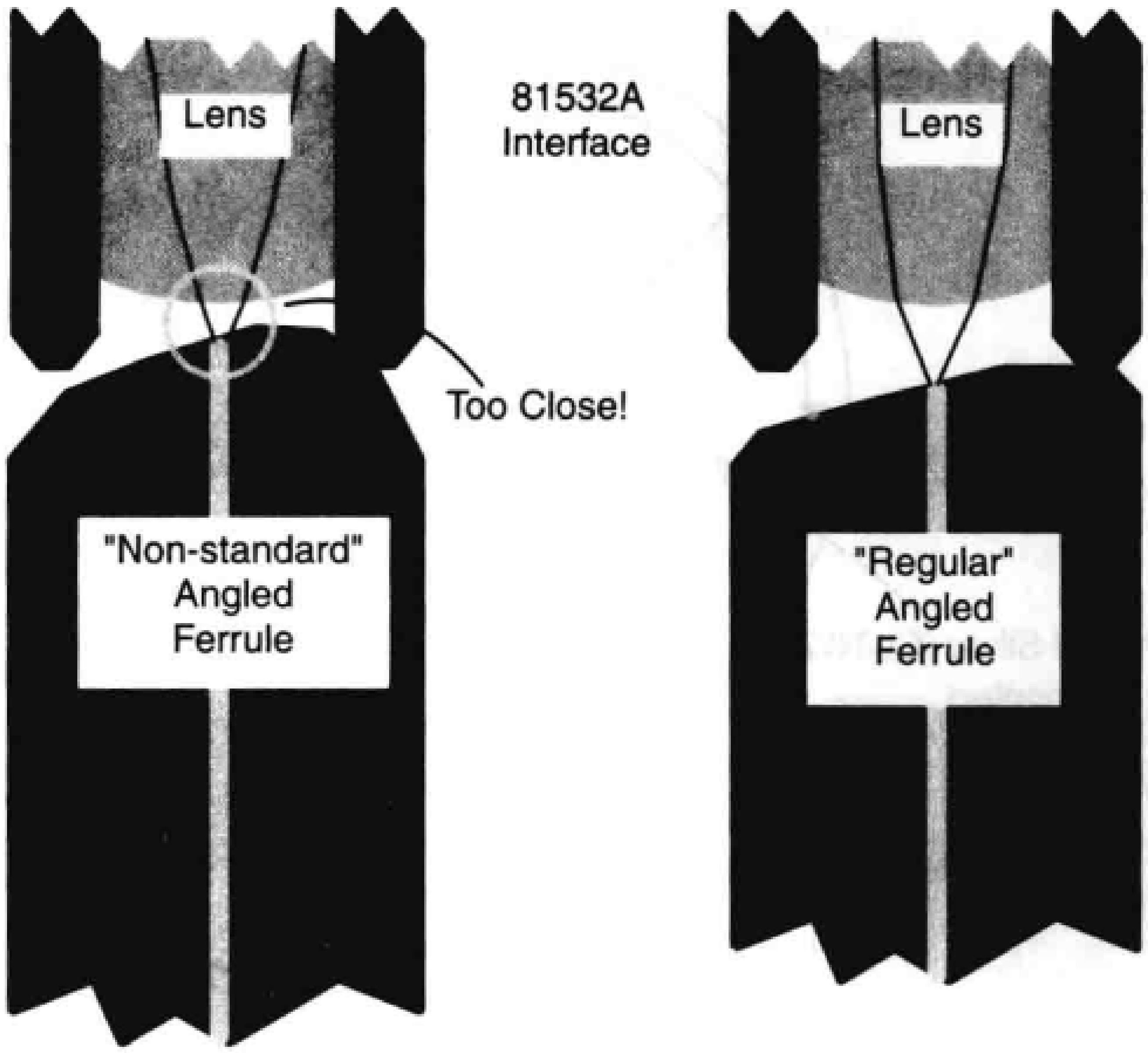

Figure C.12 There is a risk of measurement errors with some non-standard angled ferrules.

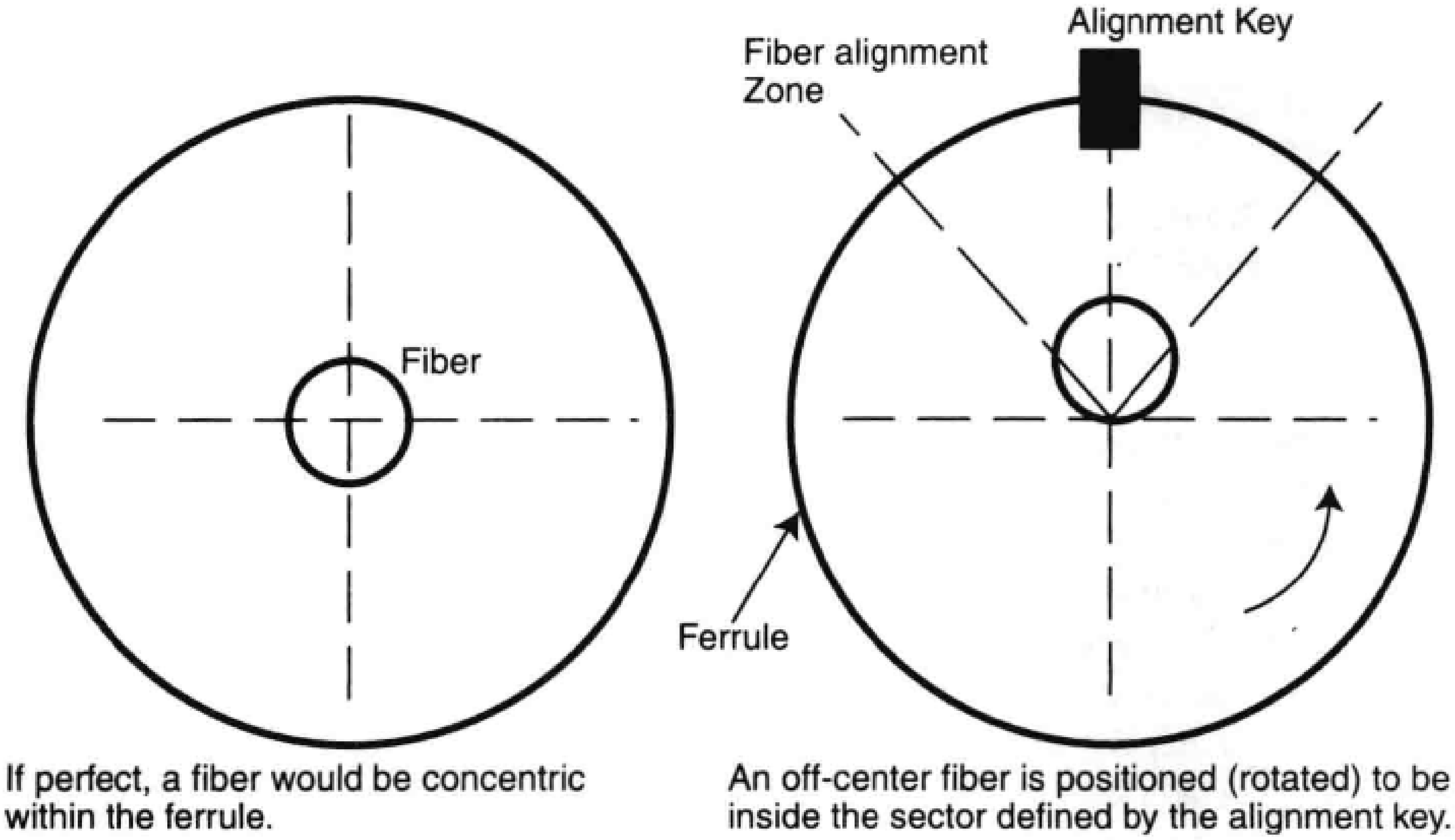

If perfect, a fiber would be concentric within the ferrule.

An off-center fiber is positioned (rotated) to be inside the sector defined by the alignment key.

Figure C.13 Close alignment and placement of the fiber for concentricity is important for low return loss. After cementing the fiber, the ferrule is rotated and keyed so that any nonconcentricity is maintained within a narrow sector for best mating.

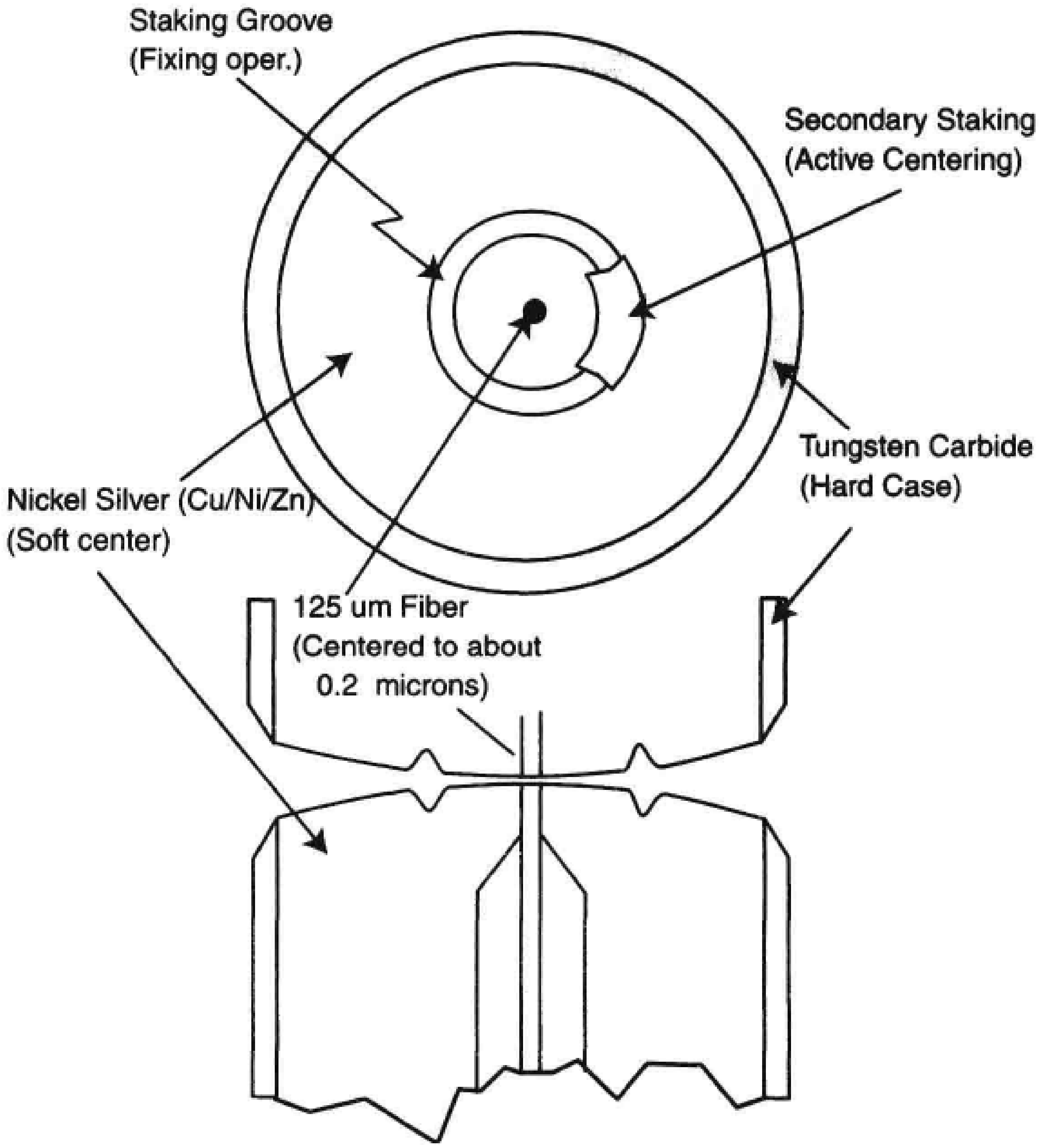

Figure C.14 Construction details of an instrument grade (Diamond HMS-10).

and low noise, often more than 60 dB isolation, and in some applications as much as 90 dB or more isolation, is needed. Will a connector reduce the return loss too much? Will a fusion splice be required? If a connector is used, how many connections will be made over it's lifetime? Will an instrument grade connector (precision core alignment) be required? Is repeatability tolerance (of reflection and loss) of connections important? Do your specifications take these into account?

After the connector is chosen, the next step is the connector's maintenance. Figure C.15 is a close-up of a clean PC cable endface. In contrast, Figure C.16 shows a connector end that was used with a cable end that avoided the alignment key (perhaps a temporary ferrule without a key, or possibly a mismatched long ferrule put into a short connector assemble). Material is smeared and ground into the endface causing light scattering and poor reflection. And, as Figure C.17 shows, if continued, this action will grind off the glass face and destroy the connector.

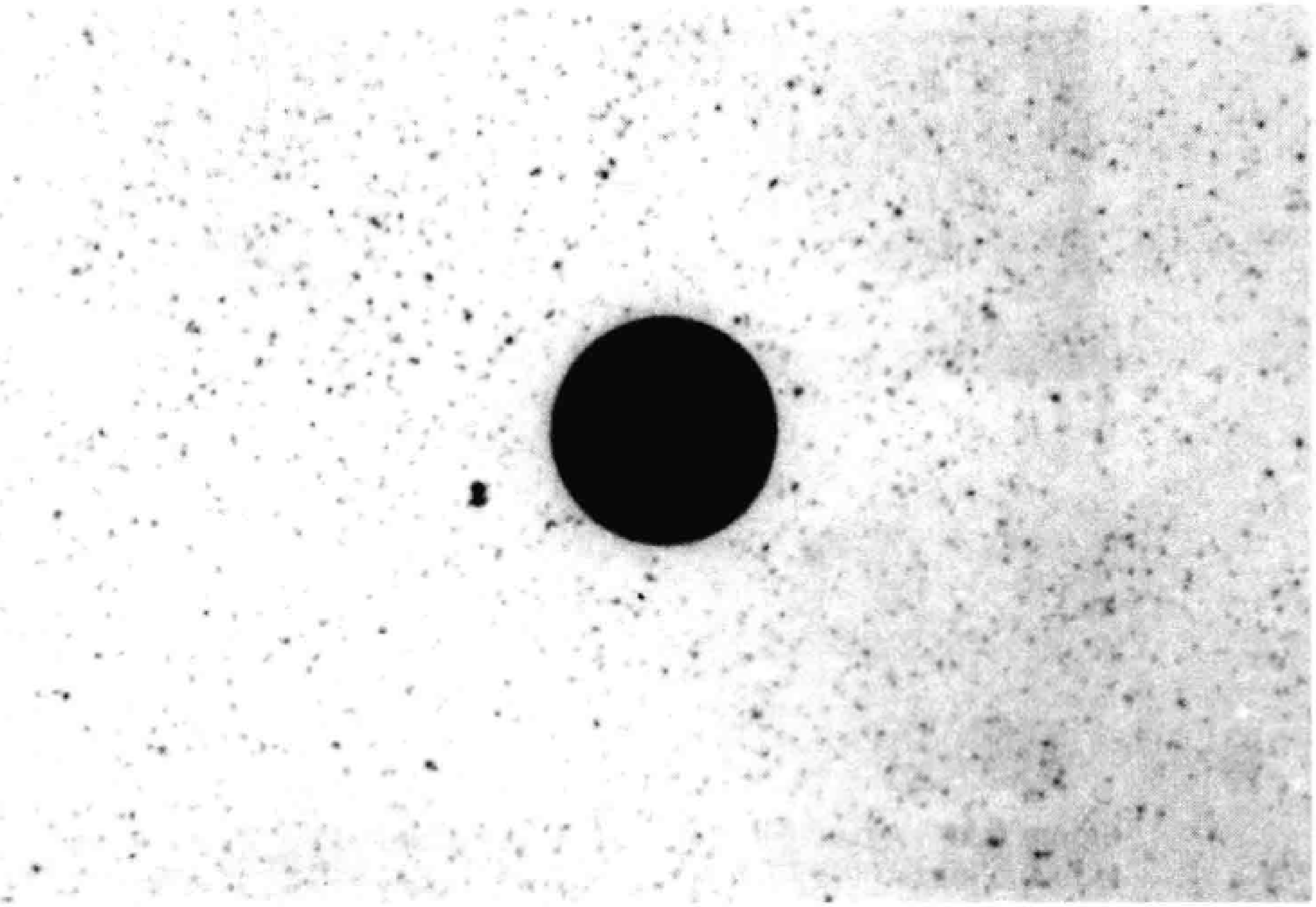

Figure C.15 A photo of a clean and problem-free connector.

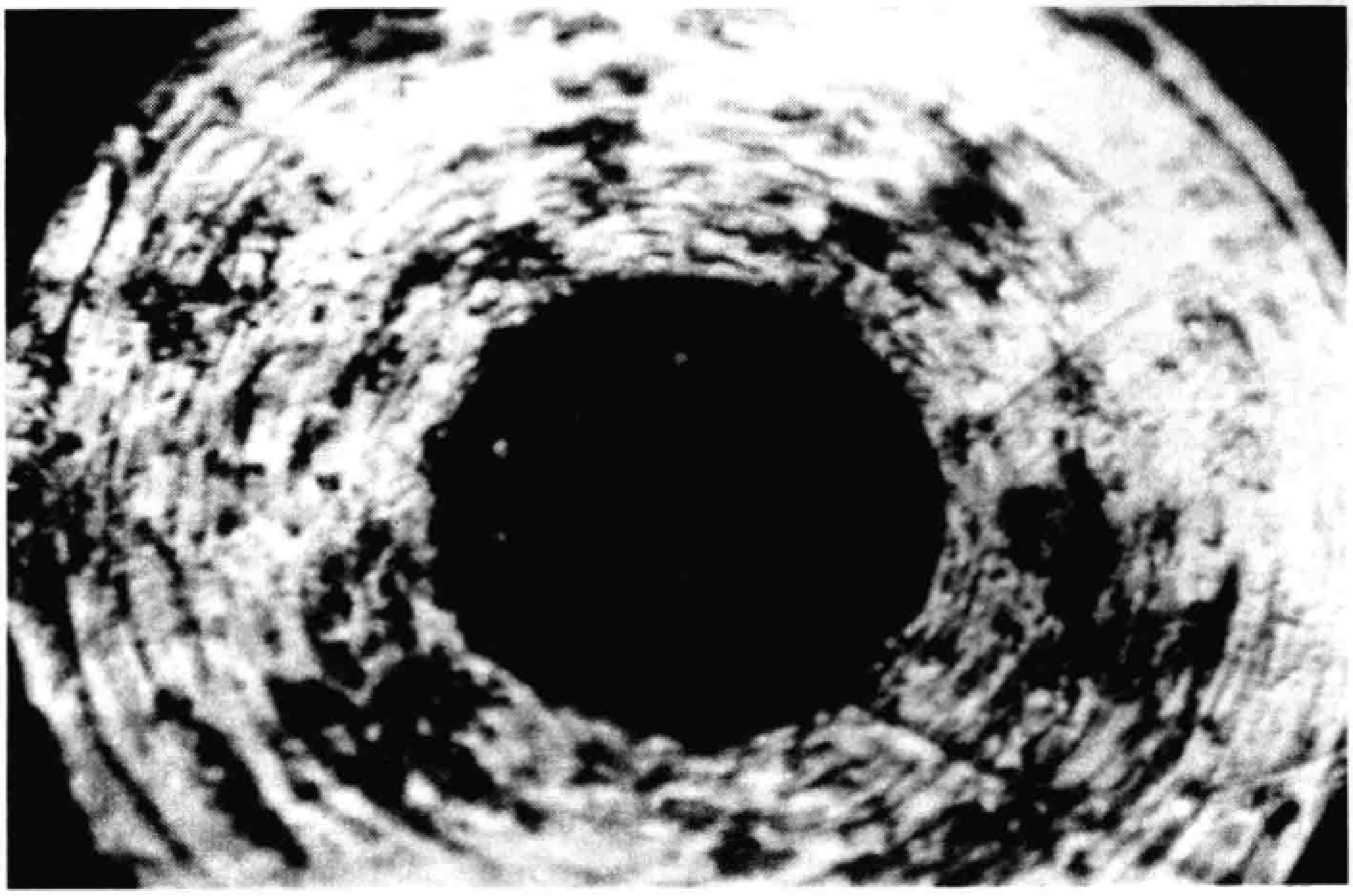

Figure C.16 A photo of a dirty endface from poor cleaning.

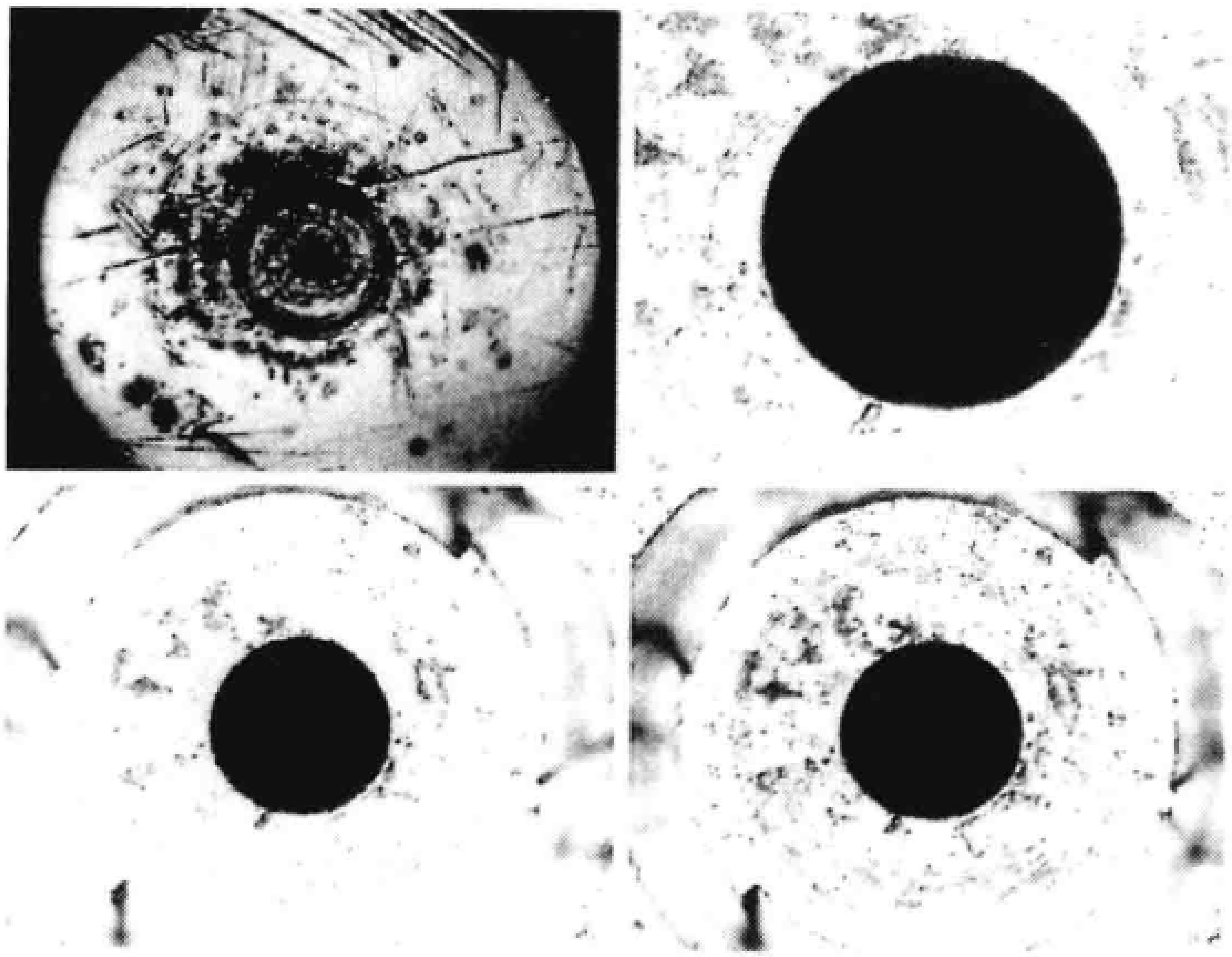

Figure C.17 A damaged connector from abuse and using an unkeyed ferrule to mate with this cable. The top left image is 50×. The black center is the glass fiber and the ring around it is the centering "stake." The bottom two are at 200× and the top right is the glass fiber end at 400× showing the ringed damage on the glass.

Repeated connections without removing the participles, or using improper tools can lead to physical damage of the glass fiber endface as seen in Figures C.18 through 21. Where the damage is severe, the damage on one connector can be transferred to another good connector that comes in contact with it.

The cure is disciplined connector care. Soft swabs should be used—never use metal or sharp objects. Some connectors have a soft endface material that can be very easily scratched and damaged. In Figure C.18, for example, the results of using a pin on the connector surface are seen. In Figure C.19, a close-up of this damaged connector, not only is there gouging in the endface around the fiber, but the glass fiber itself has been chipped off and broken. Broken or damaged glass can lead to a number of problems that are often ascribed to other causes. This connector will probably damage any other fiber that is mated to it. In Figures C.20 and C.21, another connector is seen with severe abuse. In this example, the soft ferrule core was pushed away from the glass and there is pitting in the fiber end. In addition, the glass fiber is sticking up almost 3 μm above the uneven surface (from severe wear of the soft metal that was once flush with the glass fiber).

Another potential problem comes with matching gel and oils. While these often work well on first insertion, they are great dirt magnets. Damage is often caused as the oil or gel grabs and holds grit that is then ground into the fiber endface. Also, some early gels

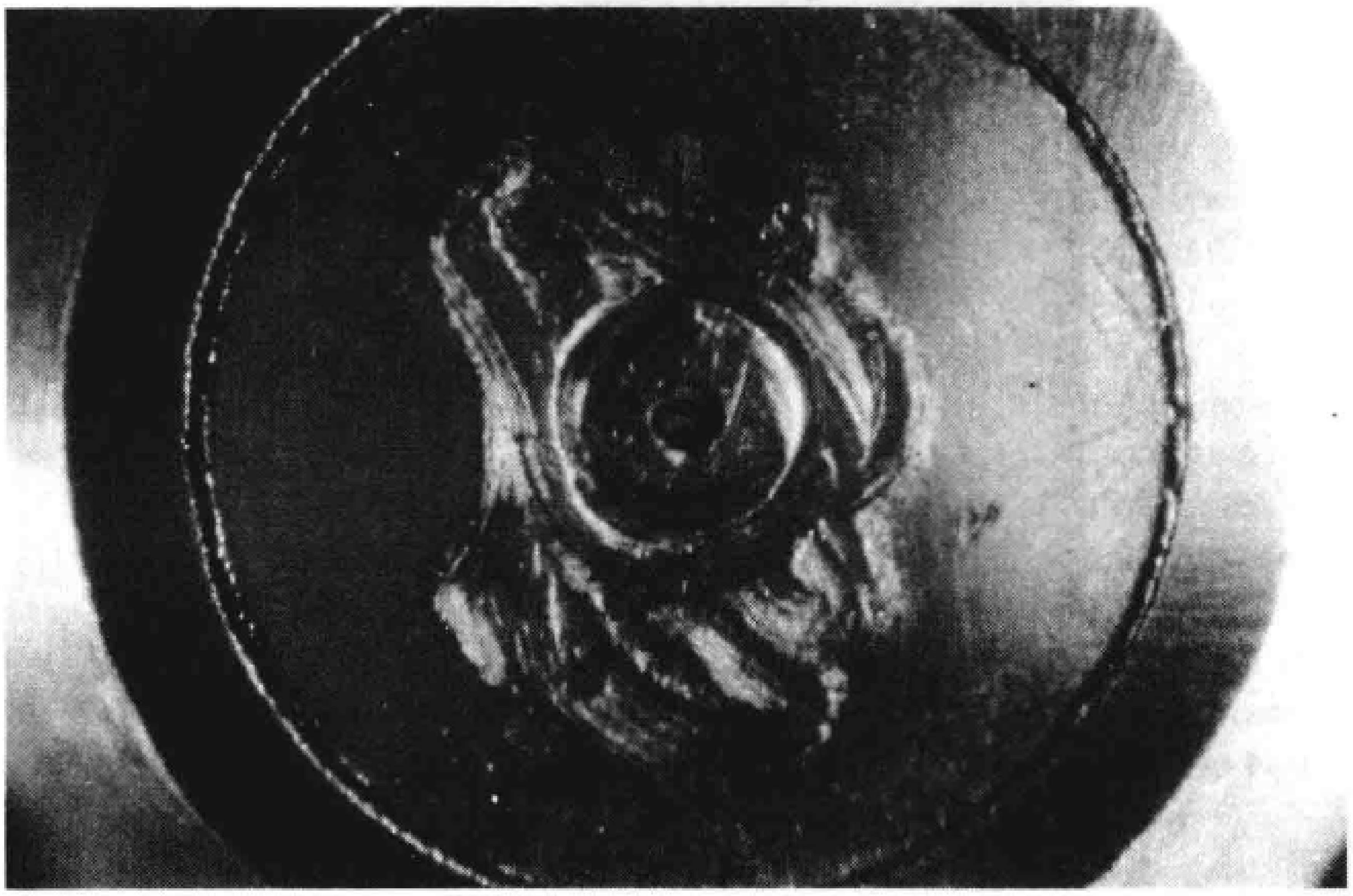

Figure C.18 A damaged fiber end from using a pin on it.

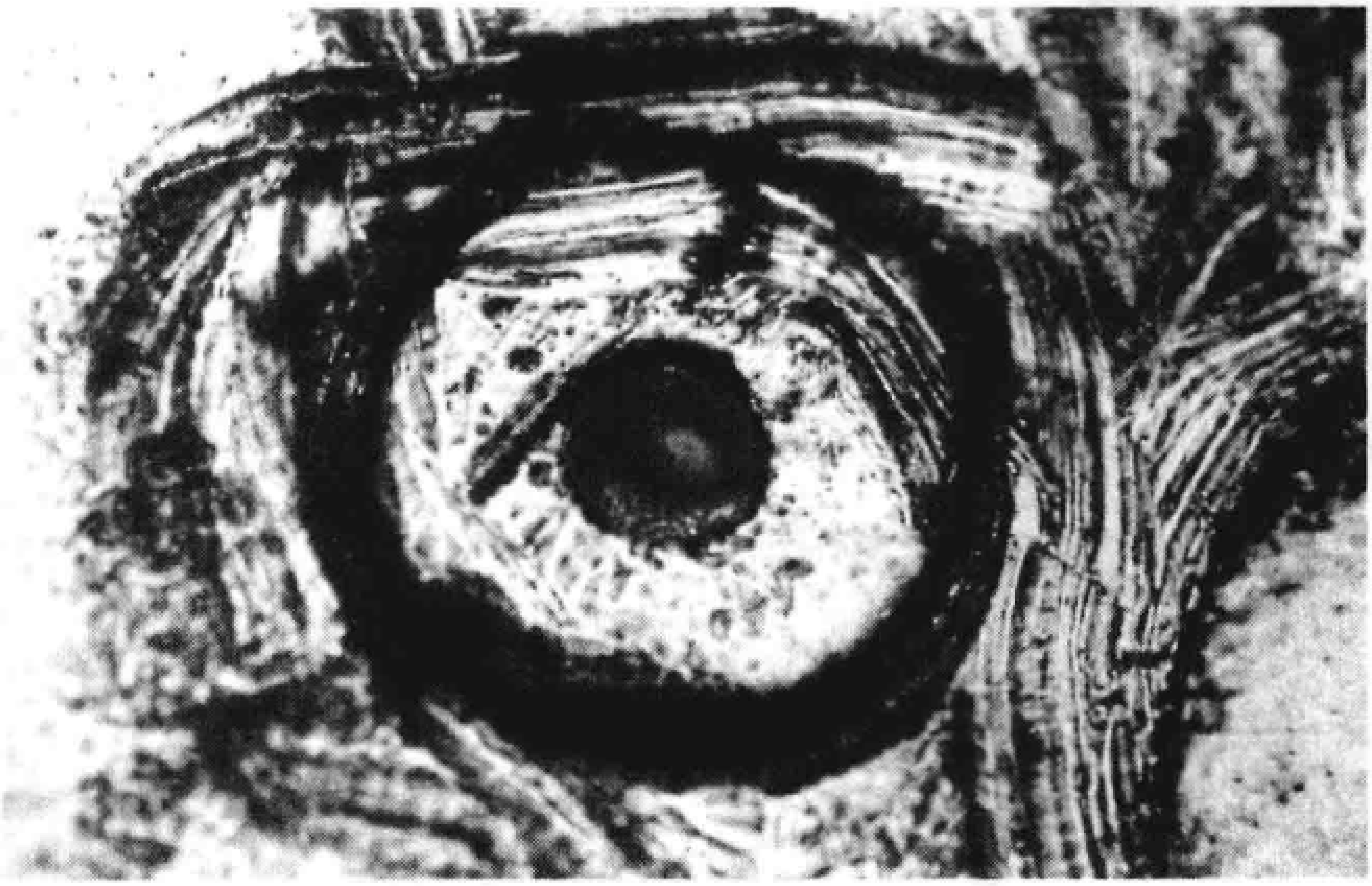

Figure C.19 A close-up (about 100×) of C.18, showing the pin broke off a piece of the glass fiber and moved it out of position.

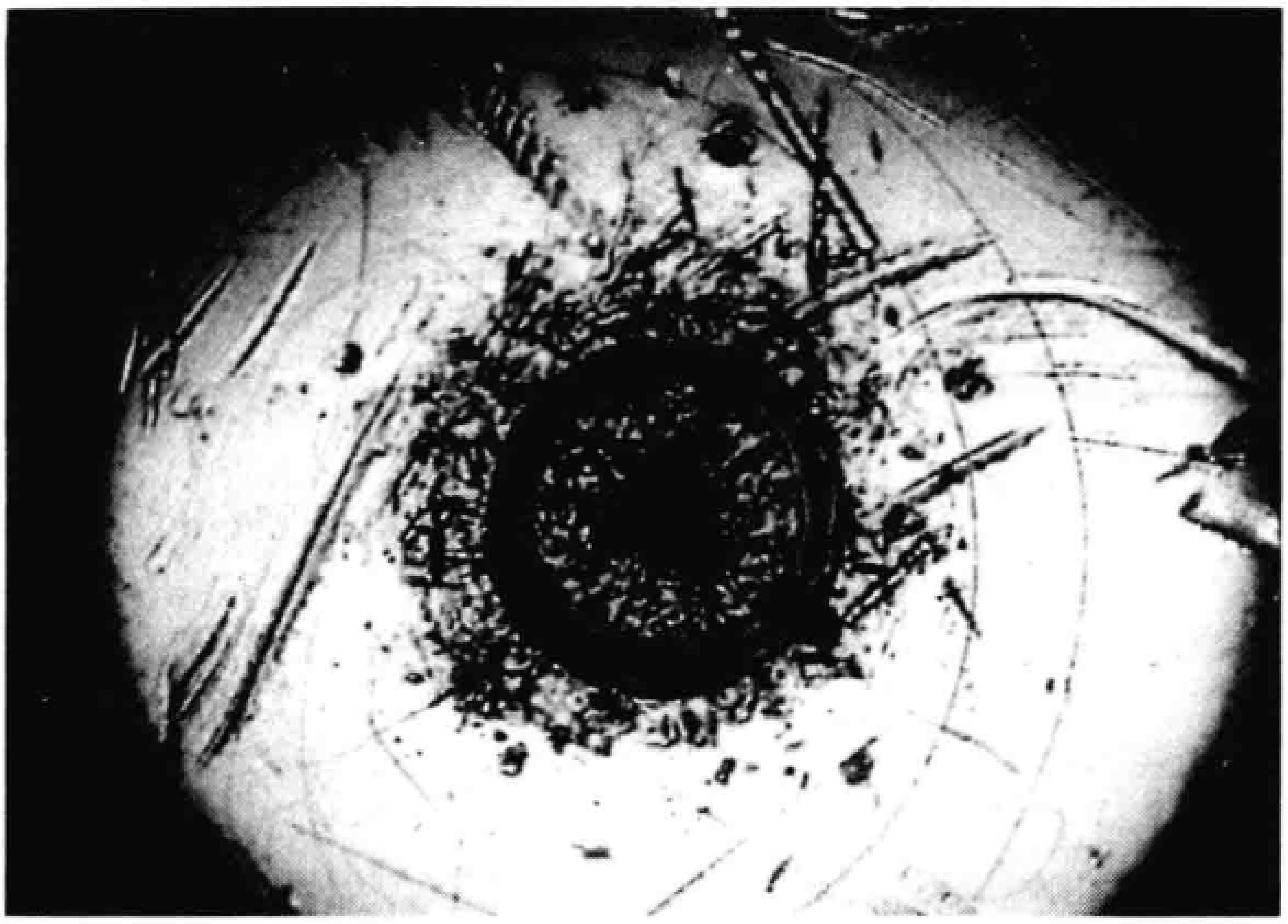

Figure C.20 At 50× the damage to another connector endface, from grit and repeated noncleaning, is seen.

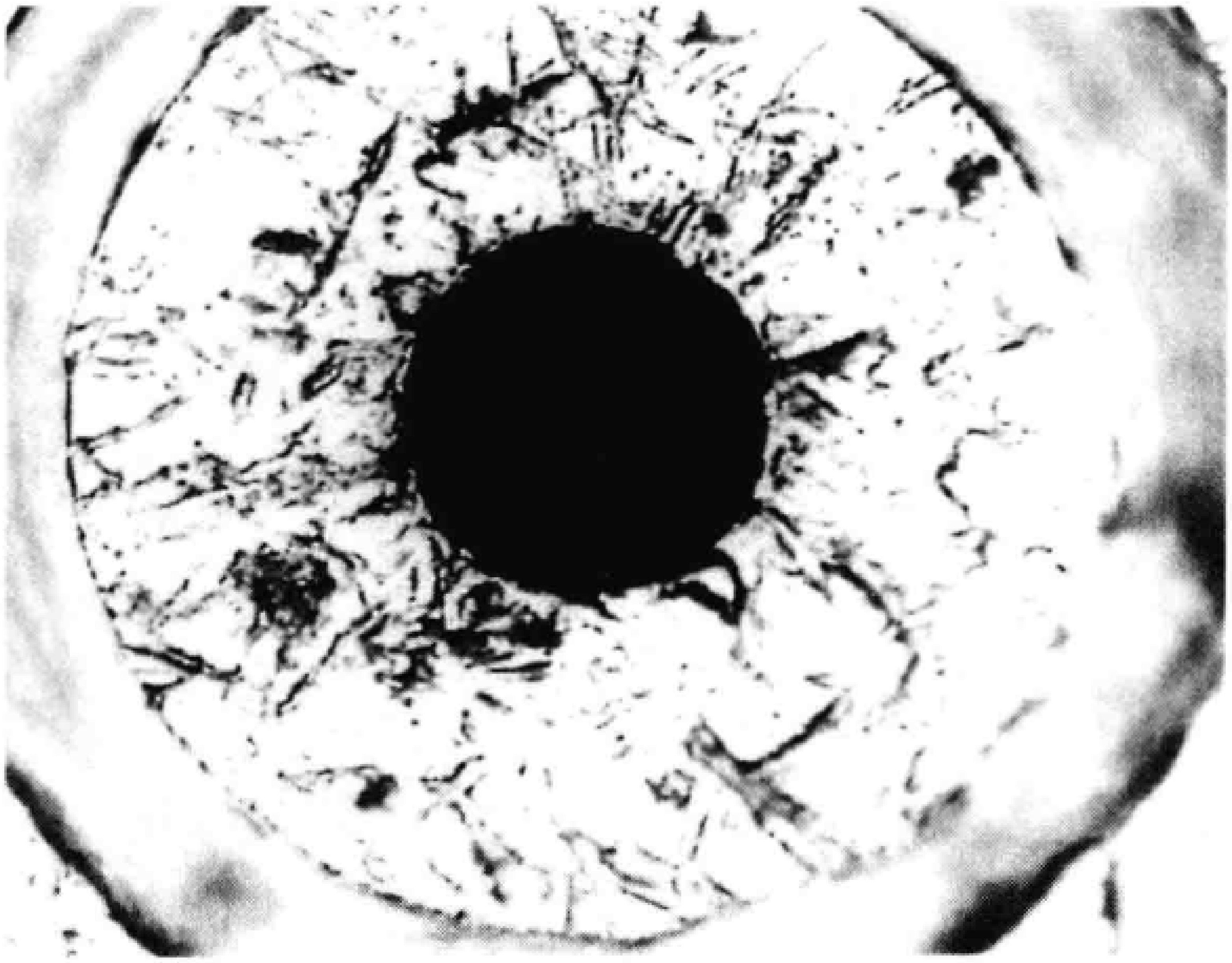

Figure C.21 At 200×, the damage and pitting to the connector in figure C.20 fiber is seen.

were designed for the FC, noncontacting connectors, using small glass spheres. When used in contacting connectors, these glass balls can scratch and pit the fiber. Index matching oil is also discouraged. It runs and migrates into unwanted areas, attracting and holding dust. If an index matching gel or oil must be used, apply it to a freshly cleaned connector, make the measurement, and immediately clean the gel or oil off. Never use a gel for long-term connections and never use it to improve a damaged connector. The gel can mask the damaged end and continued use of a damaged fiber can transfer damage to another connector.

Another tip for good fiber connector mating is: *not too tight.* Unlike electrical connections, tighter is not better. The connector's job is to bring the endfaces of two fibers together. Once they touch, tighter only causes a greater force to be applied to the delicate endface. In some connectors, the end can cock off-axis with a tight connection (due to the curved face) resulting in a worse return loss. Many measurements (such as the RIN measurement described earlier in Figure C.5) are actually improved by backing off the connector pressure. Also, if a piece of grit does happen to get by the cleaning procedure, a tighter connection is more likely to damage the glass. Tighten just until the two fibers touch.

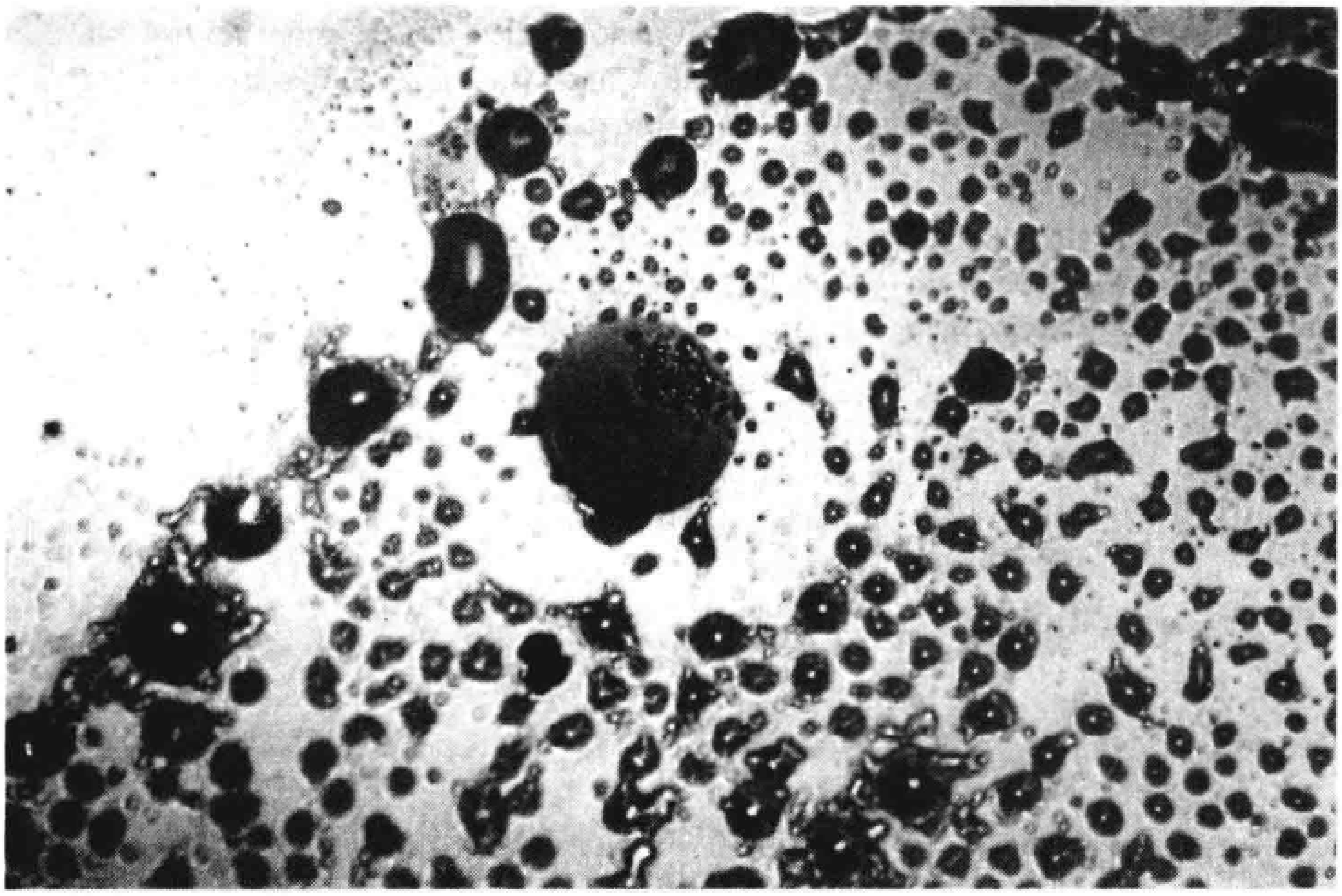

Figure C.22 A good connector was cleaned with a solvent and left to air dry. After evaporation the contaminants are left behind.

C.5 CLEANING PROCEDURES

The basics of cleaning are simple. Use a pure grade of isopropyl alcohol on a clean cotton swab to wipe off the endface and ferrule. (While other devices and methods also work, this one is easy, problem free, and inexpensive.) After the wet scrub, wipe off the wet endface with a dry swab, or blow it off with filtered, nonresidue compressed air. As Figure C.22 shows, leaving the fluid to air dry will leave behind the dissolved oils in little puddles which will interfere with the correct physical contact. Then, when reinserting the cable into the connector, insert it gently, in as straight a line as possible. Tipping, and inserting with an angle, can scrape off material from inside the connector or even break the inside sleeve of some connectors made with ceramic material.

It is not uncommon for a cable or connector to require more than one cleaning. If the performance seems poor, clean again. Often the second cleaning will restore the proper performance where the first did not. The idea is that the first step is to gently remove any grit and oil using the alcohol as a solvent. Remove the solvent by blowing it off or using a gentle dry wipe. Then if there is a caked-on layer of material still present (such as can happen if the beryllium-copper sides of the ferrule retainer gets scraped and deposited on the endface during insertion of the cable), the second cleaning should be harder, with a scrubbing action. But if scrubbed first, grit can be caught in the swab and become a gouging element.

A system is only as good as the weakest link. Don't let the connector become a failure because of poor attention. Use fusion splices on the more permanent critical nodes. Choose the best connector possible. Check (measure) the connector's return loss often, for degradation. Clean every connector, every time.

REFERENCE

1. Luis M. Fernadez and Donald R. Cropper. 1995. Evaluating Fiberoptic Connector Cleanliness for Accurate Measurements. *Fiberoptic Product News.* (6):45, 46.

Index